

**STUDIES OF THE EFFICIENCY OF SPIN EXCHANGE OPTICAL PUMPING**

by

Brian R. Lancor

A dissertation submitted in partial fulfillment of  
the requirements for the degree of

Doctor of Philosophy

(Physics)

at the

UNIVERSITY OF WISCONSIN–MADISON

2011

© Copyright by Brian R. Lancor 2011

All Rights Reserved

**DISCARD THIS PAGE**

# TABLE OF CONTENTS

	Page
<b>LIST OF TABLES</b> . . . . .	iv
<b>LIST OF FIGURES</b> . . . . .	v
<b>1 Introduction</b> . . . . .	<b>1</b>
1.1 History . . . . .	2
1.2 Description of Spin Exchange Optical Pumping . . . . .	3
1.2.1 Hybrid SEOP of K-Rb Mixtures . . . . .	6
1.3 Remaining Efficiency Questions . . . . .	6
1.3.1 Spin-exchange and Photon Efficiencies . . . . .	7
1.3.2 Limits to Alkali-Polarization . . . . .	8
1.4 Summary of Thesis . . . . .	9
<b>2 Spin Exchange Optical Pumping Apparatus</b> . . . . .	<b>14</b>
2.1 SEOP Apparatus . . . . .	14
2.1.1 Cells . . . . .	14
2.1.2 Pump Laser . . . . .	16
2.1.3 Oven . . . . .	16
2.1.4 Coils . . . . .	16
2.2 Diagnostics . . . . .	17
2.2.1 Probe Lasers . . . . .	17
2.2.2 Transverse EPR Spectroscopy . . . . .	19
2.2.3 Faraday Rotation Density Measurement . . . . .	28
2.2.4 [He] and [A] by Transmission . . . . .	29
2.3 Longitudinal vs. Transverse EPR . . . . .	32
2.4 $^3\text{He}$ Diagnostics . . . . .	36
<b>3 Dark State Absorption</b> . . . . .	<b>37</b>
3.1 Motivation . . . . .	37
3.2 Parameterization- $P_\infty$ . . . . .	38

	Page
3.3 Rb-He Molecular Potentials . . . . .	39
3.4 Estimates . . . . .	41
3.5 Preliminary Result . . . . .	43
3.6 Overview . . . . .	44
3.7 Experimental Procedure . . . . .	46
3.8 Analysis . . . . .	48
3.9 Results . . . . .	52
3.10 Cross-Sections . . . . .	55
3.11 Significance . . . . .	59
<b>4 Potassium Absorption at Rb D1 Resonance . . . . .</b>	<b>65</b>
4.1 Motivation . . . . .	65
4.2 Experimental Procedure . . . . .	67
4.3 K-He Cross Section . . . . .	70
4.4 Significance . . . . .	70
<b>5 Excited State Spin Relaxation . . . . .</b>	<b>73</b>
5.1 Motivation . . . . .	73
5.2 Excited State Nuclear Spin Relaxation . . . . .	74
5.3 Effect of Excited State Spin Relaxation on Optical Pumping . . . . .	75
5.4 Radiation Trapping . . . . .	77
5.5 Quantitative Optical Pumping Model . . . . .	80
5.5.1 Atom-light Interaction . . . . .	81
5.5.2 Excited State Evolution . . . . .	81
5.5.3 Excited-state Spin Relaxation . . . . .	82
5.5.4 Optical Pumping . . . . .	82
5.5.5 Ground-state Spin-Randomization . . . . .	84
5.5.6 Rb-Rb Spin-Exchange . . . . .	85
5.5.7 Radiation Trapping . . . . .	86
5.6 Discussion and Conclusions . . . . .	87
<b>6 Modeling . . . . .</b>	<b>89</b>
6.1 Overview . . . . .	89
6.2 Optical Pumping . . . . .	89
6.3 Dark State Absorption . . . . .	90
6.4 Ground State Spin Relaxation . . . . .	91
6.5 Wall Relaxation . . . . .	92

## Appendix

	Page
6.6 Excited State Relaxation . . . . .	93
6.7 Radiation Trapping . . . . .	93
6.8 Potassium-Helium Absorption . . . . .	94
6.9 Hybrid SEOP . . . . .	94
6.10 Efficiencies . . . . .	95
6.11 Optical Pumping Data . . . . .	98

**APPENDICES**

Appendix A: Helium Polarimetry . . . . .	106
Appendix B: Alkali-Metal Vapor Pressure Curves . . . . .	110
Appendix C: Spin Temperature . . . . .	112
Appendix D: Far Wing Cross Sections . . . . .	113
Appendix E: Equations for EPR Spectroscopy in Non-Spin Temperature Distributions	115

<b>LIST OF REFERENCES . . . . .</b>	<b>119</b>
-------------------------------------	------------

**DISCARD THIS PAGE**

## LIST OF TABLES

Table	Page
2.1 Characteristics of the vapor cells used in the experiments described in this thesis. The dimensions listed are $D$ =diameter for the spherical cells, and $D$ =diameter $\times$ $L$ =length for the cylindrical cell. . . . .	15
2.2 A table of the D1 and D2 broadening and lineshift coefficients for Rb in the presence of $^3\text{He}$ and $\text{N}_2$ buffer gases, as measured by [Romalis et al., 1997] . . . . .	30
2.3 Asymptotic forms of $I(\Delta'T_d)$ , along with a polynomial fit near $\Delta'T_d = 0$ [Walkup et al., 1984].	31
5.1 (top) Multipole relaxation cross sections $\sigma_i^{J'J}$ (in $\text{\AA}^2$ ), adapted from Ref. [Rotondaro and Perram, 1998]. The asterisk denotes an assumed quantity. The multipole relaxation rates for a gas of density $[G]$ are $\Gamma_c \alpha_i^{J'J} = \sigma_i^{J'J} v [G]$ , where $v = \sqrt{8kT/\pi\mu}$ is the mean thermal velocity for atom pairs of reduced mass $\mu$ at temperature $T$ . (bottom) Quenching rates $\Gamma_Q = \sigma_Q v [\text{N}_2]$ . . . . .	83
6.1 Comparison of measured ([Chen et al., 2007]) and modeled $P_A$ in $[\text{He}] \sim 1.5$ amg cells of increasing $D$ . Low $P_A$ at high $D$ is not explained by dark state and $\text{K-}^3\text{He}$ absorption. . . . .	104
B.1 The coefficients for determining the vapor pressures of the alkali-metals [Lide, 2011]. Number densities are given by $[A]=7.336 \times 10^{21} T^{-1} (10^{A+BT^{-1}})$ where $T$ is the temperature in Kelvin and $[A]$ will be in $\text{cm}^{-3}$ . . . . .	111
D.1 Functions for the $\text{Rb-}^3\text{He}$ pressure broadened absorption cross section. The near resonance function is the lineshape from [Romalis et al., 1997], with a linear approximation $I(x) = 0.3380 - 0.2245x$ for the shape function. The cross sections in the wings are fits to the NHRb transmission data, scaled by $[\text{}^3\text{He}]$ . . . . .	113
D.2 Functions for the $\text{Rb-N}_2$ pressure broadened absorption cross section. The near resonance function is the lineshape from [Romalis et al., 1997], with a linear approximation $I(x) = 0.3380 - 0.2245x$ for the shape function. The cross sections in the wings are fits to the K2 transmission data, scaled by $[\text{N}_2]$ . . . . .	114

**DISCARD THIS PAGE**

## LIST OF FIGURES

Figure	Page
1.1 Energy level diagram of the ground state and first excited state of Rb (ignoring the hyperfine splittings). Angular momentum conservation mandates that circularly polarized resonant photons with spin $+\hbar$ can excite atoms from the spin-down ground state but not from the spin-up ground state. Since Rb-buffer gas collisions in the excited state lead to random repopulation of the ground states, the depopulation pumping of the spin-down state leads to spin-polarization of the Rb spins. . . . .	4
1.2 Spin-exchange and photon efficiencies for $[\text{He}]=8$ amg cells with $D=0$ to $D=500$ . In all cases photon efficiencies are 5 to 10 times lower than the fundamental spin-exchange efficiencies. This implies that sources of alkali-metal spin relaxation are poorly understood. . . . .	8
1.3 Alkali-metal polarization extrapolated to infinite pumping power, $P_{max}$ , in cells with $D$ ranging from 0 to 500. The decrease in $P_{max}$ with increasing $D$ suggests K absorption of pump light at the Rb resonance frequency may be a significant spin-relaxation process. The low $P_{max}$ in the pure Rb cell indicates there must also be another pump induced relaxation process. . . . .	9
1.4 Modified energy level diagram of the ground state and first excited state of Rb (ignoring the hyperfine splittings). Rb-buffer gas collisions weakly mix the $^2P_{1/2}$ and $^2P_{3/2}$ states, giving the first excited state a small $m_J=3/2$ component. This allows absorption of $\delta=1$ light by the $m_J=1/2$ ground state sublevel. . . . .	10
1.5 Comparison of measured[Babcock et al., 2003] and modeled maximum achievable alkali polarization as a function of K/Rb density ratio $\mathcal{D}$ , with measured potassium absorption (solid blue) and without (dashed black), in an $[\text{He}]=8.0$ amg hybrid pumping cell, with a broadband, $\Gamma = 1000\text{GHz}$ , pumping source. . . . .	12

Figure	Page
1.6 Measured spin exchange (yellow circles) and photon efficiencies (blue squares) for [He]=8 amg cells with $D=0$ to $D=500$ [Babcock et al., 2003], along with a naive model for the photon efficiency (red-orange line) and a model that includes dark state absorption, excited state nuclear spin relaxation and potassium absorption at the Rb resonance (black crosses). . . . .	13
2.1 Picture of the SEOP apparatus. . . . .	15
2.2 Picture of the pump laser, and its external cavity. A telescope is placed inside the cavity, imaging the diode array bar on the diffraction grating. This insures that the diffracted beam is imaged back onto the bar, feeding each emitter back to itself. . . . .	17
2.3 Picture of the calcium silicate oven. The hot air flows in through the arm on the right. The temperature sensor is unseen, just above the cell. . . . .	18
2.4 Transverse EPR spectrum taken at $\sim T=150$ °C in Betty, with $P_{\text{Rb}} \approx 0.82$ . Each peak in the spectrum is due to the RF field driving one ground-state sub-level transition. . . . .	20
2.5 Measurement of polarization via transverse EPR spectroscopy. As the DC magnetic field is swept to match the Rb Zeeman EPR frequencies, the index of refraction of the Rb atoms becomes modulated at the 26.4-MHz RF driving frequency, thus modulating the polarization of the probe laser. This modulation is detected and demodulated by the lock-in amplifier. The Rb polarization is deduced from the ratio of areas of the EPR resonances. . . . .	24
2.6 EPR spectrum for high $P_{\text{Rb}} \approx 0.98$ . Very high signal to noise is needed to resolve the third peak set. The spike at the left end of the data is due a rapid ramping of the magnetic field at the beginning of the sweep. . . . .	27
2.7 From [Walkup et al., 1984], numerically calculated points (+), the dotted line is a linear Taylor-series approximation for small $ T_d $ , and the dashed lines are asymptotic approximations for $ T_d  \gg 1$ . . . . .	31
2.8 Measurement of the product $P_{\text{Rb}}P_{\infty} \cos \theta$ on resonance (where $P_{\infty}$ must be very nearly one), along with modeling of the data using $P_{\text{Rb}}$ measured with longitudinal EPR spectroscopy (solid red line). The data fit well when a significantly lower $P_{\text{Rb}}$ is put into the model(dashed green line). . . . .	34
2.9 $P_{\text{Rb}}$ deduced from transverse and longitudinal EPR spectroscopy . . . . .	35

## Appendix

Figure	Page
2.10 $P_{\text{Rb}}$ deduced from transverse EPR spectroscopy, and Faraday rotation calibrated to EPR spectroscopy at high $P_{\text{Rb}}$ . . . . .	36
3.1 Adiabatic energy curves for RbHe molecules adapted from [Pascale, 1983] with the method of [Allard and Kielkopf, 1982]. The projection of the total electronic angular momentum along the interatomic axes is given in brackets. The curve crossings between the photon-dressed $5s$ state and the two excited-state curves mean that photon absorption is allowed during a collision. As explained in the text, these absorption processes are not subject to the free-atom dipole selection rules, allowing normally angular-momentum-forbidden transitions to occur . . . . .	40
3.2 Fine-structure mixing angle for the $5p[1/2]$ states as a function of interatomic separation.	44
3.3 $P_{\infty}$ measured by tuning the pump laser to a range of frequencies and measuring the resulting polarization $P_{\text{Rb}}(\nu)$ , pumping rate $R_p(\nu)$ , and ground state spin-relaxation rate $\Gamma_{\text{Rb}}$ . The dashed line is a naive model assuming Lorentzian lineshapes for the D1 and D2 resonances. . . . .	45
3.4 Apparatus for measuring the circular dichroism of Rb-He vapor. The pump laser, propagating parallel to a magnetic field, spin-polarizes Rb atoms by optical pumping. The polarization is set either parallel or antiparallel to the field, as determined by the orientation of a quarter-wave plate. The fractional transmission of a weak, circularly polarized, tunable probe laser is determined by the ratio of photodiode voltages before to those after traversal of the cell. The circular dichroism is then determined from the transmissions for both directions of Rb polarization. . . . .	47
3.5 Normalized circular dichroism $C$ , near resonance, taken at a low density and low polarization, $P_{\text{Rb}} = 0.929$ . Modeling with $P_{\infty} = 1$ that omits the hyperfine splitting [solid (blue) line] predicts a nearly flat $C$ at $P_{\text{Rb}} \cos \theta_p$ . Modeling with $P_{\infty} = 1$ , but including the ground-state hyperfine structure [dashed (green) line], is in good agreement with the data. . . . .	50
3.6 $P_{\infty}$ results near the D1 resonance line. The agreement between cells of different He pressure verifies that the effects originate from absorption in RbHe collisions. The dashed line denotes the frequency dependence of the dichroism, making the naive assumption of purely Lorentzian line broadening, and the solid line is the result of using the molecular absorption cross section from Eq. ?? . . . . .	53

## Appendix

Figure	Page
3.7 Measured $P_\infty$ of RbHe molecules in the region between the first resonance lines of Rb. The solid curve shows the expected dichroism from the very naive assumption of purely Lorentzian broadened lines. . . . .	54
3.8 Measured $P_\infty$ of RbN <sub>2</sub> molecules in the region between the first resonance lines of Rb. The solid curve shows the expected dichroism from the very naive assumption of purely Lorentzian broadened lines. . . . .	55
3.9 Cross section for absorption of unpolarized light by Rb atoms in the presence of 2.80 amg of N <sub>2</sub> buffer gas. For detunings larger than $\sim 200$ GHz, the lineshape deviates significantly from the lineshape in [Romalis et al., 1997](Solid black line). . . . .	56
3.10 Cross sections, normalized to a 1-amg N <sub>2</sub> density, for absorption of $\delta = 1$ , $\delta = -1$ , and $\delta = 0$ light by fully polarized Rb atoms. The solid line is the linear fit to the $\delta = 1$ data . . . . .	57
3.11 Cross section for absorption of unpolarized light by Rb atoms in the presence of 3.27 amg of <sup>3</sup> He buffer gas. For detunings larger than $\sim 700$ GHz, the lineshape deviates significantly from the lineshape in [Romalis et al., 1997](Solid black line). The rise in cross section on the right side of the data is the D2 resonance. . . . .	58
3.12 Cross section for dark state absorption due to RbHe molecules, normalized to 1 amg <sup>3</sup> He density. The solid line is a linear fit in the region of the D1 resonance. . . . .	59
3.13 Light propagation results without[solid (red) line], and with [dashed (green) line] dark state absorption, for pumping with a laser whose spectral profile is shown in Fig. ???. Top: power as a function of position. The reduced dichroism produces a faster attenuation of the light. Bottom: Corresponding Rb polarizations, which are limited to values less than 100% even at the cell entrance, but then decay further as the spectral profile of the light is increasingly off-resonant (see Fig. 3.14) . . . . .	62
3.14 Measured spectra before and modeled spectra after propagation through the cell shown in Fig. 3.13, modeled as described in the text. Light in the wings of the spectrum contributes disproportionately to the dark state absorption, while contributing comparatively less to the resonant, dipole allowed D1 absorption. The net effect is significantly greater absorption than expected. . . . .	63
4.1 Alkali-metal polarization with infinite pumping power, $P_{max}$ , measured as a function of K to Rb density ratio $\mathcal{D}$ measured in [Babcock et al., 2003]. . . . .	66
4.2 Optical thickness at 794.41 nm, as a function of [K] in [He]=2.93 amg cell. The slope of the linear fit gives $l\sigma$ . The y-intercept of the fit is fixed at zero. . . . .	68

Appendix	Page
Figure	
4.3 $\sigma$ as a function of wavelength in cells of a) [He]=2.93 amg and b) [He]=.0924 amg. Due to 1/10000 Rb contamination of this nominally pure K cell, we avoid measurements directly on the Rb resonance. . . . .	69
4.4 Comparison of measured [Babcock et al., 2003] and modeled maximum achievable alkali polarization as a function of K/Rb density ratio $D$ in a [ $^3\text{He}$ ]=8.0 amg hybrid cell pumped by a 1000 GHz bandwidth source. Modeling was done with (solid blue) and without (dashed black) off-resonant potassium absorption. . . . .	72
5.1 Total angular momentum evolution in the excited state, for initially fully polarized $P_{1/2}^{85\text{Rb}}$ (upper curves) and $^{87\text{Rb}}$ (lower curves) in 1 amg of He gas and 0.065 amg of $\text{N}_2$ , assuming no quenching. Collisions rapidly relax the electronic angular momentum to nearly zero, but hyperfine coupling partially repolarizes the electron so that repeated collisions eventually relax the nucleus as well. The substantially smaller hyperfine splitting in $^{85\text{Rb}}$ makes the effect much smaller in that isotope. The dashed curves include fine-structure changing collisions. . . . .	75
5.2 a) Calculated fraction of nuclear spin lost in the excited state during the optical pumping cycle, $f_I$ , at various nitrogen and He densities. b) Paramagnetic coefficient $\epsilon$ for natural abundance Rb vapor in spin-temperature equilibrium, as a function of electron spin-polarization. . . . .	76
5.3 The steady-state polarization as a function of the product $f_I\epsilon$ , which is approximately twice the angular momentum lost by the nucleus during the excited-state evolution. The three curves are, top to bottom, for $R = \infty$ , $R = 100\Gamma_{\text{sd}}$ , and $R = 14\Gamma_{\text{sd}}$ . . . . .	78
5.4 The photon demand as a function of the product $f_I\epsilon$ , normalized to the ground-state spin-relaxation rate $\Gamma_{\text{sd}}$ , the value that would be obtained in the absence of excited-state nuclear spin-precession. The three curves, top to bottom, are for $R = \infty$ , $R = 100\Gamma_{\text{sd}}$ , and $R = 14\Gamma_{\text{sd}}$ . FIX AXIS LABEL . . . . .	79
5.5 The photon demand normalized to its ideal value. The upper two curves are for 1 amg He density, the lower two for 8 amg. The upper curve of each pair includes both radiation trapping and excited-state relaxation effects, while the lower includes only excited-state relaxation. . . . .	87

## Appendix

## Figure

Page

- 6.1 Measured spin exchange (yellow circles) and photon efficiencies (blue squares) for  $[\text{He}]=8$  amg cells with  $D=0$  to  $D=500$  [Babcock et al., 2003], along with a naive model for the photon efficiency (red-orange line) and a model that includes dark state absorption, excited state nuclear spin relaxation and potassium absorption at the Rb resonance (black crosses). . . . . 96
- 6.2 Spin exchange and photon efficiencies for  $[\text{He}]=8$  amg cells with  $D=0$  to  $D=500$ . In all cases photon efficiencies are 5 to 10 times lower than the fundamental spin exchange efficiencies. This implies that sources of alkali-metal spin relaxation are not fully understood. . . . . 97
- 6.3  $P_{max}$  as a function of  $D$  for  $[\text{He}]=7.9$  amg with broadband ( $\sim 800$  GHz) and narrowband (100 GHz) pumping sources, and for  $[\text{He}]=6.0, 4.0, 2.0$  and  $1.0$  with narrowband pumping. . . . . 99
- 6.4  $P_{\text{Rb}}$  as a function of the spin exchange rate in a pure Rb,  $[\text{He}]=1.24$  amg cell pumped with 52W of narrowband ( $\sim 125$  GHz) light. Measured values from [Chen et al., 2007] (blue squares), naive models with (red diamonds) and without (red circles) laser heating, and full models including the relaxation mechanisms described in this thesis with (green diamonds) and without (green circles) laser heating are shown. Including all relaxation mechanisms and estimate laser heating effects produces results in reasonable agreement with the data. . . . . 100
- 6.5  $P_{\text{Rb}}$  as a function of the spin exchange rate in a  $D=4.8$ ,  $[\text{He}]=3.45$  amg cell pumped with 52W of narrowband ( $\sim 125$  GHz) light. Measured values from [Chen et al., 2007] (blue squares), naive models without (red circles) laser heating, and full models including the relaxation mechanisms described in this thesis with (black crosses) and without (green circles) laser heating are shown. Models that include all known relaxation underestimate  $P_{\text{Rb}}$  at high spin exchange rate, and the inclusion of laser heating greatly increases the discrepancy. . . . . 103
- 6.6 Measured values of  $P_{\text{Rb}}$  as a function of Rb density in a pure Rb,  $[\text{He}]=0.85$  amg cell pumped with 14W of narrowband light (closed circles) and 42W of broadband light (open circles) from [Chann et al., 2003]. Naive (closed green diamonds) and full (open green diamonds) modeling (including laser heating) of the broadband pumping, and full modeling of the narrowband pumping (blue squares) are also shown. . . . . 105
- A.1 Plot (calculated in [Babcock et al., 2005a]) of the magnetic correction factor for the various alkali isotopes as a function of the EPR frequency. Note that for the special case of  $^{85}\text{Rb}$  and  $^{23}\text{Na}$  the correction factors follow each other to less than 0.1% . . . 108

Appendix Figure	Page
A.2 Plot (Diagram of the NMR FID setup. . . . .	109
B.1 Vapor pressure curves for Cs,Rb,K,Na, and Li. . . . .	110
E.1 Labels of the peak areas in $^{85}\text{Rb}$ EPR spectroscopy. . . . .	115
E.2 Labels of the peak areas in $^{87}\text{Rb}$ EPR spectroscopy. . . . .	117

# Chapter 1

## Introduction

Optical pumping of alkali-metal atoms at high temperatures and high buffer gas pressures is a powerful technique for precision spectroscopies (clocks, magnetometers) [Jau et al., 2004, Kominis et al., 2003], and for collisional transfer of angular momentum to noble gas nuclei via spin-exchange collisions [Walker and Happer, 1997]. Hyperpolarized  $^3\text{He}$  and  $^{129}\text{Xe}$  produced by spin exchange optical pumping (SEOP) have many applications, including use in neutron spin filters, magnetic resonance imaging, polarized targets for electron beams, and tests of fundamental symmetries [Vasilakis et al., 2009, Fu et al., 2011].

In spin exchange optical pumping of  $^3\text{He}$ , a high power, circularly polarized pump laser is resonantly absorbed by an alkali-metal vapor, transferring angular momentum to the alkali-metal electron spin. Then, the alkali-metal atoms transfer that angular momentum to the nuclear spin of the  $^3\text{He}$  vapor through a weak hyperfine coupling during collisions. The optical pumping portion of SEOP should be very efficient, in terms of the number of photons needed to polarize a given number of alkali-metal atoms, since the selection rules of the ground state to first excited state (or D1) transition don't allow fully spin polarized alkali-metal atoms to absorb the pumping light. Thus, the pumping light can propagate deeply into cells with very high alkali-metal density, polarizing a very large number of atoms. However, previous experiments have shown optical pumping efficiencies to be 5 to 10 times lower than theoretical predictions [Babcock et al., 2003, Chen et al., 2007]. Developing an understanding of the sources of this inefficiency is critical for the further improvement of SEOP polarizers.

## 1.1 History

Until ten years ago, the  $^3\text{He}$  polarization achieved through SEOP was limited to  $\sim 55\%$ . Polarizations were partially limited by the difficulty in maintaining Rb- $^3\text{He}$  spin-exchange rates that were very high compared to  $^3\text{He}$  wall relaxation rates in SEOP cells. Much work was done at NIST and elsewhere to consistently produce cells with long  $^3\text{He}$  lifetimes at room temperature. At Wisconsin, our lab developed techniques for frequency narrowing the diode array bars typically used in SEOP to significantly improve the optical pumping of the alkali-metal vapors, allowing the polarization of a higher density of alkali atoms for a given laser power, increasing the spin exchange rate [Babcock et al., 2005a].

A fundamental limit on the efficiency of Rb- $^3\text{He}$  SEOP is the ratio of the spin exchange to spin destruction cross-sections in Rb- $^3\text{He}$  collisions [Babcock et al., 2003, Walker and Happer, 1997]. Potassium- $^3\text{He}$  collisions were found to be more efficient ([Ben-Amar Baranga et al., 1998]), so to exploit the higher efficiency, a hybrid SEOP technique was developed, where Rb is optically pumped in the presence of 1-100 times as much K [Babcock et al., 2003]. With these techniques,  $^3\text{He}$  polarizations near 80% are achieved, an impressive advancement but still shy of predictions approaching 100%.

This lab identified a temperature dependent  $^3\text{He}$  relaxation, (dubbed the X-factor) that scales with alkali-metal density, as the remaining limit on achieved  $P_{\text{He}}$  [Babcock et al., 2006]. This limit cannot be overcome by increasing the spin exchange rate, as doing so increases the  $^3\text{He}$  relaxation rate proportionally.

However, it would still be very useful to increase the optical pumping efficiency of SEOP and HySEOP. The optical pumping efficiency limits the number of alkali-metal atoms that can be spin-polarized for a given laser power, and therefore the rate at which a given amount of  $^3\text{He}$  can be polarized. In [Babcock et al., 2003] they measured the optical pumping efficiency of Rb SEOP and K-Rb HySEOP cells with high helium density, and found the efficiencies to be 5 to 10 times

lower than expected in all cells. In this thesis I will describe experimental and theoretical investigations of several mechanisms limiting the efficiency of optical pumping in SEOP and HySEOP, and investigate, through computational models, their effect on optical pumping of SEOP cells.

## 1.2 Description of Spin Exchange Optical Pumping

Spin exchange optical pumping is a technique for producing spin polarized noble gas nuclei, using alkali-metal vapor as an intermediary to transfer angular momentum from a circularly polarized pump laser to the noble gas nuclei. Typically, a sealed glass cell containing 1 to 8 Atm of  $^3\text{He}$ , 0.065 Atm of  $\text{N}_2$ , and a small amount of Rb liquid is heated to  $\sim 180^\circ \text{C}$ . This leads to an equilibrium vapor density of  $\sim 5 \times 10^{14}$  Rb atoms per  $\text{cm}^3$ . The pump laser, typically a diode array bar, is circularly polarized and tuned on resonance with the  $^2S_{1/2} \rightarrow ^2P_{1/2}$  (or D1) ground state to first excited state transition of the Rb atoms. Absorption of the probe beam deposits angular momentum in the Rb vapor, polarizing the Rb electron spin. A weak hyperfine coupling during Rb- $^3\text{He}$  collisions then transfers angular momentum to the  $^3\text{He}$  nuclei. Angular momentum leaks out the Rb electron spins in Rb- $^3\text{He}$ , Rb-Rb, Rb- $\text{N}_2$ , and Rb-wall collisions.

To understand the optical pumping step, it is helpful to consider the energy level diagram in Fig. 1.1. Both the  $^2S_{1/2}$  and  $^2P_{1/2}$  states have total angular momentum  $J=L+S=1/2$ , and therefore have two magnetic sublevels,  $m_J=\pm 1/2$ . Photons from the circularly polarized pump beam carry angular momentum in the pump propagation direction,  $\lambda=1$ . In order to conserve angular momentum, a pump photon can only be absorbed if the atom gains 1 unit of angular momentum. Thus photons in the  $m_J=-1/2$  ground state can absorb pump photons, moving to the  $m_J=1/2$  excited state, but atoms in the  $m_J=1/2$  ground state cannot absorb pump photons, as the  $^2P_{1/2}$  state does not have an  $m_J=3/2$  sublevel. The  $m_J=1/2$  ground state is a so-called dark state, because it does not interact with the pump light. The basic premise of the optical pumping is then very simple; Atoms are excited out of only one ground state, then decay with roughly 50% probability into the other, dark ground state. After a short time most of the atoms are moved into the dark state, where they relax only slowly into the other ground state through spin-destruction collisions.

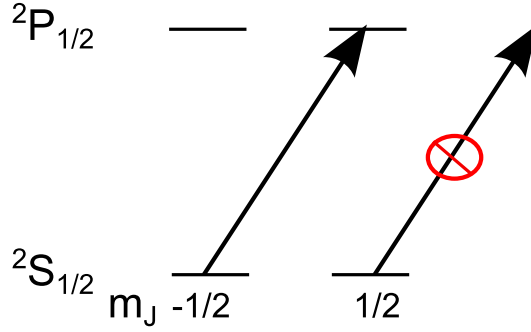


Figure 1.1 Energy level diagram of the ground state and first excited state of Rb (ignoring the hyperfine splittings). Angular momentum conservation mandates that circularly polarized resonant photons with spin  $+\hbar$  can excite atoms from the spin-down ground state but not from the spin-up ground state. Since Rb-buffer gas collisions in the excited state lead to random repopulation of the ground states, the depopulation pumping of the spin-down state leads to spin-polarization of the Rb spins.

For this simple picture to be accurate, it is important to prevent excited Rb atoms from decaying through spontaneous emission. Spontaneously emitted photons have random propagation directions and polarizations and can excite atoms in the dark ground state, providing an additional relaxation mechanism.  $\text{N}_2$  buffer gas has a large cross-section ( $\sim 50\text{\AA}^2$ [Rotondaro and Perram, 1998]) for collisional de-excitation of Rb, so 10s of Torr of  $\text{N}_2$  are added to quench the excited state atoms in a time short compared to the natural lifetime (27ns).

We can now quantitatively describe the optical pumping process. The excitation rate per Rb atom can be written

$$\langle \delta\Gamma \rangle = R_p(1 - P_{\text{Rb}}) \quad (1.1)$$

where the polarization  $P_{\text{Rb}} = 2\langle S_z \rangle$ , and the pumping rate  $R_p$  is the excitation rate per unpolarized Rb atom, given by

$$R_p = \int_0^\infty \phi(\nu) \sigma_0(\nu) d\nu \quad (1.2)$$

where  $\phi(\nu)$  is the pump beam photon flux per unit frequency, and  $\sigma_0(\nu)$  is the absorption cross section of unpolarized atoms. Collisions between excited Rb atoms and the  $^3\text{He}$  and  $\text{N}_2$  buffer gases randomize the Rb electron in the excited state, leading to decay with equal probability into either ground state sublevel. Thus, each excitation has a 1/2 probability of changing the angular momentum of the Rb atom by one unit, giving an equation for the evolution of the Rb angular

momentum [Walker and Happer, 1997]

$$\frac{dF_z}{dt} = \frac{1}{2}R_p(1 - P_{\text{Rb}}) - \Gamma_{\text{Rb}}\frac{P_{\text{Rb}}}{2} \quad (1.3)$$

where the Rb ground state relaxation processes have been summed in the rate  $\Gamma_{\text{Rb}}$ . Solving this in steady state gives

$$P_{\text{Rb}} = \frac{R_p}{R_p + \Gamma_{\text{Rb}}} \quad (1.4)$$

In practice,  $R_p$  can be made much greater than  $\Gamma_{\text{Rb}}$ , so  $P_{\text{Rb}}$  should be nearly one under operating conditions.

Note that the Rb atoms also have nuclear spin,  $I=5/2$  for  $^{85}\text{Rb}$  and  $I=3/2$  for  $^{87}\text{Rb}$ . We ignore the effect of the nuclear spin because the ground state splitting induced by the  $I \cdot J$  hyperfine interaction is 6.8 GHz in  $^{87}\text{Rb}$  and 3.5 GHz in  $^{85}\text{Rb}$ , while the pressure broadened absorption linewidths are  $\sim 18$  GHz/Atm for  $^3\text{He}$  and  $\text{N}_2$  buffer gasses, and pump laser linewidths are typically 80 GHz or more. Thus, the splitting is not resolved in the optical pumping process.

The second step in SEOP is the transfer of angular momentum from the Rb electron spin to the  $^3\text{He}$  nuclear spin through spin-exchange collisions. Angular momentum is transferred at a rate  $k_{SE}[\text{Rb}]$ , where  $k_{SE}$  is the Rb- $^3\text{He}$  spin-exchange rate coefficient and  $[\text{Rb}]$  is the rubidium number density [Ben-Amar Baranga et al., 1998, Chann et al., 2002a]. The  $^3\text{He}$  spins lose angular momentum through  $^3\text{He}$ - $^3\text{He}$  magnetic dipole interactions, collisions with the cell walls, and diffusion through magnetic field gradients at a combined rate  $\Gamma_{\text{He}}$  [Walker and Happer, 1997]. In addition, Babcock *et al.* have identified a temperature dependent  $^3\text{He}$  spin relaxation mechanism that scales with  $[\text{Rb}]$ , and is parameterized as  $\Gamma_X = X k_{SE}[\text{Rb}]$  [Babcock et al., 2006]. This effect varies from cell to cell, (ranging from  $\sim .15$  to 1.2) but  $X$  was shown to correlate with the surface to volume ratio of cells, indicating that it is an effect that occurs at the walls. Putting these effects together gives

$$\frac{dP_{\text{He}}}{dt} = k_{SE}[\text{Rb}] (P_{\text{Rb}} - P_{\text{He}}) - (\Gamma_{\text{He}} + X k_{SE}[\text{Rb}]) P_{\text{He}} \quad (1.5)$$

The steady state solution is

$$P_{\text{He}} = P_{\text{Rb}} \frac{k_{SE}[\text{Rb}]}{k_{SE}[\text{Rb}](1 + X) + \Gamma_{\text{He}}} \quad (1.6)$$

The X-factor limits the achievable  $P_{\text{He}}$ , even at very high spin-exchange rates to

$$P_{\text{He}} = P_{\text{Rb}} \frac{1}{1 + X} \quad (1.7)$$

### 1.2.1 Hybrid SEOP of K-Rb Mixtures

A modified form of SEOP, where the Rb vapor is replaced with a mixture of K and Rb was developed by [Babcock et al., 2003]. In this method, the Rb vapor is directly optically pumped as described in the previous section, and very rapid K-Rb spin-exchange collisions bring the K electron spin into equilibrium with the Rb spins. Both alkali-metals undergo spin-exchange collisions with the  $^3\text{He}$  gas. Typically, the K-Rb spin-exchange rate is high enough that we can assume  $P_{\text{Rb}} = P_{\text{K}} = P_A$ , and we can write the differential equation for the evolution of the total angular momentum

$$[\text{Rb}] \frac{dF_z^{\text{Rb}}}{dt} + [\text{K}] \frac{dF_z^{\text{K}}}{dt} = [\text{Rb}] R_p \frac{1}{2} (1 - P_A) - ([\text{Rb}] \Gamma_{\text{Rb}} + [\text{K}] \Gamma_{\text{K}}) P_A \quad (1.8)$$

using the density ratio,  $D = \frac{[\text{K}]}{[\text{Rb}]}$ , we get

$$\frac{1}{D} \frac{dF_z^{\text{Rb}}}{dt} + \frac{dF_z^{\text{K}}}{dt} = \frac{R_p}{D} \frac{1}{2} (1 - P_A) - \left( \frac{\Gamma_{\text{Rb}}}{D} + \Gamma_{\text{K}} \right) P_A \quad (1.9)$$

and, the steady state solution is

$$P_A = \frac{R_p/D}{R_p/D + \Gamma_{\text{Rb}}/D + \Gamma_{\text{K}}} \quad (1.10)$$

The critical point is that  $\Gamma_{\text{K}} \sim \Gamma_{\text{Rb}}/10$ , whereas  $k_{SE}^{\text{Rb-He}} \approx k_{SE}^{\text{K-He}}$ . Thus, a larger fraction of the angular momentum transferred from the laser to the alkali-metal spin goes to polarizing the  $^3\text{He}$  through spin-exchange.

### 1.3 Remaining Efficiency Questions

Although the limits on achievable  $^3\text{He}$  polarization are well characterized by the X-factor, there is evidence that the optical pumping step of SEOP is much less efficient than the simple model described above would predict. Babcock *et al.* performed a series of experiments on the SEOP performance of pure Rb and hybrid cells with density ratios up to 500, and  $[\text{He}] = 8$  amagats (an amagat

is a unit of density, where 1 amg is the density of an ideal gas at STP)[Babcock et al., 2003]. They defined and measured two efficiencies, the spin-exchange efficiency and the photon efficiency.

### 1.3.1 Spin-exchange and Photon Efficiencies

The spin-exchange efficiency is defined as the ratio of the rate of angular momentum transfer from polarized Rb atoms to unpolarized  $^3\text{He}$  atoms to the rate of alkali-metal angular momentum loss to ground state collisions. Taking Eq. 1.5 and setting  $P_{\text{He}}$  to zero gives

$$\left(\frac{dP_{\text{He}}}{dt}\right)_{P_{\text{Rb}}=0} = k_{SE}^{\text{Rb-He}}[\text{Rb}]P_{\text{Rb}} \quad (1.11)$$

and considering the hybrid case gives

$$\left(\frac{dP_{\text{He}}}{dt}\right)_{P_A=0} = (k_{SE}^{\text{Rb-He}}[\text{Rb}] + k_{SE}^{\text{Rb-K}}[\text{K}])P_A \quad (1.12)$$

The total rate of angular momentum loss due to ground-state relaxation collisions is written

$$[\text{Rb}]\left(\frac{dF_z^{\text{Rb}}}{dt}\right)_{gsr} + [\text{K}]\left(\frac{dF_z^{\text{K}}}{dt}\right)_{gsr} = -([\text{Rb}]\Gamma_{\text{Rb}} + [\text{K}]\Gamma_{\text{K}} + [\text{Rb}][\text{K}]q_{\text{KRb}})P_A \quad (1.13)$$

Thus, the spin exchange efficiency becomes

$$\eta_{SE} = \frac{(dP_{\text{He}}/dt)_{P_A=0}}{[\text{Rb}]\left(\frac{dF_z^{\text{Rb}}}{dt}\right)_{gsr} + [\text{K}]\left(\frac{dF_z^{\text{K}}}{dt}\right)_{gsr}} = \frac{[{}^3\text{He}](k_{SE}^{\text{Rb-He}}[\text{Rb}] + k_{SE}^{\text{K-He}}[\text{K}])}{[\text{Rb}]\Gamma_{\text{Rb}} + [\text{K}]\Gamma_{\text{K}} + [\text{Rb}][\text{K}]q_{\text{KRb}}} \quad (1.14)$$

This is a limit to the fraction of absorbed photons that can go toward polarizing  $^3\text{He}$  nuclei, based on the characteristics of alkali-metal-buffer gas and alkali-metal-alkali-metal collisions.

The photon efficiency is a direct measure of the fraction of the angular momentum transferred by the pump laser to the Rb vapor that goes to polarizing  $^3\text{He}$ .

$$\eta_\gamma = \frac{[{}^3\text{He}] V dP_{\text{He}}/dt}{\Delta \phi} \quad (1.15)$$

If the model we have described were complete (the ground state collisions accounted for all the alkali-metal spin loss), then  $\eta_\gamma$  should equal  $\eta_{SE}$ . At all values of  $D$ , the measured spin-exchange efficiencies were in agreement with predictions based on previous measurements of  $k_{SE}^{\text{Rb-He}}$ ,  $k_{SE}^{\text{K-He}}$ ,  $\Gamma_{\text{Rb}}$ , and  $\Gamma_{\text{K}}$ [Babcock et al., 2003] (Fig. 1.2). Note the sharp increase in efficiency

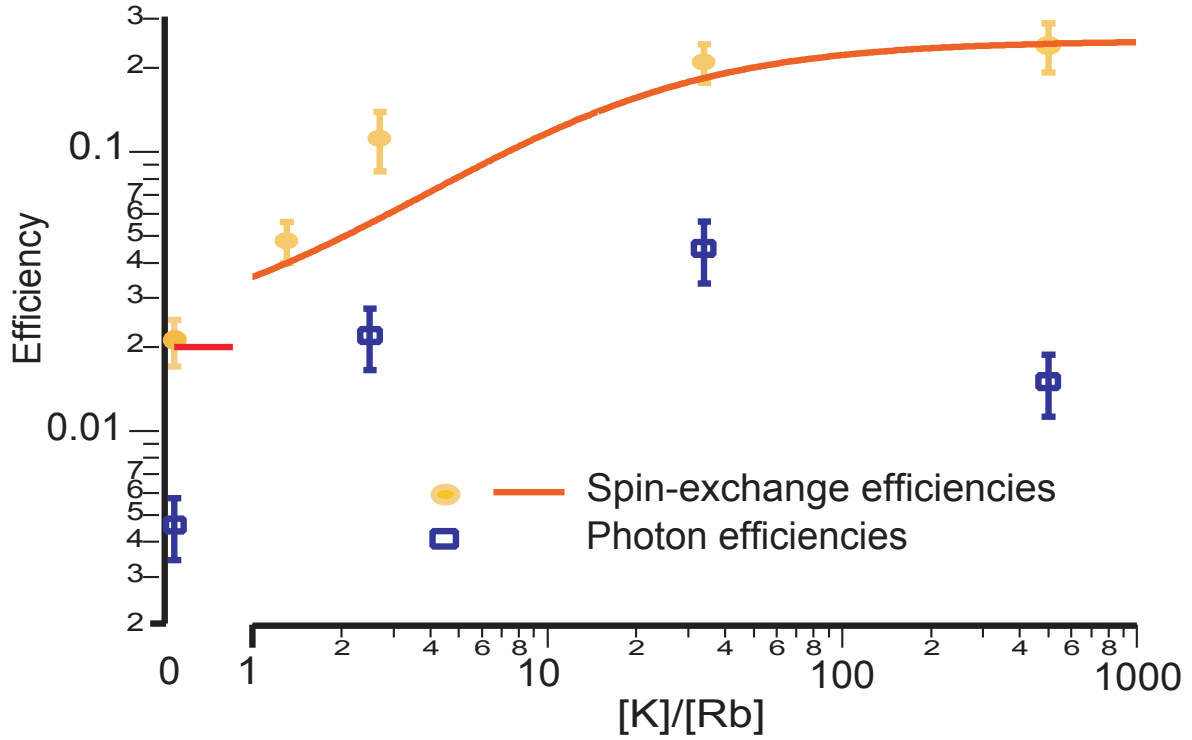


Figure 1.2 Spin-exchange and photon efficiencies for  $[\text{He}]=8$  amg cells with  $D=0$  to  $D=500$ . In all cases photon efficiencies are 5 to 10 times lower than the fundamental spin-exchange efficiencies. This implies that sources of alkali-metal spin relaxation are poorly understood.

as  $D$  increases from 0 to 10, which shows the advantage of hybrid SEOP. However, photon efficiencies were measured to be 5-10 times lower than spin-exchange efficiencies. This indicates that the majority of the alkali-metal spin relaxation is through unaccounted for mechanisms.

### 1.3.2 Limits to Alkali-Polarization

The experimenters noted that the cells could not be pumped to high  $P_A$ , even for low  $[\text{Rb}]$ , where  $R_p \gg \Gamma_A$ . Furthermore, from their data they deduced the alkali polarization achieved with infinite pumping power,  $P_{max}$  (Fig. 1.3).  $P_{max}$  is limited to  $\sim 0.91$  at low  $D$ , and drops dramatically with for  $D > 10$ . The optical pumping theory described above predicts  $P_{max} = 1$  in all cases. The reduced  $P_{max}$  implies that there is a light induced relaxation mechanism, that scales with pump laser intensity, limiting the maximum achievable polarization. If there were no light induced Rb

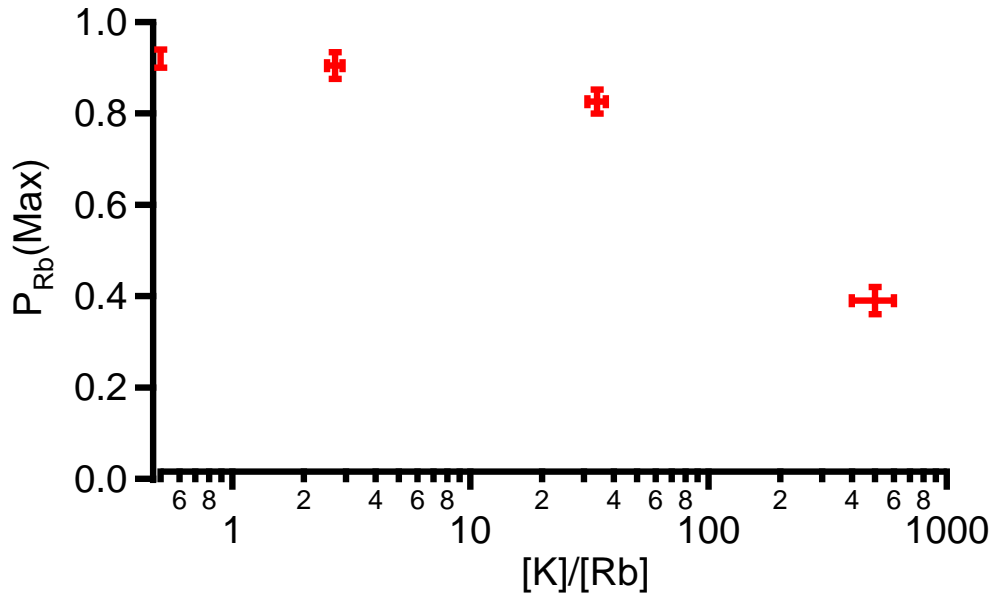


Figure 1.3 Alkali-metal polarization extrapolated to infinite pumping power,  $P_{max}$ , in cells with  $D$  ranging from 0 to 500. The decrease in  $P_{max}$  with increasing  $D$  suggests K absorption of pump light at the Rb resonance frequency may be a significant spin-relaxation process. The low  $P_{max}$  in the pure Rb cell indicates there must also be another pump induced relaxation process.

spin relaxation, then turning the pump laser power to infinity would overcome the spin relaxation, leading to  $P_{max}=1$ . This pump light induced relaxation mechanism also appears to increase with increasing  $D$ . One possible mechanism for light induced relaxation is absorption of  $\lambda=1$  pump light by atoms in the  $m_J=1/2$  ground state. It is possible that Rb-buffer-gas collisions slightly mix the  $^2P_{1/2}$  and  $^2P_{3/2}$  states, allowing weak absorption by the  $m_J=1/2$  state (Fig. 1.4). For hybrid cells, another candidate for light induced relaxation is absorption of the 795nm Rb D1 light by K atoms. This thesis describes experiments and theoretical calculations designed to characterize these previously unaccounted for sources of alkali relaxation

## 1.4 Summary of Thesis

Chapter 2 contains a description of the apparatus we use to perform SEOP, and the diagnostic tools we employ to characterize the Rb and K vapors during SEOP. In particular, we discuss two

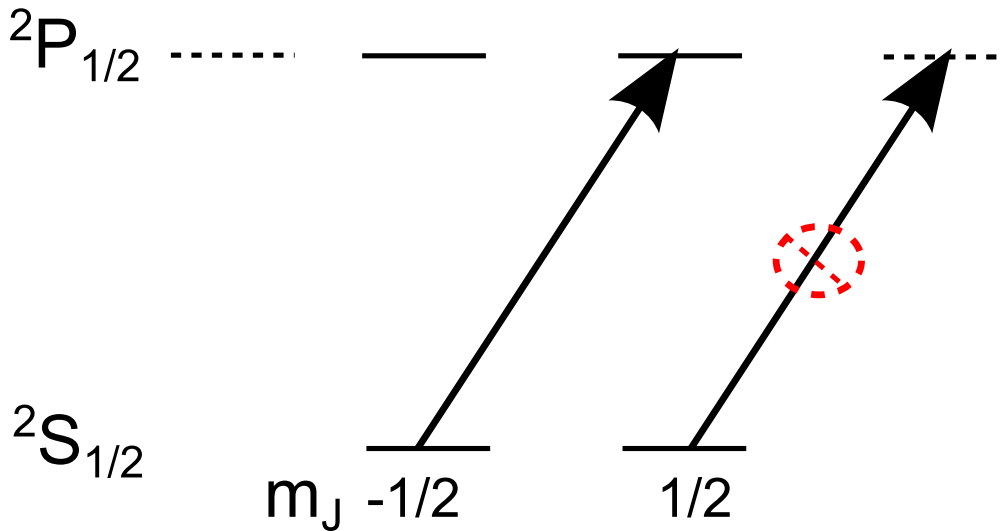


Figure 1.4 Modified energy level diagram of the ground state and first excited state of Rb (ignoring the hyperfine splittings). Rb-buffer gas collisions weakly mix the  $^2P_{1/2}$  and  $^2P_{3/2}$  states, giving the first excited state a small  $m_J=3/2$  component. This allows absorption of  $\lambda=1$  light by the  $m_J=1/2$  ground state sublevel.

variations of electron paramagnetic spectroscopy that have been used to measure  $P_{\text{Rb}}$ . In the course of performing the experiment describe in Chapter 3, we found that polarizations measured using the longitudinal EPR technique deviate systematically from those measured using longitudinal EPR spectroscopy and calibrated Faraday rotation measurements. Transverse EPR and Faraday rotation measurements are compatible, while  $P_{\text{Rb}}$  deduced from longitudinal EPR is always significantly higher.

Chapter 3 describes an experiment measuring the absorption of spin-up light near the D1 resonance by the spin-up ground state in violation of the atomic selection rules, due to Rb-buffer gas collisions. Measurements of the transmission of a circularly polarized probe beam, through Rb atoms with spin polarization  $\pm P_{\text{Rb}}$ , were made at a range of frequencies near the D1 resonance in three cells. One cell with 2.80 amg of  $\text{N}_2$  buffer gas, and two SEOP cells, with a small amount of  $\text{N}_2$  and  $^3\text{He}$  densities of 0.80 and 3.27 amg were studied. The transmission measurements, along with measurements of  $P_{\text{Rb}}$ , allowed us to extract the cross-section for dark state absorption in each cell. The dark state absorption in the SEOP cells scales linearly with the buffer gas density, confirming buffer-gas collisions as the mechanism that allows dark state absorption. Using the  $\text{N}_2$  cell

we found the cross-section due to Rb-N<sub>2</sub> collisions, allowing us to extract the cross-section due to Rb-<sup>3</sup>He collisions from the SEOP cell data

$$\frac{\sigma_d}{[\text{N}_2]} = 1.49 \pm 0.15 \times 10^{-17} \frac{\text{cm}^2}{\text{amg}} \quad (1.16)$$

$$\frac{\sigma_d}{[\text{He}]} = 1.10 \pm 0.12 \times 10^{-17} \frac{\text{cm}^2}{\text{amg}} \quad (1.17)$$

These small cross sections are shown, through modeling, to have a significant impact on optical pumping efficiency, particularly in cells with high [<sup>3</sup>He].

Chapter 4 describes measurements of the cross-section for absorption of Rb D1 resonance light by K atoms in the presence of <sup>3</sup>He and N<sub>2</sub> buffer gasses. Transmission measurements, near the Rb D1 resonance, were made in two cells containing K vapor and 0.924 and 2.93 amg [<sup>3</sup>He]. The cross-section for absorption was shown to be non-zero, and proportional to the buffer gas density. The result is summarized

$$\sigma_{\text{K-He}} = 2.19 \pm .39 \times 10^{-18} \frac{\text{cm}^2}{\text{amg}} [\text{He}] \quad (1.18)$$

$$\sigma_{\text{K-N}_2} = 8.8 \pm 7.6 \times 10^{-18} \frac{\text{cm}^2}{\text{amg}} [\text{N}_2] \quad (1.19)$$

With this K-<sup>3</sup>He cross-section and the dark-state absorption cross-section from the experiment describe in chapter 4 , the alkali-spin relaxation can be modeled for the conditions described in [Babcock et al., 2003], and a new prediction for  $P_{max}$  as a function of  $D$  made(Fig. 1.5). Modeling without these light induced relaxation mechanisms predicts  $P_{max} = 1$  for all  $D$ , whereas the modified model shows good agreement with the data at high  $D$ , where the K-<sup>3</sup>He cross-section is the dominant relaxation mechanism.

Chapter 5 describes a quantitative theoretical investigation of the effects of the N<sub>2</sub> quenching gas on optical pumping. A small amount N<sub>2</sub> is added to SEOP cells, as there is a large, resonantly enhanced, non-radiative quenching cross-section in collisions between excited Rb atoms and the N<sub>2</sub> buffer gas. We consider the possibility that a non-negligible nuclear spin precession occurs during the brief periods of time in which the alkali-metal atoms are in the excited state after absorbing photons and before undergoing quenching collisions with nitrogen molecules. This would allow

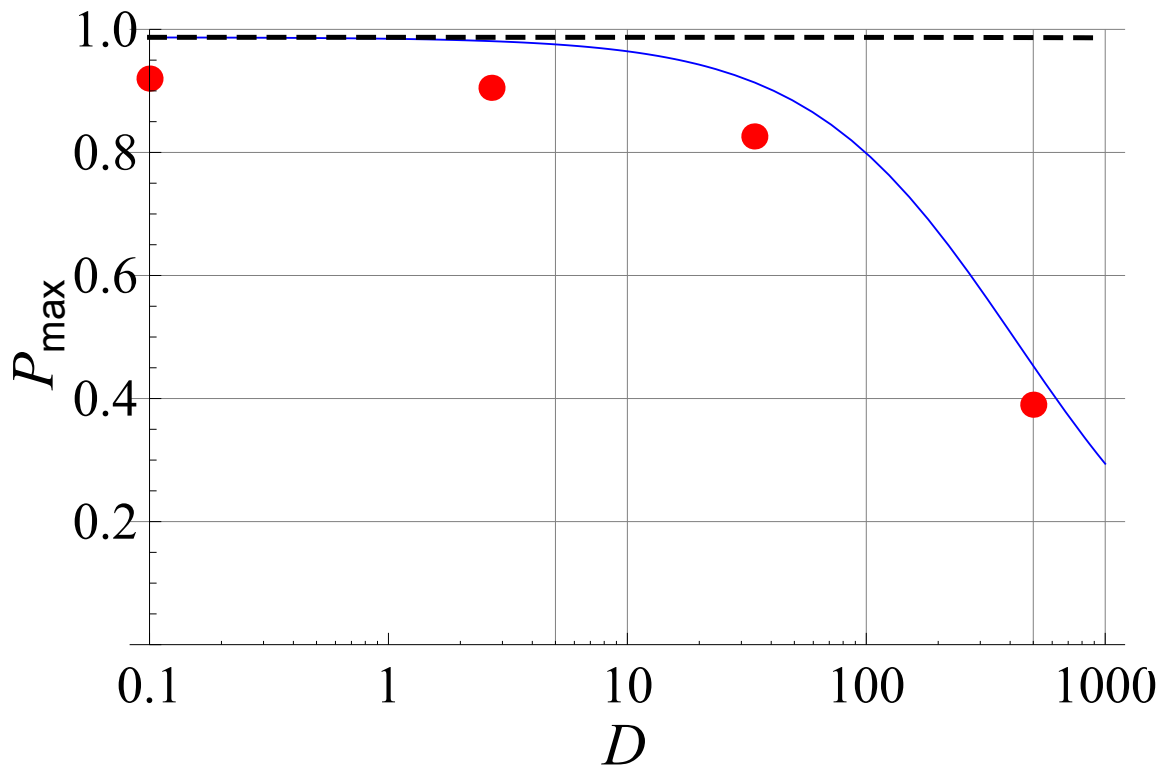


Figure 1.5 Comparison of measured[Babcock et al., 2003] and modeled maximum achievable alkali polarization as a function of K/Rb density ratio  $\mathcal{D}$ , with measured potassium absorption (solid blue) and without (dashed black), in an [He]=8.0 amg hybrid pumping cell, with a broadband,  $\Gamma = 1000\text{GHz}$ , pumping source.

relaxation of the Rb nuclear spins, which are coupled by the hyperfine interaction to the Rb electron spins. We analyze the effect of spontaneous emission and excited state nuclear spin relaxation as a function of  $\text{N}_2$  and  $^3\text{He}$  density. We find that for typical SEOP buffer gas densities, there is a small amount of nuclear spin lost by Rb atoms in the excited state, which should be taken into account when modeling the efficiency of optical pumping. The results of the thorough calculation are presented in a form in which they can be added simply to optical pumping models.

Chapter 6 uses a model including the additional relaxation methods described in the 3 previous chapters to describe a group of previous experimental results. First, we show that the effects described in chapter 3,4 and 5 allow us to properly model the photon efficiencies measured in [Babcock et al., 2003], except for the  $D=0$  cell(Fig. 1.6). We also compare the results of our

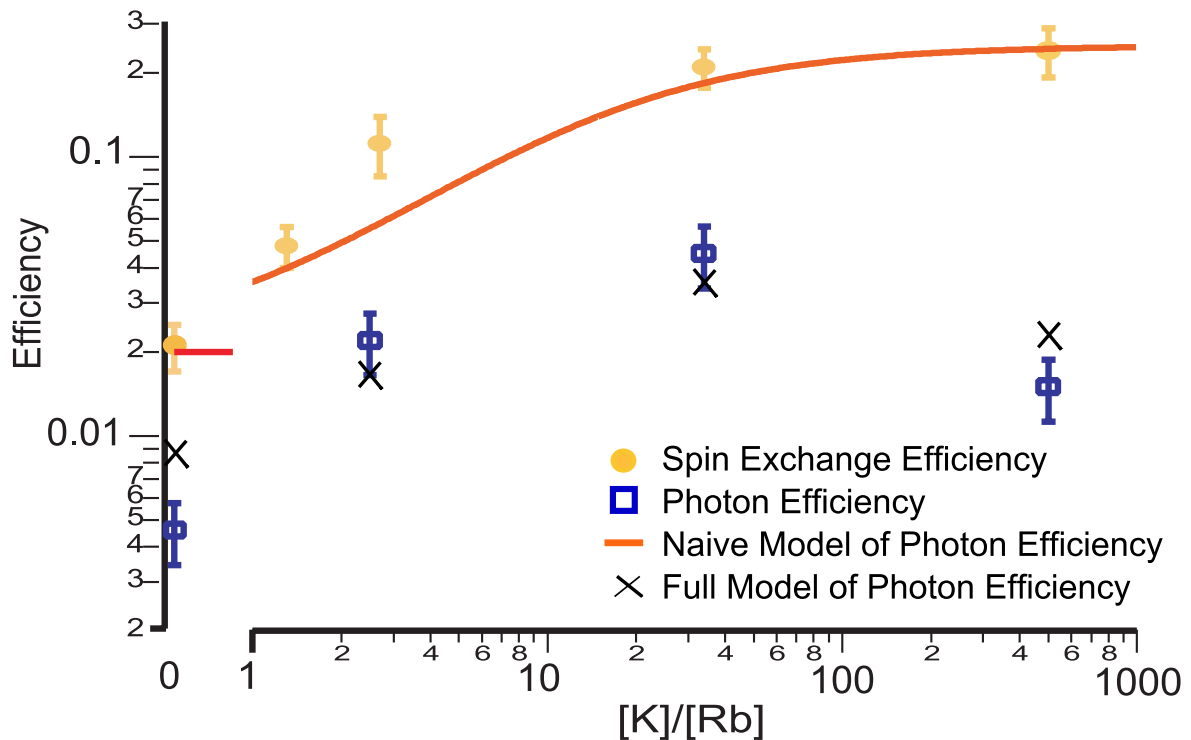


Figure 1.6 Measured spin exchange (yellow circles) and photon efficiencies (blue squares) for  $[\text{He}]=8$  amg cells with  $D=0$  to  $D=500$  [Babcock et al., 2003], along with a naive model for the photon efficiency (red-orange line) and a model that includes dark state absorption, excited state nuclear spin relaxation and potassium absorption at the Rb resonance (black crosses).

model to optical pumping data reported in [Chen et al., 2007] and [Chann et al., 2003]. Our model has much better qualitative agreement with this data than previous models, giving insight into the poor performance of broadband sources relative to narrowband pump sources and into the poor performance of optical pumping of pure Rb cells with narrowband sources. Also, we show that an understanding of laser heating effects of the type described in [Walter et al., 2001] is needed to produce accurate models.

## Chapter 2

# Spin Exchange Optical Pumping Apparatus

## 2.1 SEOP Apparatus

The basic apparatus needed for performing SEOP is very simple. A cell containing  $^3\text{He}$  and  $\text{N}_2$  gases and alkali metal liquid is heated in an oven to achieve the desired alkali-metal density. Then an intense pump laser tuned to the Rb D1 resonance polarizes the alkali-metal electron spins in the direction of a magnetic holding field applied by a set of field coils. Our apparatus has several other sets of magnetic field coils associated with Rb and  $^3\text{He}$  diagnostics, and probe lasers with associated optics and detectors. The apparatus is pictured in Fig. 2.1.

### 2.1.1 Cells

The five cells we used in these experiments were blown glass spheres or blown cylinders with flat windows. Three of cells were fabricated for neutron spin filters and were loaned to us by Tom Gentile, Wangchun Chen and Jeff Anderson at NIST-Gaithersberg. We also have one cell on loan from William Hersman at the University of New Hampshire.  $^3\text{He}$  SEOP cells are typically made out of Boron-free aluminosilicate glasses (GE180 or Corning1720), as these glasses have low neutron absorption cross-sections, low permeability to  $^3\text{He}$  and long  $^3\text{He}$  lifetimes. We purchased one cell from Triad Technologies, that contains only Rb and  $\text{N}_2$ , which is made from Pyrex. Characteristics of the cells used in the experiments described in this thesis are shown in Table 2.1

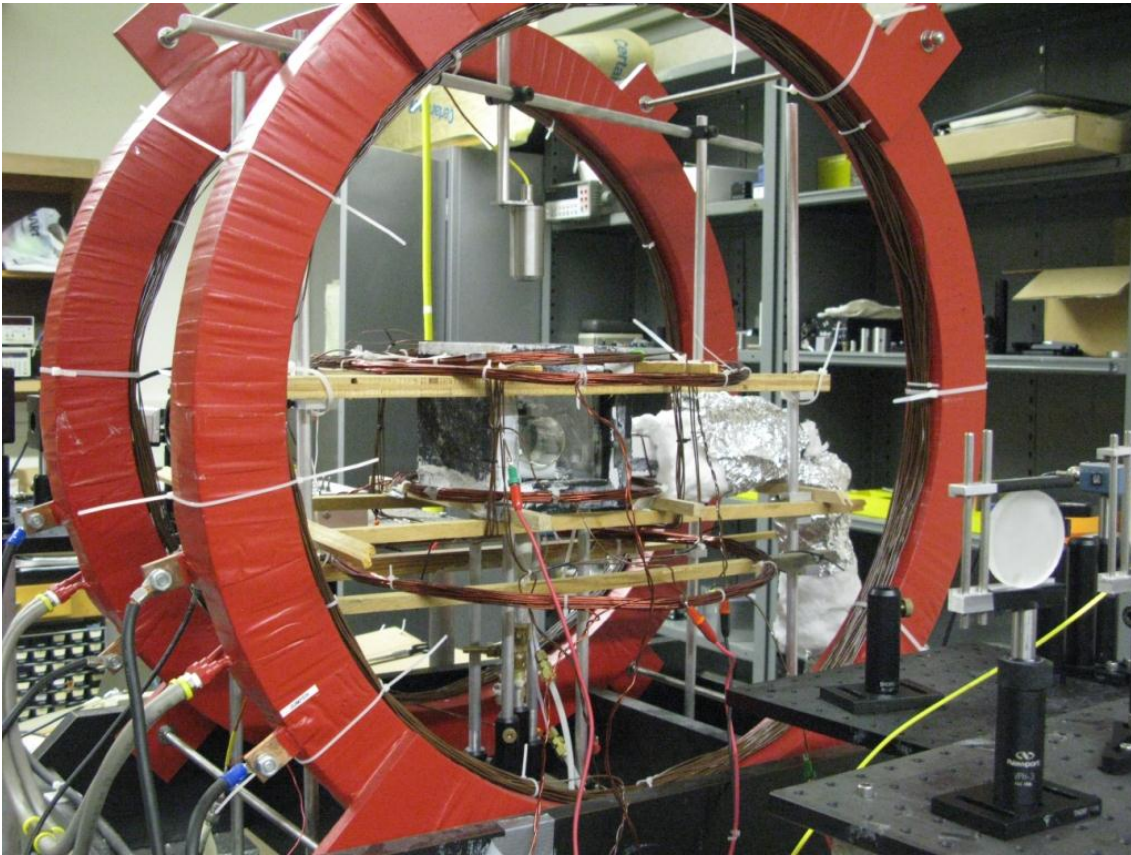


Figure 2.1 Picture of the SEOP apparatus.

Name	[ $^3\text{He}$ ]	[ $\text{N}_2$ ]	$T_1$	Alkali-Metal	Dimension (cm)	Glass	Source
Betty	.80	.07	240	Rb	4.5 x 4.9	GE180 and C1720	NIST
NHRb	3.27	.13	145	Rb	3.5	GE180	UNH
$\text{N}_2$		2.8		Rb	4.5	Pyrex	Triad
K1	.924	.063		K	5.7	GE180	NIST
K2	2.87	.063		K	4.8	GE180	NIST

Table 2.1 Characteristics of the vapor cells used in the experiments described in this thesis. The dimensions listed are  $D$ =diameter for the spherical cells, and  $D$ =diameter  $\times$   $L$ =length for the cylindrical cell.

### 2.1.2 Pump Laser

The pump lasers used were frequency narrowed Nuvonyx diode array bars (FNDABs). The diode array bars contain  $\sim 20$  emitters in a line, that deliver high power (50 W), but whose free running wavelengths typically span several nm, giving a linewidth of  $\sim 1000$  GHz. In an external cavity of the type described in [Babcock et al., 2005a], the output power is typically reduced by half, and the linewidth is reduced to  $\sim 100$  GHz. The cavity is a Littrow cavity, where the pump laser is aligned at grazing incidence to a diffraction grating (typically 2400 grooves/mm) such that the first order diffracted beam returns to the laser. A telescope is placed inside the cavity, imaging the bar onto the diffraction grating. This insures that the diffracted beam is imaged back onto the bar, feeding each emitter back to itself. The pump laser is pictured in Fig. 2.2.

### 2.1.3 Oven

The oven we used is a hot air flow-through oven, constructed from 1/2" calcium silicate insulation board held together with furnace cement, with 1/4" glass windows (Fig. 2.3). Air is blown across a heating element and through the oven to a small outlet on the far side. Thinner windows exhibit problems with etalon interference fringing of the probe beam transmission. A KBr window on the top of the oven transmits thermal radiation from black painted high temperature tape placed on top of the cell to an IR sensor. The output of the sensor is fed to a PID feedback circuit that controls the duty cycle of the heating element. The IR sensor was calibrated using a thermistor temporarily attached to a cell in the oven. If a thermistor is left on the cell during SEOP, it creates local magnetic field gradients that reduce the coherence time of the  $^3\text{He}$  spins, interfering with  $^3\text{He}$  polarimetry.

### 2.1.4 Coils

The coils used are water cooled 73.7 cm diameter pair of Helmholtz coils (Fig. 2.1) capable of producing fields up to 150 G. Typical holding fields are 10-50 G. There is a separate, uncooled coils, wound on the inside of the holding field coils that is ramped for EPR spectroscopy (described below). In addition

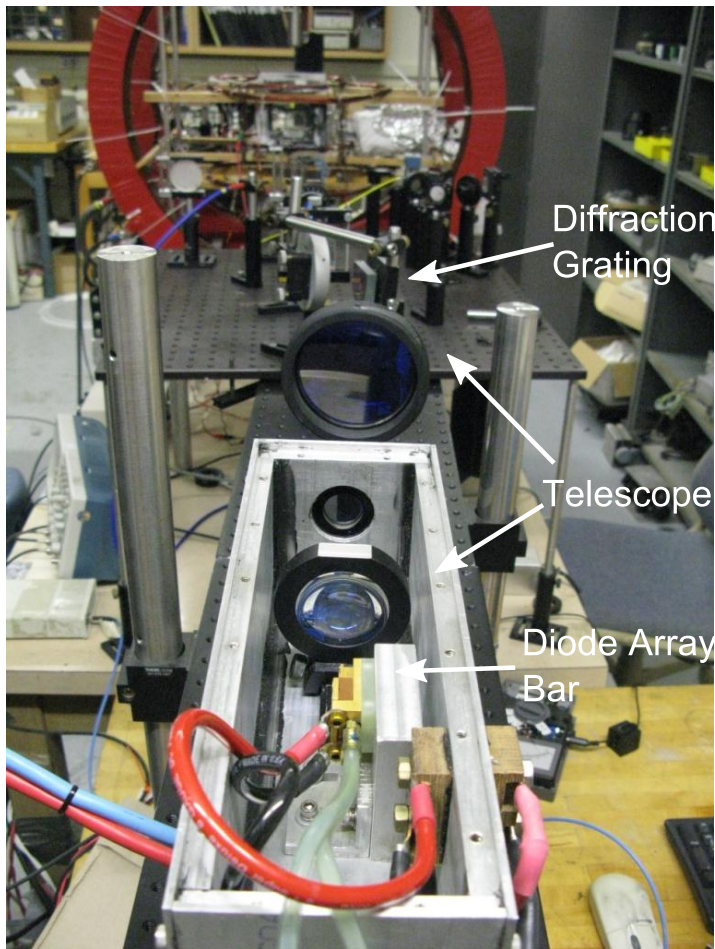


Figure 2.2 Picture of the pump laser, and its external cavity. A telescope is placed inside the cavity, imaging the diode array bar on the diffraction grating. This insures that the diffracted beam is imaged back onto the bar, feeding each emitter back to itself.

## 2.2 Diagnostics

A key feature of our apparatus is diagnostics for the alkali-metal and  $^3\text{He}$  gases. These include diagnostics measuring the average Rb and  $^3\text{He}$  spins ( $P_{\text{Rb}}$  and  $P_{\text{He}}$ ), the gas densities ( $[\text{Rb}]$ ,  $[\text{He}]$ , and  $[\text{N}_2]$ ) and the lifetime of  $^3\text{He}$  spins.

### 2.2.1 Probe Lasers

We use weak probe beams as diagnostic tools, to measure properties of the alkali-metals without significantly perturbing pump laser driven equilibria. These are all external cavity diode lasers

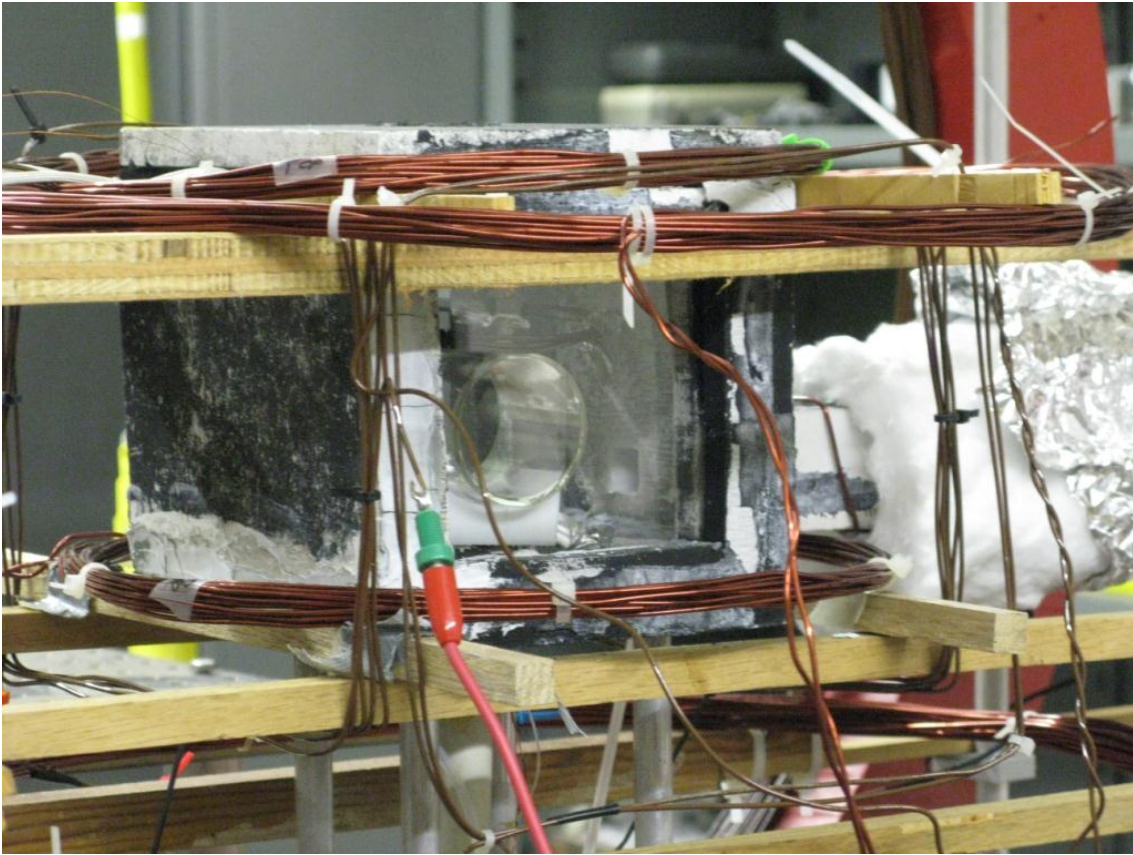


Figure 2.3 Picture of the calcium silicate oven. The hot air flows in through the arm on the right. The temperature sensor is unseen, just above the cell.

(ECDLs), in home-built Littman-Metcalf cavities([Littman and Metcalf, 1978]). In the Littman-Metcalf configuration, the off-the-shelf diode is aligned at grating incidence to a diffraction grating (typically a 1800 grooves/mm holographic grating), which acts as the frequency selective element in the cavity. The first order diffracted beam is sent to a mirror, and then reflected back onto the grating, sending the first order of the first order beam back into the laser diode. The angle of the feedback mirror controls what frequency of light is directed back into the diode; The cavity losses are at a minimum at the feedback frequency, pulling the laser output to that frequency allowing frequency control of the diode. The grating efficiency depends on the incident polarization of the probe beam, so a  $\lambda/2$  plate is used to control the feedback fraction. This may cause problems, since the polarization of the feedback is not the same as the output polarization for most settings of the

$\lambda/2$  plate, but it works well enough in practice. Fine tuning of the output frequency is achieved with a mixture of current and temperature tuning.

To probe the Rb D1 resonance we use a temperature controlled, 50 mW Hitachi HL7851G diode, which can be tuned from  $\sim 788\text{nm}$  to  $799\text{ nm}$ . For the Rb D2 resonance, we used a 70 mW Blue Sky Research 785nm Circulaser diode, which could tune from  $\sim 777\text{nm}$  to  $783\text{nm}$ . We used a highly AR-coated Eagleyard EYP-RWE-0790-04000-0750-SOT01-0000 diode to probe the K resonances. This laser has a very large tuning range,  $\sim 750\text{nm}$  to  $790\text{ nm}$ , and has more stable feedback and is easier to tune using the feedback mirror, as compared to the other probe lasers.

## 2.2.2 Transverse EPR Spectroscopy

We measure  $P_{\text{Rb}}$  using the method of transverse electron paramagnetic resonance spectroscopy (EPR) developed in Happer's lab at Princeton ([Young et al., 1997, Baranga et al., 1998]). An RF field is applied, perpendicular to the magnetic holding field. The magnetic holding field is then swept to bring the Rb ground-state sublevel transitions on resonance with the RF field, one after the other. When the RF field is resonant with the transition between two ground-state sub-levels, a transverse spin oscillating at the RF frequency is generated, the magnitude of which is proportional the population difference between the two states. The transverse spin is measured with a probe beam as the magnetic holding field is swept and a spectrum is produced (Fig. 2.4). From the areas of the EPR peaks, the populations of the sub-levels can be reconstructed and  $P_{\text{Rb}}$  can be calculated.

### 2.2.2.1 Theory

For each Rb isotope, the hyperfine interaction splits the ground state into two sets of states (manifolds) with different values of the total angular momentum  $F = I \pm 1/2$ . For the holding field values used during EPR spectroscopy (typically  $\sim 50\text{G}$ ), EPR peaks corresponding to subsequent transitions between pairs of states in the same manifold ( $|Fm\rangle \rightarrow |Fm-1\rangle$  and  $|Fm-1\rangle \rightarrow |Fm-2\rangle$  transitions) are very well separated. The  $|Fm\rangle \rightarrow |Fm-1\rangle$  and  $|F'm\rangle \rightarrow |F'm-1\rangle$

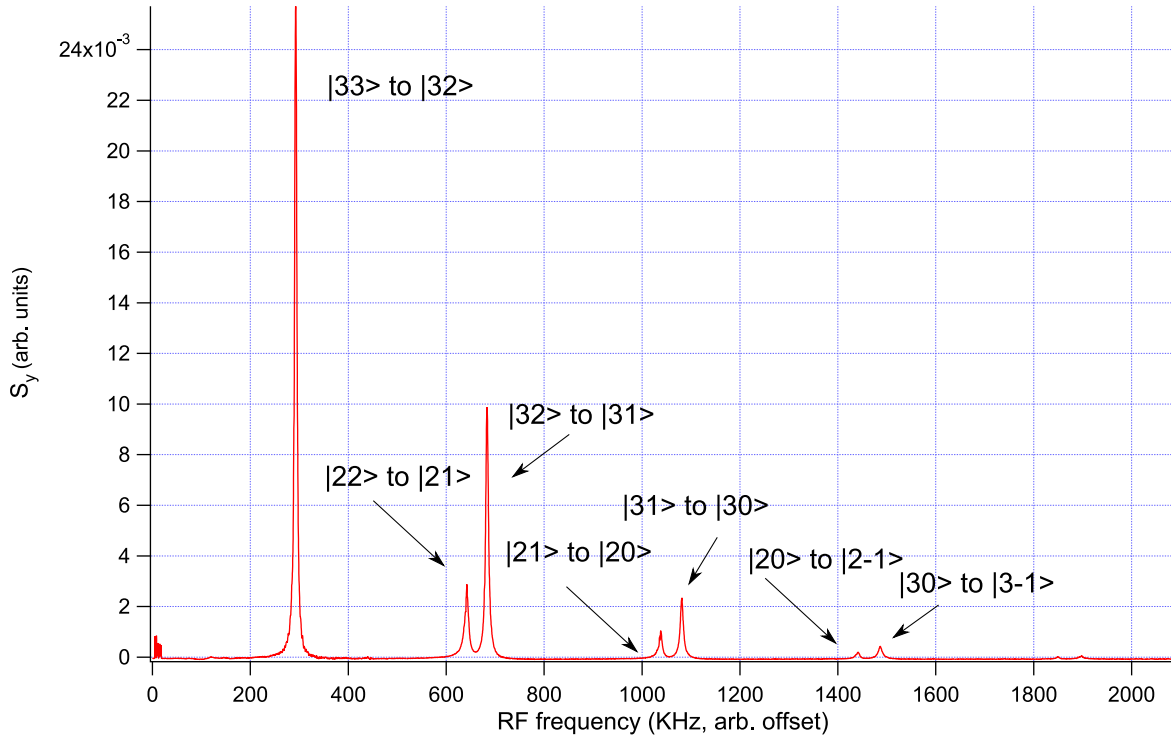


Figure 2.4 Transverse EPR spectrum taken at  $\sim T=150^\circ\text{C}$  in Betty, with  $P_{\text{Rb}} \approx 0.82$ . Each peak in the spectrum is due to the RF field driving one ground-state sub-level transition.

transitions between pairs of states with the same azimuthal quantum numbers in the two different manifolds typically overlap, and we will consider the case of driving one transition in each manifold.

The interaction between the oscillating field and the atomic states is characterized by

$$H^a = \begin{bmatrix} E_m & \epsilon_{Fm} e^{-i\omega t} \\ \epsilon_{Fm}^* e^{i\omega t} & E_{m-1} \end{bmatrix} \quad (2.1)$$

for states  $|F m\rangle, |F m-1\rangle$  in the upper manifold with  $F = a = I + 1/2$ , where  $E_m > E_{m-1}$ , and

$$H^b = \begin{bmatrix} E_m & \epsilon_{Fm} e^{i\omega t} \\ \epsilon_{Fm}^* e^{-i\omega t} & E_{m-1} \end{bmatrix} \quad (2.2)$$

for states in the lower manifold with  $F = b = I - 1/2$ , where  $E_m < E_{m-1}$ . The coupling strength  $\epsilon$  is

$$\epsilon_{Fm} = \langle F m_f | g_s \mu_B B_x S_x | F' m'_f \rangle \quad (2.3)$$

We want to calculate the time evolution of the off diagonal elements of the density matrix, from which we can calculate the transverse spin induced by the RF B-field. If we assume that the RF field is weak, so that the populations in the two states,  $\rho_m$  and  $\rho_{m-1}$ , are unchanged by the driving field, for the  $F = a$  manifold

$$i\frac{d\rho_{m,m-1}}{dt} = [H^a, \rho]_{m,m-1} = \hbar E_m \rho_{m,m-1} + \epsilon_{am} e^{-i\omega t} \rho_{m-1} - \hbar E_{m-1} \rho_{m,m-1} - \epsilon_{am} e^{-i\omega t} \rho_m \quad (2.4)$$

adding decoherence

$$= (\omega_m - \omega_{m-1})\rho_{m,m-1} + (\rho_{m-1} - \rho_m)\epsilon_{am} e^{-i\omega t} - \frac{i\gamma_{am}}{2}\rho_{m,m-1} \quad (2.5)$$

$$= \omega_{m,m-1}\rho_{m,m-1} + (\rho_{m-1} - \rho_m)\epsilon_{am} e^{-i\omega t} - \frac{i\gamma_{am}}{2}\rho_{m,m-1} \quad (2.6)$$

where  $\omega_{m,m-1} = \omega_m - \omega_{m-1}$ . Assuming we can write the decoherence  $\rho_{m,m-1} = \sigma_{m,m-1} e^{-i\omega_{m,m-1}t}$ , we get

$$i\frac{d\sigma_{m,m-1}}{dt} = (\rho_{m-1} - \rho_m)\epsilon_{am} e^{-i(\omega - \omega_{m,m-1})t} - \frac{i\gamma_{am}}{2}\sigma_{m,m-1} \quad (2.7)$$

guessing  $\sigma_{m,m-1} = A e^{-i\Delta t}$ , where the detuning  $\Delta_a = \omega - \omega_{m,m-1}$ , we can solve this to get

$$\rho_{m,m-1}^a = \frac{(\rho_{m-1}^a - \rho_m^a)\epsilon_{am}}{\Delta_a + \frac{i\gamma_{am}}{2}} e^{-i\omega t} = \epsilon_{am} (\rho_{m-1}^a - \rho_m^a) \frac{\Delta_a - \frac{i\gamma_{am}}{2}}{\Delta_a^2 + \frac{\gamma_{am}^2}{4}} e^{-i\omega t} \quad (2.8)$$

To calculate the matrix element  $\epsilon_{Fm}$ , we look at the potential using the projection theorem

$$g_s \mu_B B_x S_x = g_s \mu_B B_x \frac{S \cdot F}{F^2} F_x = g_s \mu_B B_x \frac{1}{2} \frac{F^2 + S^2 - I^2}{F^2} F_x \quad (2.9)$$

Plugging in  $S = 1/2$  and  $F = I \pm 1/2$

$$g_s \mu_B B_x S_x = \pm \frac{g_s \mu_B B_x}{2I + 1} F_x = \pm \frac{g_s \mu_B B_x}{2(2I + 1)} (F_+ + F_-) \quad (2.10)$$

These projection theorem matrix elements are only non zero for  $F' = F$  and  $m'_f = m_f \pm 1$ . For  $m'_f = m_f - 1$

$$\epsilon_{Fm} = \pm \frac{1}{2} \frac{g_s \mu_B B_x}{2I + 1} \sqrt{F(F + 1) - m(m - 1)} \quad (2.11)$$

and the coherence in the  $F = a$  manifold is

$$\rho_{m,m-1}^a = \frac{1}{4} \frac{g_s \mu_B B_x}{2I + 1} \sqrt{a(a + 1) - m(m - 1)} (\rho_{m-1}^a - \rho_m^a) \frac{\Delta_a - \frac{i\gamma_{am}}{2}}{\Delta_a^2 + \frac{\gamma_{am}^2}{4}} e^{-i\omega t} \quad (2.12)$$

For transitions between states in the  $F = b$  manifold

$$i \frac{d\rho_{m,m-1}}{dt} = \omega_{m,m-1} \rho_{m,m-1} + (\rho_{m-1} - \rho_m) \epsilon_{bm} e^{i\omega t} - \frac{i\gamma_{bm}}{2} \rho_{m,m-1} \quad (2.13)$$

defining  $\Delta_b = \omega + \omega_{m,m-1}$ , the solution is

$$\rho_{m,m-1}^b = -\frac{1}{4} \frac{g_s \mu_B B_x}{2I+1} \sqrt{b(b+1) - m(m-1)} (\rho_{m-1}^b - \rho_m^b) \frac{\Delta_b + \frac{i\gamma_{bm}}{2}}{\Delta_b^2 + \frac{\gamma_{bm}^2}{4}} e^{-i\omega t} \quad (2.14)$$

The measurable quantity is [Baranga et al., 1998]

$$\langle S_x \rangle = Tr(\rho S_x) = \frac{1}{2(2I+1)} Tr(\rho F_x) \quad (2.15)$$

$$= \frac{\sqrt{a(a+1) - m(m-1)}}{2I+1} (\rho_{m,m-1}^a + \rho_{m-1,m}^a) + \frac{\sqrt{b(b+1) - m(m-1)}}{2I+1} (\rho_{m,m-1}^b + \rho_{m-1,m}^b) \quad (2.16)$$

$$= \frac{1}{8} \frac{g_s \mu_B B_x}{(2I+1)^2} \left[ (a(a+1) - m(m-1)) (\rho_{m-1}^a - \rho_m^a) \left[ \frac{\Delta_a (e^{i\omega t} + e^{-i\omega t})}{\Delta_a^2 + \frac{\gamma_{am}^2}{4}} + \frac{i\frac{\gamma_{am}}{2} (e^{i\omega t} - e^{-i\omega t})}{\Delta_a^2 + \frac{\gamma_{am}^2}{4}} \right] \right. \\ \left. + (b(b+1) - m(m-1)) (\rho_{m-1}^b - \rho_m^b) \left[ \frac{\Delta_b (e^{i\omega t} + e^{-i\omega t})}{\Delta_b^2 + \frac{\gamma_{bm}^2}{4}} + \frac{i\frac{\gamma_{bm}}{2} (e^{-i\omega t} - e^{i\omega t})}{\Delta_b^2 + \frac{\gamma_{bm}^2}{4}} \right] \right] \quad (2.17)$$

$$= \frac{1}{8} \frac{g_s \mu_B B_x}{(2I+1)^2} \left[ (a(a+1) - m(m-1)) (\rho_{m-1}^a - \rho_m^a) \left[ \frac{2\Delta_a \cos \omega t - \gamma_{am} \sin \omega t}{\Delta_a^2 + \frac{\gamma_{am}^2}{4}} \right] \right. \\ \left. + (b(b+1) - m(m-1)) (\rho_{m-1}^b - \rho_m^b) \left[ \frac{-2\Delta_b \cos \omega t + \gamma_{bm} \sin \omega t}{\Delta_b^2 + \frac{\gamma_{bm}^2}{4}} \right] \right] \quad (2.18)$$

and, similarly

$$\langle S_y \rangle = -\frac{1}{8} \frac{g_s \mu_B B_x}{(2I+1)^2} \left[ (a(a+1) - m(m-1)) (\rho_{m-1}^a - \rho_m^a) \left[ \frac{2\Delta_a \sin \omega t + \gamma_{am} \cos \omega t}{\Delta_a^2 + \frac{\gamma_{am}^2}{4}} \right] \right. \\ \left. + (b(b+1) - m(m-1)) (\rho_{m-1}^b - \rho_m^b) \left[ \frac{2\Delta_b \sin \omega t + \gamma_{bm} \cos \omega t}{\Delta_b^2 + \frac{\gamma_{bm}^2}{4}} \right] \right] \quad (2.19)$$

### 2.2.2.2 EPR Apparatus

In our apparatus, one SRS DS345 function generator produces an RF driving signal (at  $\sim 26$  MHz), while a second function generator produces a reference signal detuned from the driving

signal by  $\sim 80$  KHz. The frequencies of the resonances can be approximated by calculating the energy shifts of the ground-state sub-levels due to  $B_z$  using the Breit-Rabi formula [Ramsey, 1953]

$$E_m = -\frac{E_{hf}}{2(2I+1)} - g_I \mu_B B_z m \pm \frac{1}{2} E_{hf} \sqrt{1 + \frac{4m}{2I+1} \frac{(g_I - g_J) \mu_B B_z}{E_{hf}} + \left( \frac{(g_I - g_J) \mu_B B_z}{E_{hf}} \right)^2} \quad (2.20)$$

where  $E_{hf}$  is the hyperfine energy splitting and the  $(\pm)$  signs are for the  $F = I \pm 1/2$  hyperfine manifolds. Expanding this to second order in the field gives

$$E_m \approx -\frac{E_{hf}}{2(2I+1)} - g_I \mu_B B_z m \pm \frac{1}{2} E_{hf} \left[ 1 + \frac{2m}{2I+1} \frac{(g_I - g_J) \mu_B B_z}{E_{hf}} + \frac{1}{2(2I+1)^2} \left( \frac{(g_I - g_J) \mu_B B_z}{E_{hf}} \right)^2 (1 - 4m^2) \right] \quad (2.21)$$

Then, we can find the transition frequency between two states

$$\frac{E_m - E_{m-1}}{\hbar} \approx \frac{g_I \mu_B B_z}{\hbar} \pm \frac{E_{hf}}{\hbar} \left[ \frac{1}{2I+1} \frac{(g_I - g_J) \mu_B B_z}{E_{hf}} + \frac{1}{(2I+1)^2} \left( \frac{(g_I - g_J) \mu_B B_z}{E_{hf}} \right)^2 (1 - 2m) \right] \quad (2.22)$$

To first order, and ignoring the contribution from the nuclear magnetic moment ( $g_I \ll g_J$ ) all the transitions of a given isotope have the same frequency

$$|\omega_{0I}| = \frac{g_J \mu_B B_z}{\hbar(2I+1)} \quad (2.23)$$

and we can approximate Eq. 2.22

$$\frac{E_m - E_{m-1}}{\hbar} = |\omega_{m,m-1}| \approx |\omega_{0I}| + \frac{|\omega_{0I}|^2}{\omega_{hf}} (1 - 2m) \pm \frac{g_I \mu_B B_z}{\hbar} \quad (2.24)$$

So, the difference in the resonant frequencies for subsequent transitions in the same hyperfine manifold is

$$|\omega_{m,m-1} - \omega_{m-1,m-2}| \approx \frac{2\omega_{0I}^2}{\omega_{hf}} \quad (2.25)$$

and the difference in the resonant frequencies for transitions with the same azimuthal quantum numbers  $m$ , but different  $F$  is

$$|\omega_{F m,m-1} - \omega_{F' m,m-1}| = \frac{g_I \mu_B B_z}{\hbar} \quad (2.26)$$

The driving signal is split and one part is sent through a voltage controlled attenuator to a pair of 9-cm-diameter coils separated by 7cm. The other part of the driving signal is mixed with the reference signal to produce an 80 KHz reference for an SRS SR830 digital lock-in amplifier. The 780 nm probe beam is tuned 1-2 nm off resonance, sent through a linear polarizer, and directed through the cell perpendicular to the RF field at an angle of  $\sim 15^\circ$  to the holding field. When the driving field is on resonance with a ground-state sub-level transition, the polarization of the probe is modulated by the atomic coherence at the RF frequency. The polarization modulation is converted to intensity modulation with a second linear polarizer oriented at  $45^\circ$  with respect of the probe polarization direction, and the probe intensity is detected with a New Focus 1621 nanosecond photodetector. The output of the detector is sent through two RF amplifiers and then demodulated to 80 KHz by mixing it with the reference signal. The demodulated signal is sent to the input of the lock-in amplifier(Fig. 2.5).

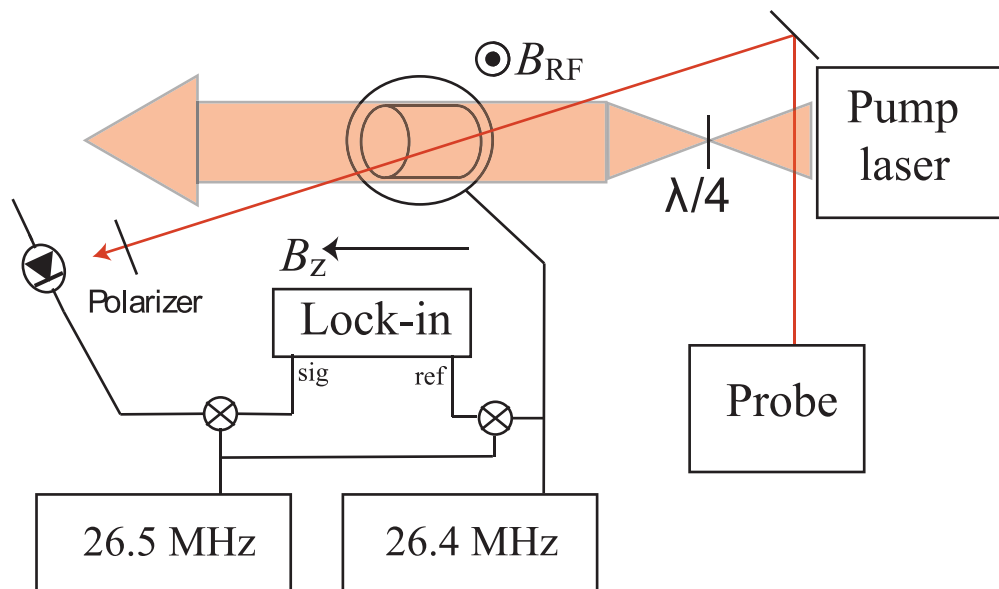


Figure 2.5 Measurement of polarization via transverse EPR spectroscopy. As the DC magnetic field is swept to match the Rb Zeeman EPR frequencies, the index of refraction of the Rb atoms becomes modulated at the 26.4-MHz RF driving frequency, thus modulating the polarization of the probe laser. This modulation is detected and demodulated by the lock-in amplifier. The Rb polarization is deduced from the ratio of areas of the EPR resonances.

The probe laser is directed perpendicular to the RF field, so the transverse component is in the y-direction, and the polarization of the beam is sensitive to  $S_y$ . A linearly polarized beam that propagates in the y-direction through a medium with some spin  $S_y$ , will have its polarization rotated by an angle proportional to  $S_y l$ , where  $l$  is the path length through the vapor. Thus, a measure of the polarization rotation of the beam is a relative measurement of the spin  $S_y$ . From Eq. 2.19, the polarization modulation induced in the probe by driving a single resonance is proportional to

$$(F(F+1) - m(m-1))(\rho_{Fm-1} - \rho_{Fm}) \left[ \frac{2\Delta_{Fm} \sin \omega t + \gamma_{Fm} \cos \omega t}{\Delta_{Fm}^2 + \frac{\gamma_{Fm}^2}{4}} \right] \quad (2.27)$$

This signal is demodulated, and the phase of the lock-in reference signal can be chosen (experimentally this is done by hand) to produce a lock-in output that is Lorentzian in RF frequency

$$L = C (F(F+1) - m(m-1))(\rho_{Fm-1} - \rho_{Fm}) \frac{\gamma_{Fm}}{\Delta_{Fm}^2 + \frac{\gamma_{Fm}^2}{4}} \quad (2.28)$$

where C contains factors including the RF field strength, photodiode and lock-in gains which are the same for all resonances. Note that the spin  $S_y$  induced by driving a sub-level transition in either hyperfine manifold has the same phase relative to the driving field, producing EPR spectra where the peaks are all in the same direction. In [Young et al., 1997, Baranga et al., 1998], they measured  $S_x$ . The responses of  $S_x$  to driving transitions in the two manifolds are out of phase with each other, producing EPR spectra where peaks have alternating sign. It is useful to align the probe beam in either the x-z or y-z plane, as any other orientation will measure a combination of  $S_x$  and  $S_y$ . For a combination, the responses to driving in the two manifolds will have a relative phase between zero and  $\pi/2$ , leading to complicated analysis.

### 2.2.2.3 Analysis

Typically the linewidths  $\gamma$  of different ground-state sub-level resonances are different, but for Lorentzian peaks the area under successive peaks is independent of the linewidth. In our experiment, we observed asymmetric, non-Lorentzian EPR peaks. We believe this is due to inhomogeneous broadening due to magnetic field gradients in the cell, since the effect was largely eliminated

by using a shim coil to produce a  $\text{dB}_z/\text{dz}$  gradient. The resulting EPR peaks were fit to Voigt profiles. Since the individual atomic responses still have Lorentzian frequency profiles, the area of the peaks should still be independent of the linewidths.

Thus, the ratio of the area of two successive peaks from driving transitions in the same manifold is

$$A_m = \frac{(F(F+1) - m(m-1))}{(F(F+1) - (m-1)(m-2))} \frac{\rho_{Fm} - \rho_{Fm-1}}{\rho_{Fm-1} - \rho_{Fm-2}} \quad (2.29)$$

From the ratios of successive peaks it is possible to extract information about the populations  $\rho_{Fm}$ , without calibrating the detection apparatus to determine the absolute magnitude of the atomic response. This is particularly simple when the Rb spins are in spin temperature equilibrium [Anderson et al., 1959]. Spin temperature is characterized by the spin temperature parameter  $\beta$ , where  $\rho_m = e^{-m\beta}$  and  $\frac{\rho_m}{\rho_{m-1}} = e^{-\beta}$ . Thus, we can write

$$\frac{\rho_m - \rho_{m-1}}{\rho_{m-1} - \rho_{m-2}} = \frac{\rho_m(1 - \frac{\rho_{m-1}}{\rho_m})}{\rho_{m-1}(1 - \frac{\rho_{m-2}}{\rho_{m-1}})} = \frac{\rho_m(1 - e^{-\beta})}{\rho_{m-1}(1 - e^{-\beta})} = \frac{\rho_m}{\rho_{m-1}} = e^{-\beta} \quad (2.30)$$

In principle,  $\beta$  can then be deduced from the ratio of the areas of any two successive peaks,

$$A_m = \frac{(F(F+1) - m(m-1))}{(F(F+1) - (m-1)(m-2))} e^{-\beta} \quad (2.31)$$

and all the sub-level populations are known. The spin polarization can be expressed

$$P = \tanh\left(\frac{\beta}{2}\right) = \frac{e^{\beta} - 1}{e^{\beta} + 1} \quad (2.32)$$

However, for the magnetic holding fields used, the  $|F m\rangle \rightarrow |F m-1\rangle$  and  $|F-1 m\rangle \rightarrow |F-1 m-1\rangle$  peaks are not typically well separated. Thus, for  $^{85}\text{Rb}$ ,  $\beta$  must be extracted from the ratio of the area of the  $|33\rangle \rightarrow |32\rangle$  peak to the sum of the areas of the unresolved  $|32\rangle \rightarrow |31\rangle$  and  $|22\rangle \rightarrow |21\rangle$  peaks.

The magnitude of the applied RF field is decreased, and the detuning of the probe beam increased, until the measured polarization is found to be insensitive to changes in those parameters. Careful shielding of the probe laser was found to be necessary, to prevent pick up of the RF on the drive current of the diode. It was also noted that higher RF power can be used at lower densities.

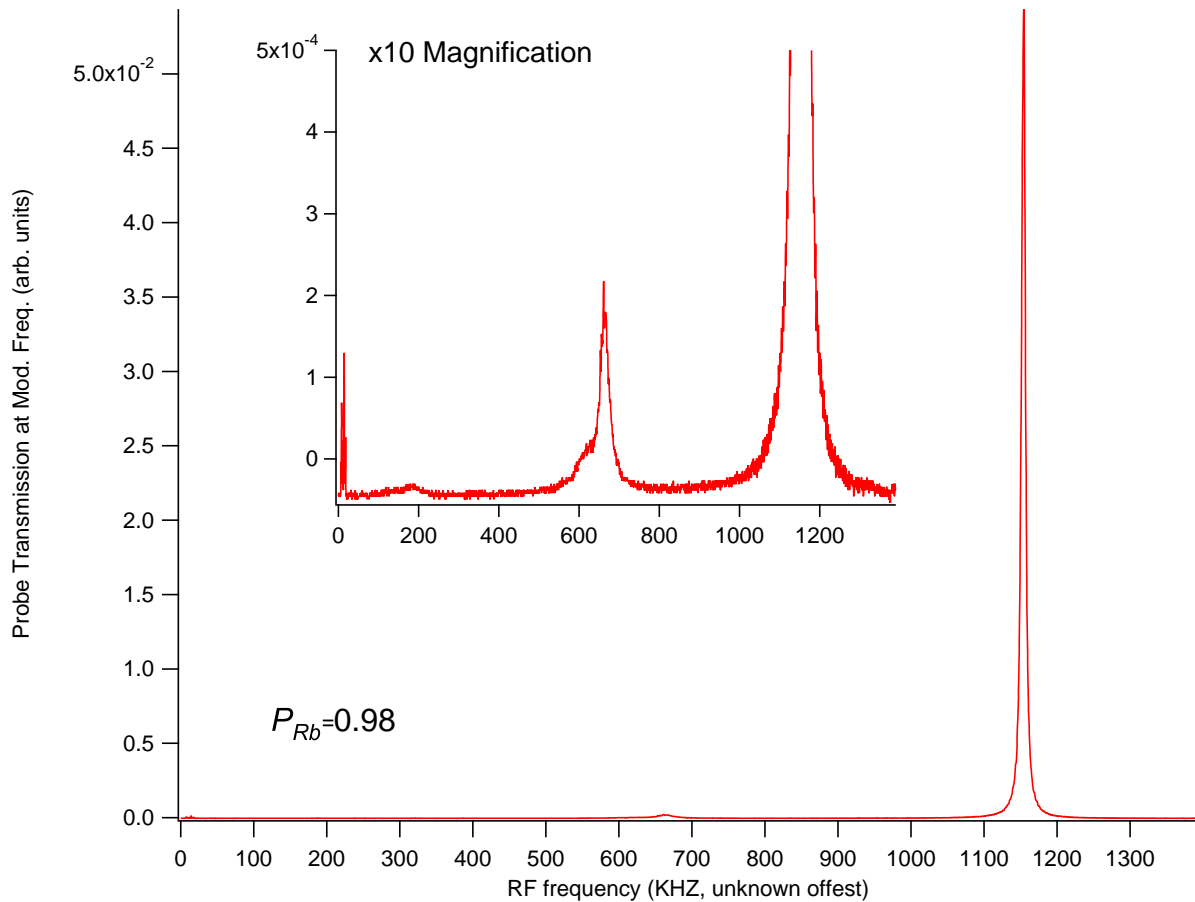


Figure 2.6 EPR spectrum for high  $P_{Rb} \approx 0.98$ . Very high signal to noise is needed to resolve the third peak set. The spike at the left end of the data is due a rapid ramping of the magnetic field at the beginning of the sweep.

Note that measurement of high  $P$  requires very high signal to noise. Fig. 2.6 shows a spectrum for  $P_{Rb} \approx 0.98$ . It can be seen that all the peaks except the first are very small. Since for the experiment described in Chapter 3 it is  $(1 - P_{Rb})$  that is the important quantity, very high signal to noise is needed for low uncertainty.

While under the conditions of high temperature and  $[Rb]$  where SEOP is typically performed, the Rb atoms are in spin temperature equilibrium, some of the experiments described below were performed at low temperature, where the atoms were found to be in an equilibrium that was quite different from spin temperature. When the atoms are not in spin temperature equilibrium, it is

important to record as many peaks of the EPR spectrum as can be detected above noise, and use all this information to extract the sub-level populations  $\rho_m$ .

Given the areas of the  $N$  detectable peaks,  $N-1$  independent ratios of peak areas may be formed, each of which can be related to the sublevel populations by Eq. 2.29. From these ratios,  $N$  sublevel populations can be calculated, assuming that the populations add up to 1 and that all other sub-level populations are zero. (The solutions for  $^{85}\text{Rb}$  populations given 3,5,7,9 and, 11 peaks and  $^{87}\text{Rb}$  given 3,5, and 7 peaks are in appendix E.)  $P_{\text{Rb}}$  is determined from the sublevel populations, and then compared to the value obtained assuming two more peaks at the noise level to confirm that resolving more peaks would not significantly affect the measurement of  $P_{\text{Rb}}$ .

### 2.2.3 Faraday Rotation Density Measurement

It is often important to measure the Rubidium density [Rb]. Estimates can be made using the vapor pressure curves from [Lide, 2011], but these values have been shown to be reliable only to the 50 % level. To directly determine [Rb] we measure the rotation of the polarization of a longitudinal probe beam, as the alkali-metal polarization is changed from  $P_{\text{Rb}}$  to  $-P_{\text{Rb}}$ . The probe laser is tuned a few nm away from the  $^2\text{S}_{1/2}$  to  $^2\text{P}_{3/2}$  transition at 780nm, and the detuning is measured with a New Focus Inc. 7711 Fizeau wave meter. The beam is chopped at  $\sim 400$  Hz, linearly polarized with a Glan-Taylor, and sent through the cell to the polarization rotation detector.

The detector is comprised of a  $\lambda/2$  plate mounted in a precision rotation stage, followed by a polarizing beam splitter cube which sends the horizontally and vertically polarized components of the beam onto a pair of photodiodes wired to produce a current proportional to the difference in intensity on the two detectors. The signal from the subtracting photodiode pair is sent to a lock-in amplifier referenced to the chopping frequency.

Due to the D1 and D2 resonances, there is a rotation of the polarization of the probe beam as it propagates through a spin polarized alkali-metal vapor. The linearly polarized light can be written as the combination of an equal amount of left-handed and right-handed circular polarizations, where the phase between the two components determines the orientation of the linear polarization.

The circular dichroism of a polarized vapor causes there to be a different path length for components of different helicity, changing the phase between them, which is a rotation of the polarization orientation. The angle is given by [Kadlecek et al., 2001, Vliegen et al., 2001, ?].

$$\theta_P = \frac{[\text{Rb}]le^2}{6mc} \left( \frac{1}{\Delta_{3/2}} - \frac{1}{\Delta_{1/2}} \right) P_{\text{Rb}} \quad (2.33)$$

where  $l$  is the length of the cell where the probe beam is passing through it,  $e$  is the electron charge,  $m$  the electron mass and  $c$  the speed of light. There is also a differential absorption of the two circular components, but the above equation is still correct at detunings where substantial absorption occurs, where it now describes the rotation of the major axis of the polarization ellipse.

To begin the measurement, the alkali-metal atoms are spin-polarized and the detector  $\lambda/2$  is set to orient the probe polarization at  $45^\circ$  onto the beam splitter cube, producing zero signal. Then the alkali-metal polarization is reversed by rotating the pump  $\lambda/4$ . The polarization rotation can be very large at high [Rb], so the angle is measured by slowly rotating the pump  $\lambda/4$  to change the alkali-metal polarization, while simultaneously rotating the detector  $\lambda/2$  to maintain zero signal. The total rotation angle is  $2\theta_P$ .

#### 2.2.4 [He] and [A] by Transmission

Transmission measurements can also be used to deduce buffer gas and rubidium vapor densities. The probe laser is chopped at  $\sim 400$  Hz and scanned across the D1 or D2 resonance. The transmitted intensity is measured with a silicon photo-diode and sent to a lock-in amplifier referenced to the chopping frequency. The lock-in output is proportional to the transmission  $I = I_0 e^{-N[\text{Rb}]l\sigma(\nu)}$ . The transmission of a far-off resonance probe can be used to find the lock-in signal due to  $I_0$ . Then dividing near resonance data by this value, taking the natural log, and dividing by  $l$ , gives the product  $[\text{Rb}]\sigma(\nu)$ . This product can be fit to the known lineshape ([Romalis et al., 1997]) to extract [He] and [Rb].

Romalis *et al.* deduced the broadening and shift coefficients of the Rb D1 and D2 lines due to collisions with  $^3\text{He}$ ,  $^4\text{He}$ ,  $\text{N}_2$ , and Xe buffer gasses. They measured the absorption cross-sections under various conditions and fit them to a lineshape profile derived from the Szudy and

	$^3\text{He}$	$\text{N}_2$
D1 full width (GHz/amg)	$18.7 \pm 0.3$	$17.8 \pm 0.3$
D1 line shift (GHz/amg)	$5.64 \pm 0.15$	$-8.25 \pm 0.15$
D1 asymmetry, $T_d$ ( $10^{-13}\text{s}$ )	$-1.9 \pm 0.1$	$16 \pm 2$
D2 full width (GHz/amg)	$20.8 \pm 0.2$	$18.1 \pm 0.3$
D2 line shift (GHz/amg)	$0.68 \pm 0.05$	$-5.9 \pm 0.1$
D2 asymmetry, $T_d$ (10-13s)	$-0.73 \pm 0.1$	$12 \pm 1$

Table 2.2 A table of the D1 and D2 broadening and lineshift coefficients for Rb in the presence of  $^3\text{He}$  and  $\text{N}_2$  buffer gases, as measured by [Romalis et al., 1997]

Bayliss universal Franck-Condon profiles ([Szudy and Baylis, 1975]), assuming low perturber density ([Szudy and Baylis, 1996]). The lineshape is proportional to  $\frac{\Gamma(\Delta')}{\Delta'^2 + \gamma^2/4}$ , where  $\Delta' = \omega - \omega_0 - \delta\omega$  is the detuning from the pressure shifted line center. At line center,  $\Gamma(0) = \gamma$ , in agreement with the Lorentzian profile expected from the impact approximation (citation?). The detuning dependence of  $\Gamma$  accounts for deviations from the Lorentzian shape. Walkup, Stewart, and Pritchard ([Walkup et al., 1984]) solved for  $\Gamma(\Delta')$  assuming a van der Waals potential, giving

$$\Gamma(\Delta') = nv_{th}8\pi R_{th}^2 I(\Delta'T_d) \quad (2.34)$$

where  $T_d$  is the duration of the collision,  $R_{th}$  is the effective radius of the collision, and  $v_{th}$  is the most probable thermal velocity in the center-of-mass frame.  $I(\Delta'T_d)$  contains the shape information, and is shown in Fig. 2.7. This lineshape is a Lorentzian profile with a small dispersion type correction. The asymptotic forms of  $I(\Delta'T_d)$  for  $z|\Delta'T_d| \geq 2.4$ , and a polynomial fit for the region in between are given in Table 2.3. Despite the fact that Rb- $^3\text{He}$  collisions are not dominated by van der Waals interactions, Romalis *et al.* found that Rb- $^3\text{He}$  and Rb- $\text{N}_2$  cross-sections fit well to the van der Waals lineshape. They observed the linewidths and shifts to be linear in buffer gas density, with coefficients listed in Table 2.2.

The values from Table 2.2 can be used, along with  $I(\Delta'T_d)$  (2.7), to determine the shape of the cross-section used to fit transmission spectra. To find the amplitude of the cross section, we

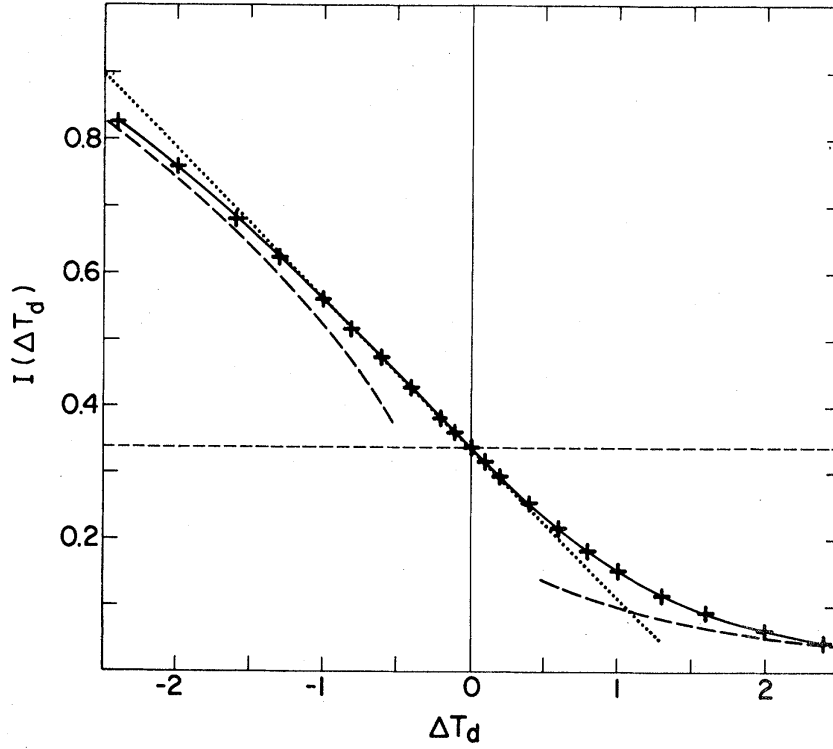


Figure 2.7 From [Walkup et al., 1984], numerically calculated points (+), the dotted line is a linear Taylor-series approximation for small  $|T_d|$ , and the dashed lines are asymptotic approximations for  $|T_d| \gg 1$ .

$\Delta'T_d$	$^3\text{He D1 } \Delta'$ (GHz)	$\text{N}_2 \text{ D1 } \Delta'$ (GHz)	$I(x)$
$\leq -2.4$	2010	-239	$\frac{\pi}{6}\sqrt{x}$
$-2.4 < \Delta'T_d < 2.4$	$-2010 < \Delta' < 2010$	$-239 < \Delta' < 239$	$.338 - .209x + .0187x^2 + .0083x^3 - .0003x^4$
$\geq 2.4$	-2010	239	$0.8464\sqrt{x}e^{-2.1341x^{5/9}}$

Table 2.3 Asymptotic forms of  $I(\Delta'T_d)$ , along with a polynomial fit near  $\Delta'T_d = 0$  [Walkup et al., 1984].

find the amplitude for a Lorentzian cross-section

$$\sigma(\nu) = A' \frac{\gamma}{\Delta^2 + \gamma^2/4} \quad (2.35)$$

The total cross section obeys

$$\int_{-\infty}^{\infty} \sigma(\nu) d\nu = \pi r_e f c = 2\pi A' \quad (2.36)$$

giving  $A' = f \times 4.21 \times 10^{-12} \frac{\text{cm}^2}{\text{GHz}}$ , where  $f=.342$  for the D1 line, and  $.696$  for the D2 line. Then in reference to the van der Waals lineshape, we write

$$\sigma(\nu) = A \frac{I(2\pi\Delta'T_d)}{(2\pi\Delta')^2 + \gamma^2/4} \quad (2.37)$$

From the expectation that the near resonance shape be Lorentzian, we set

$$AI(0) = A'\gamma \quad (2.38)$$

so

$$A = \frac{A'}{0.338}\gamma \quad (2.39)$$

and

$$\sigma(\nu) = A' \gamma \frac{I(2\pi\Delta'T_d)/0.338}{(2\pi\Delta')^2 + \gamma^2/4} \quad (2.40)$$

From transmission spectra taken at low density, where the core of the lineshape is observable, it is possible to extract the linewidth  $\gamma$  without knowing [Rb] precisely. [He] can then be deduced using the broadening coefficient, making a small correction for the contribution from [N<sub>2</sub>], measured at cell filling. Once the linewidth is known, fits of the transmission at any [Rb] have only [Rb] as a free parameter.

### 2.3 Longitudinal vs. Transverse EPR

Previously, this lab has measured  $P_{\text{Rb}}$  using longitudinal EPR spectroscopy, a variation of the transverse EPR spectroscopy described above. With this technique, as in transverse EPR, an x-directed RF field is applied to the atoms, and the magnetic holding field is swept to put

successive ground-state sub-level transitions on resonance with the driving field. However, instead of monitoring the coherence, the polarization of a linearly polarized, longitudinally directed probe beam is detected as a measurement of  $S_z$ .

given that  $F_z = \sum_F \sum_m m \rho_{Fm}$ , the change in  $F_z$  due to driving an RF resonance is

$$\frac{dF_z}{dt} = m \frac{d\rho_{Fm}}{dt} + (m-1) \frac{d\rho_{Fm-1}}{dt} \quad (2.41)$$

We can solve for the time evolution of the density matrix

$$\frac{d\rho_{Fm}}{dt} = -i([H, \rho]_m = -i\epsilon e^{-i\omega t} \rho_{m-1,m} - \epsilon^* e^{i\omega t} \rho_{m,m-1}) \quad (2.42)$$

using Eq. 2.12

$$\frac{d\rho_{Fm}}{dt} = -\left(\frac{g_s \mu_B B_x}{2(2I+1)}\right)^2 (F(F+1) - m(m-1)) (\rho_{Fm} - \rho_{Fm-1}) \frac{\gamma_{Fm}}{\delta_{Fm}^2 + \gamma_{Fm}^2/4} \quad (2.43)$$

and  $\frac{d\rho_{Fm-1}}{dt} = -\frac{d\rho_{Fm}}{dt}$ . So, for driving a single transition

$$\frac{dF_z}{dt} = -\left(\frac{g_s \mu_B B_x}{2(2I+1)}\right)^2 (F(F+1) - m(m-1)) (\rho_{Fm} - \rho_{Fm-1}) \frac{\gamma_{Fm}}{\delta_{Fm}^2 + \gamma_{Fm}^2/4} \quad (2.44)$$

We can add optical pumping and ground state spin relaxation to the RF pumping term to get

$$\begin{aligned} \frac{dF_z}{dt} &= \frac{1}{2} R_P (1 - P_{Rb}) - \left(\frac{g_s \mu_B B_x}{2(2I+1)}\right)^2 (F(F+1) - m(m-1)) (\rho_m - \rho_{m-1}) \frac{\gamma}{\delta^2 + \gamma^2/4} \\ &\quad - \frac{1}{2} \Gamma_{Rb} P_{Rb} \end{aligned} \quad (2.45)$$

In spin temperature,  $P_{Rb}$ ,  $\rho_m$ , and  $\rho_{m-1}$  can be written in terms of  $\beta$ , but there is no analytical solution to the differential equation in steady state. Given that the RF pumping term is small, the steady state solution can be approximated

$$P_{Rb} \approx \frac{R_P - \left(\frac{g_s \mu_B B_x}{2(2I+1)}\right)^2 (F(F+1) - m(m-1)) (\rho_m - \rho_{m-1}) \frac{\gamma}{\delta^2 + \gamma^2/4}}{R_P + \Gamma_{Rb}} \quad (2.46)$$

Thus, scanning across each resonance produces a  $\Delta P_{Rb}$  which has a Lorentzian lineshape. The spectrum produced should, as in transverse EPR spectroscopy, have peak areas that are insensitive to the linewidths  $\gamma_{Fm}$ . And, it should be possible to use the areas of successive peaks to deduce the sublevel populations in the same way as in transverse EPR.

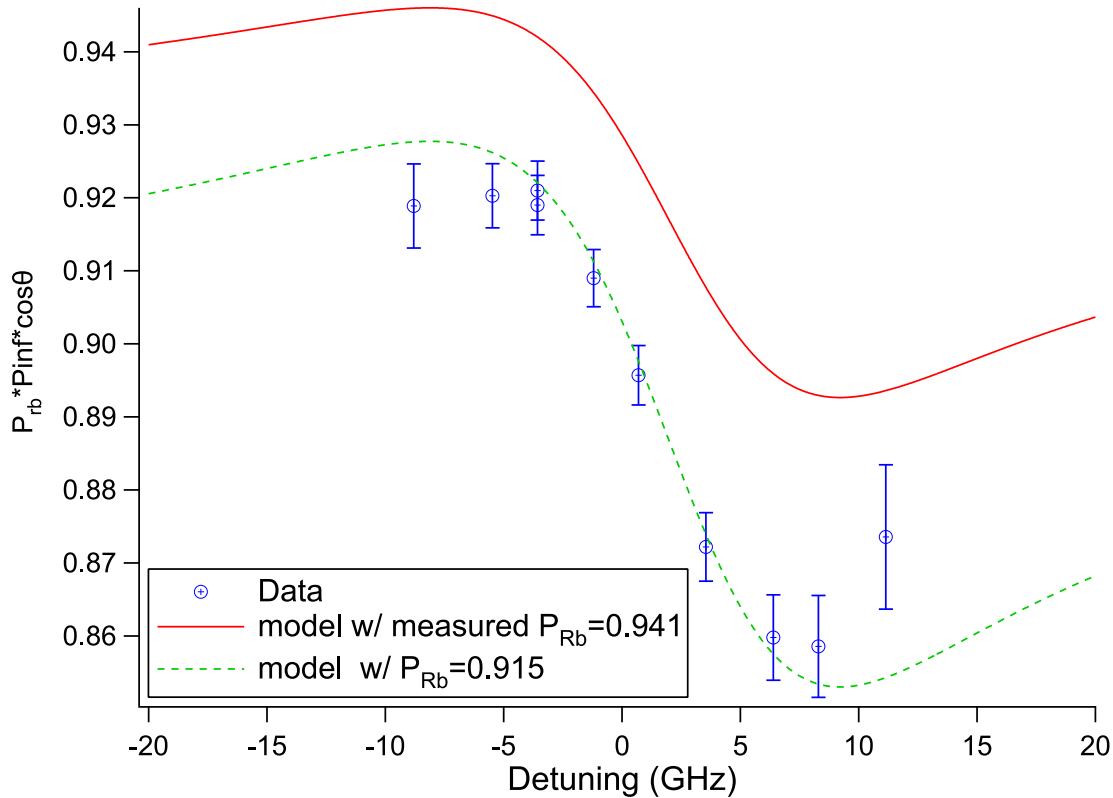


Figure 2.8 Measurement of the product  $P_{Rb}P_{\infty} \cos \theta$  on resonance (where  $P_{\infty}$  must be very nearly one), along with modeling of the data using  $P_{Rb}$  measured with longitudinal EPR spectroscopy (solid red line). The data fit well when a significantly lower  $P_{Rb}$  is put into the model(dashed green line).

When we began measurements of the circular dichroism of RbHe molecules, we were using longitudinal EPR spectroscopy. We began to suspect that the values of  $P_{Rb}$  deduced using longitudinal EPR spectroscopy were incorrect. In the region very near resonance,  $P_{\infty}$  is known to be very close to one. Extracting  $P_{\infty}$  from the data in this region is complicated, due to the hyperfine splitting of the ground state. But, models of the transmission that assumed  $P_{\infty} = 1$  and used values of  $P_{Rb}$  deduced from longitudinal EPR spectroscopy were inconsistent with the data (Fig. 2.8). The data could be modeled accurately if lower values of  $P_{Rb}$  were used.

We then measured  $P_{Rb}$ , under the same conditions, using both transverse and longitudinal EPR spectroscopy (Fig. 2.9). The spin polarization of the Rb vapor was varied by changing the circular

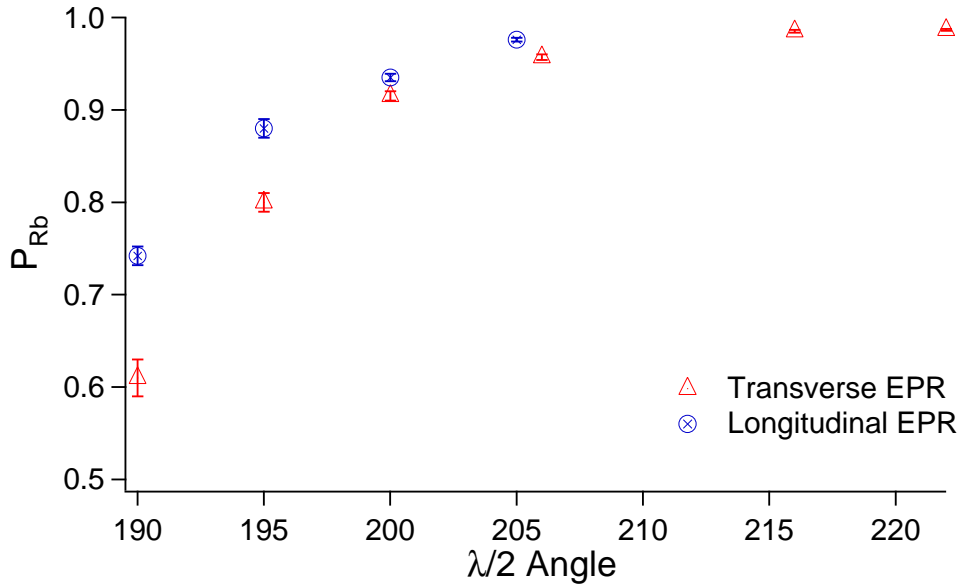


Figure 2.9  $P_{Rb}$  deduced from transverse and longitudinal EPR spectroscopy

polarization of the pump beam. The values of  $P_{Rb}$  deduced from longitudinal EPR were found to be systematically higher than those deduced from transverse EPR.

Furthermore, both methods of EPR spectroscopy were compared to  $P_{Rb}$  deduced from measuring the Faraday rotation of probe beam as the spin polarization is varied. As shown above (Eq. 2.33), the polarization of the probe beam undergoes a rotation while propagating through a polarized vapor, where the rotation angle  $\theta_P$  is proportional to  $P_{Rb}$ . First, the pump laser polarization was made circular, to maximize the spin polarization of then vapor. The helicity of the pump polarization was then reversed by rotating the  $\lambda/4$  plate by  $90^\circ$  and the rotation of the probe beam measured; this total rotation  $\theta_{tot}$  is proportional to  $2P_{Rb}$ . Subsequently, changes are made to the pump polarization, the Faraday rotation of the probe beam is measured, and the ratio of that small rotation to  $\theta_{tot}$  gives the fractional change in  $P_{Rb}$ . In Fig. 2.10 transverse EPR data and Faraday rotation data are shown to agree, when the rotation data is calibrated to the transverse EPR at very high  $P_{Rb}$ .

We do not currently understand why the two methods of EPR spectroscopy produce such different results.

## 2.4 $^3\text{He}$ Diagnostics

The diagnostics for measuring properties of the  $^3\text{He}$  spin are not used in any of the experiments described in the remainder of the thesis, and are discussed in appendix A

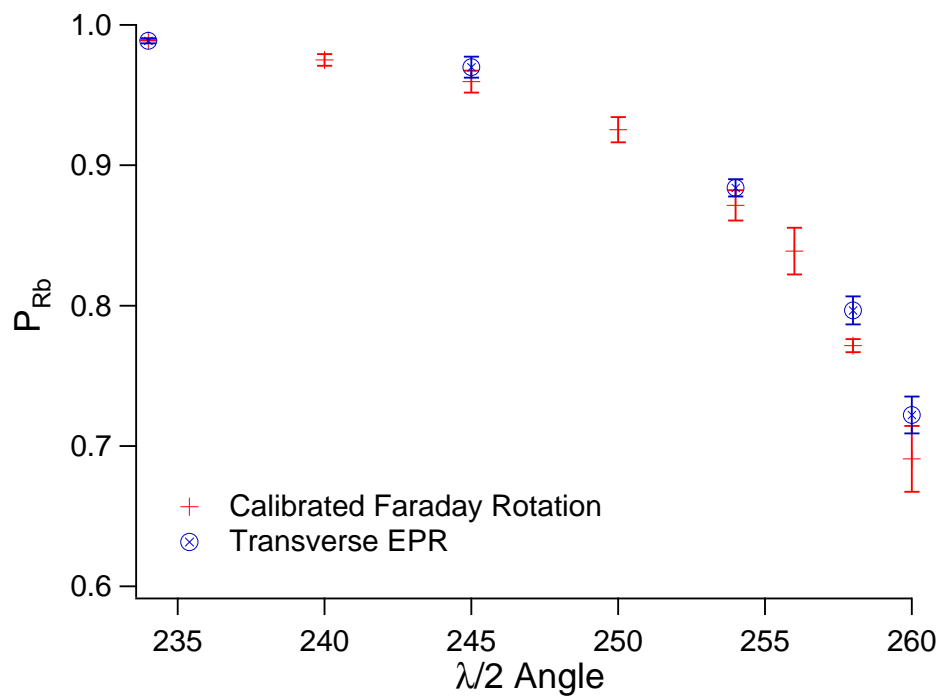


Figure 2.10  $P_{\text{Rb}}$  deduced from transverse EPR spectroscopy, and Faraday rotation calibrated to EPR spectroscopy at high  $P_{\text{Rb}}$

## Chapter 3

### Dark State Absorption

#### 3.1 Motivation

Experimenters in our lab and others consistently observe that SEOP requires more laser power than simple models such as the one presented in Chapter 1 predict. In [Chen et al., 2007], alkali-metal polarizations were measured as a function of alkali-metal density in a large group of SEOP and HySEOP cells. In, almost all cases, the measured polarizations are significantly lower than models predict. Also, Babcock et al. did a series of experiments on the SEOP performance of pure Rb and K-Rb hybrid cells with density ratios up to 500. The cells had 8 amagats of  $^3\text{He}$ , and were pumped with a 60W un narrowed diode array bar [Babcock et al., 2003]. They measured the alkali polarization in each cell as a function of pump laser intensity, and extrapolated to infinite pump power to find  $P_{max}$ , the maximum achievable alkali polarization.  $P_{max}$  in the pure Rb SEOP cell was  $\sim .91$ . If the relaxation mechanisms limiting the polarization of the alkali-metal atoms were independent of the pump laser intensity, then increasing the pump intensity to sufficiently high levels should allow the optical pumping to overwhelm the relaxation mechanisms. The fact that  $P_{max}$  was significantly less than one implies that a pump light induced relaxation method was significantly limiting the alkali-metal polarization.

One possible mechanism for pump light induced relaxation is dark state absorption due to a breakdown of the angular momentum selection rule of the  $^2S_{1/2} \rightarrow ^2P_{1/2}$ (D1) optical pumping transition. As described in chapter 1, for free atom angular momentum selection rules of the D1 transition mandate that atoms in the  $m_J = +1/2$  ground state sublevel do not absorb pumping light with spin  $\lambda=1$ . The optical pumping excites atoms out of the  $m_J = -1/2$  ground-state, roughly

50% of which decay into the  $m_J = +1/2$  state. Atoms are trapped in the dark state, until they relax to the  $m_J = -1/2$  through ground state spin relaxation collisions. As long as the pumping rate is very large compared to the ground state relaxation rate (which is typically easy to achieve),  $P_{\text{Rb}}$  should be near unity. If atoms in the  $m_J = +1/2$  state do absorb  $\lambda=1$  pump light at a small rate, this would be a light induced relaxation method that would limit  $P_{\text{Rb}}$  even for high pumping rates.  $P_{\text{Rb}}$  would come to an equilibrium, less than unity, depending on the relative rate of pump laser excitation out of the two ground-states.

The remainder of this chapter describes an experiment measuring the dark state absorption due to Rb- $^3\text{He}$  and Rb- $\text{N}_2$  collisions. The main results were reported briefly in [Lancor et al., 2010a], and in more detail in [Lancor et al., 2010b].

### 3.2 Parameterization- $P_\infty$

The absorption cross section for monochromatic light of spin  $\lambda$ , by atoms in the  $m_J = \pm 1/2$  states can be written, generally, as [Chen et al., 2007]

$$\sigma_{\pm}^{\lambda}(\nu) = \sigma_0(\nu)(1 \mp \lambda P_\infty(\nu)) \quad (3.1)$$

where  $\sigma_0(\nu)$ , the cross-section for absorption by unpolarized atoms, contains the information about the lineshape and strength of the transition, and  $P_\infty(\nu)$ , limited to  $-1 \leq P_\infty \leq 1$ , contains the angular momentum information. Or, the cross section for absorption by the atomic ensemble can be written in terms of the spin polarization  $P_{\text{Rb}} = \rho_{1/2} - \rho_{-1/2}$

$$\sigma_{P_{\text{Rb}}}^{\lambda}(\nu) = \sigma_0(1 - \lambda P_\infty(\nu) P_{\text{Rb}}) \quad (3.2)$$

For the D1 atomic transition, angular momentum selection rules give  $P_\infty=1$ . As  $P_{\text{Rb}}$  goes from -1 to 1, the absorption cross section for  $\lambda=1$  light goes from  $2\sigma_0$  to zero; Atoms in the  $m_j = +1/2$  do not absorb any  $\lambda=1$  light. A true dark state is present only if  $P_\infty=1$ , any deviation from  $P_\infty=1$  within the bandwidth of the pumping laser will lead to absorption out of the spin-up groundstate. We generalize Eq. 1.3[Walker and Happer, 1997] for the evolution of the atomic spins

due to pumping with monochromatic  $\lambda=1$  light

$$\frac{dF_z}{dt} = -\frac{1}{2}R_p(\nu)(1 - P_\infty(\nu))\rho_{1/2} + \frac{1}{2}R_p(\nu)(1 + P_\infty(\nu))\rho_{-1/2} - \Gamma_{Rb}\frac{P_{Rb}}{2} \quad (3.3)$$

$$= \frac{1}{2}R_p(\nu)(P_\infty(\nu) - P_{Rb}) - \Gamma_{Rb}\frac{P_{Rb}}{2} \quad (3.4)$$

where  $R_p(\nu)$  is the scattering rate for unpolarized light and  $\Gamma_{Rb}$  is the ground state collisional spin destruction rate. Solving this in steady state gives

$$P_{Rb} = P_\infty(\nu)\frac{R_p(\nu)}{R_p(\nu) + \Gamma_{Rb}} \quad (3.5)$$

Thus,  $P_\infty$  is the alkali-polarization at infinite pumping rate.  $P_\infty$  can also be described as the normalized circular dichroism of fully polarized atoms, where we define the normalized circular dichroism

$$C = \frac{\sigma_{P_{Rb}}^{-1} - \sigma_{P_{Rb}}^1}{\sigma_{P_{Rb}}^{-1} + \sigma_{P_{Rb}}^1} = P_\infty P_{Rb} \quad (3.6)$$

and

$$P_\infty = \frac{\sigma_1^{-1} - \sigma_1^1}{\sigma_1^{-1} + \sigma_1^1} \quad (3.7)$$

Thus, the normalized circular dichroism is the product of the atomic polarization, which depends on the experimental conditions, and  $P_\infty$ , which depends only on the atomic properties.

### 3.3 Rb-He Molecular Potentials

It is reasonable to expect that there may be some absorption from the  $m_j = +1/2$  ground state due to the presence of the  $^2S_{1/2} \rightarrow ^2P_{3/2}$ (D2) resonance. For the D2 transition,  $P_\infty = -1/2$ . Angular momentum conservation allows excitation from the  $m_J = +1/2$  state by  $\lambda=1$  light, since there is an  $m_J = +3/2$  excited state. Since these experiments are typically done with gas pressures of several atmospheres, it is natural to ask to what extent pressure broadening gives a small amount of D2 character to the D1 resonance. Several previous studies suggest this. First, spectroscopic measurements show that the red wing of the D2 line certainly overlaps the D1 resonance [Drummond, 1974]. In addition, He collisions can transfer  $5^2P_{1/2}$  population to  $5^2P_{3/2}$ , albeit with a small cross section [Rotondaro and Perram, 1998]. The existence of this excited-state

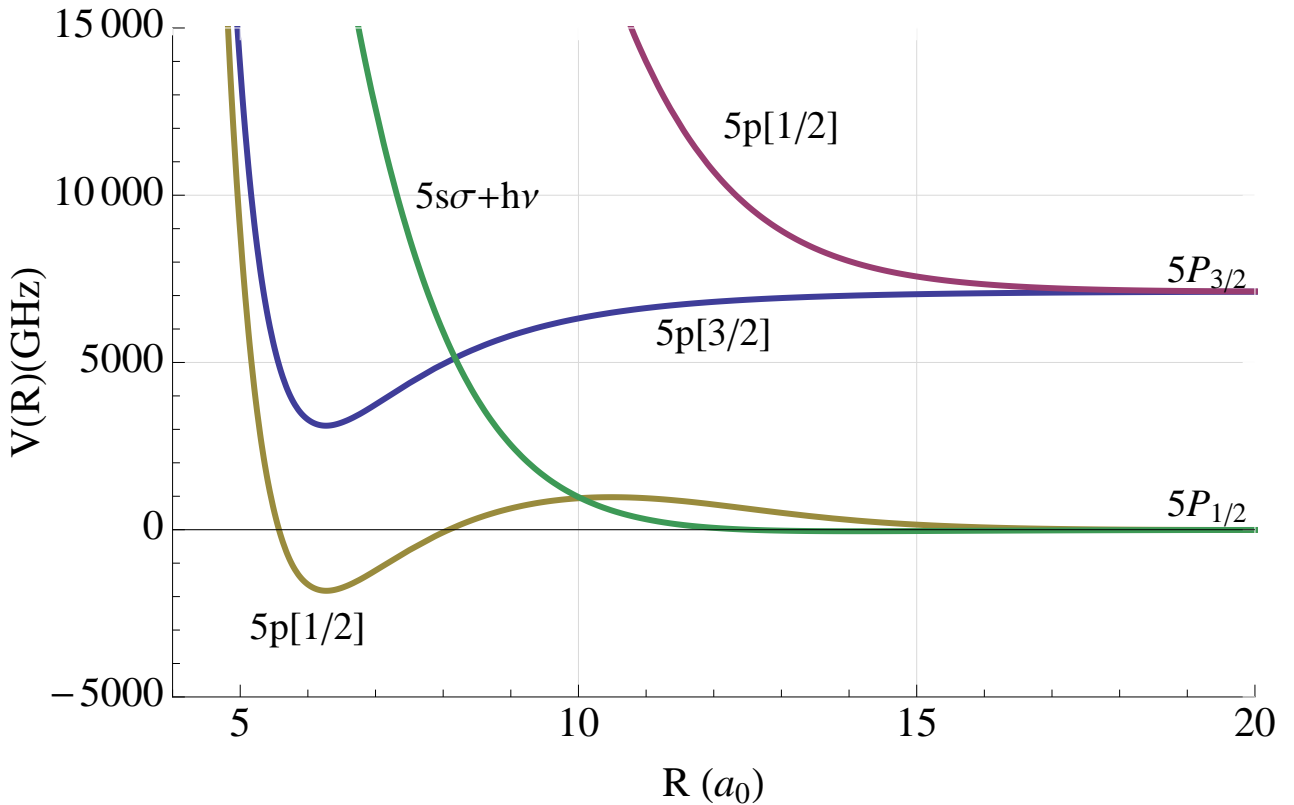


Figure 3.1 Adiabatic energy curves for RbHe molecules adapted from [Pascale, 1983] with the method of [Allard and Kielkopf, 1982]. The projection of the total electronic angular momentum along the interatomic axes is given in brackets. The curve crossings between the photon-dressed  $5s\sigma$  state and the two excited-state curves mean that photon absorption is allowed during a collision. As explained in the text, these absorption processes are not subject to the free-atom dipole selection rules, allowing normally angular-momentum-forbidden transitions to occur

spin-relaxation process implies that during collisions with He atoms the  $5^2P_{1/2}$  and  $5^2P_{3/2}$  states are somewhat mixed. Finally, from a theoretical perspective it is well known that during collisions the fine-structure interaction is partially decoupled by the intramolecular fields, thereby mixing  $P_{1/2}$  and  $P_{3/2}$  molecular states [Allard and Kielkopf, 1982]

The partially D2-like absorption of light during RbHe collisions can be understood by considering the lowest adiabatic potential energy curves for Rb-He molecules, shown in Fig. 3.1. It is well known [Allard and Kielkopf, 1982] that RbHe collisions are non-adiabatic, but for a qualitative understanding the adiabatic curves should be useful. The curves that correlate with the two  $5P$  fine structure levels are designated  $5p[\Omega]$ , where  $\Omega = 1/2, 3/2$  is the magnitude of the projection

of the electron angular momentum on the interatomic axis. The  $\Omega = 3/2$  state has pure  $P_{3/2}$  character while the  $\Omega = 1/2$  states contain significant mixtures of the two fine-structure components for interatomic separations  $r < 15a_o$ . Also shown in Fig. 3.1 is the ground state potential  $5s\sigma$  shifted up by the energy of a D1 photon. The crossing between the  $5p[3/2]$  state and the repulsive wall of the photon-shifted  $5s\sigma$  state at  $r = 8a_o$  means that resonant D2-like absorption can occur during RbHe collisions. Since  $kT/h = 9400\text{GHz}$  at typical  $180^\circ\text{C}$  temperatures for SEOP, the curve crossing energy of  $h \times 5000\text{GHz}$  is readily thermally accessed. It is also seen in Fig. 3.1 that the fine-structure-mixed  $5p[1/2]$  molecular potential is resonantly accessed by D1 light.

It should be noted that the D2-like absorption during collisions should be non-resonant, as light detuned from the D1 atomic resonance will be resonant with the  $5s\sigma \rightarrow 5p[3/2]$  transition at thermally accessible inter-atomic distances. This suggests that the effect of molecular absorption would be accentuated for broadband pumping sources, as was seen in [Babcock et al., 2003].

### 3.4 Estimates

In this section we will present estimates of the dichroism of RbHe molecules in the vicinity of the D1 resonance line. To our knowledge, the circular dichroism of these molecules has never been studied before, nor have calculations been published. A full calculation is beyond the scope of this work, but the considerations given here will attempt to explain our observations.

We consider the light absorption process as a collision, where the ground-state potential curve is shifted up by one photon energy. As seen from Fig. 3.1, 795 nm light can be resonantly absorbed to the  $5p[3/2]$  state during a collision. In the absence of fine-structure mixing by the atom-atom interactions, the  $5p[1/2]$  state that correlates at large  $r$  to the  $P_{1/2}$  state would not absorb the  $\lambda=1$  light. However, the fine-structure interaction causes the  $5p[1/2]$  states to be mixtures of  $P_{1/2}$  and  $P_{3/2}$  in the laboratory frame, with the  $P_{3/2}$  part giving rise to an allowed light absorption. In this case, the Rabi coupling will depend on the interatomic separation  $r$ , going to zero at large  $r$ .

To simplify the calculations, we will assume that we can neglect the variation in the light-atom coupling with collision angle, replacing the angle-dependent Rabi coupling with its angular average. We will also assume that we can neglect rotational coupling of the adiabatic curves

[Allard and Kielkopf, 1982]. With these assumptions, the light-absorption process is isotropic and we can consider the problem as a simple collision in the radial coordinate, with excitation to each of the excited-state potential curves considered separately.

Assuming a classical trajectory with distance of closest approach  $r_0$  (assumed to occur at time  $t = 0$ ), it is convenient to define

$$\alpha(r) = \int_{r_0}^r \frac{dr}{v(r)} \Delta V(r) \quad (3.8)$$

$$v(r) = v_\infty \sqrt{1 - \frac{b^2}{r^2} - \frac{2V_{5s\sigma}(r)}{mv_\infty^2}} \quad (3.9)$$

where  $K = mv_\infty^2/2$  is the initial kinetic energy, corresponding to initial speed  $v_\infty$ , and  $b$  is the impact parameter for the collision. The difference potential is  $\hbar\Delta(r) = V_e(r) - V_{5s\sigma}(r) - \hbar\omega$ . Then, in the weak intensity limit, first order perturbation theory gives the probability of finding the atom in the excited state  $e$  after a single collision is

$$|c_e|^2 = \left| \int_{r_0}^{\infty} \frac{dr}{v} \epsilon(r) \cos \alpha(r) \right|^2. \quad (3.10)$$

The molecular Rabi frequency is given in terms of the atomic Rabi frequency as

$$\epsilon(r) = \frac{\epsilon_0}{2} \sin(\beta(r)/2) \quad (3.11)$$

where the factor of 2 accounts for the angular average over collision orientations, and  $\beta$  is the  $P_{3/2}$  mixing angle to be discussed below. From this we get the excitation rate to a single adiabatic potential by averaging over the collision impact parameters:

$$\mathcal{R} = [\text{He}]v_\infty \int \pi db^2 |c_e|^2 = \sigma^1 I / \hbar\omega \quad (3.12)$$

The atomic Rabi frequency  $\epsilon_0$  is related to the light intensity and the atomic lifetime  $\tau$  by  $\epsilon_0^2 = 3\lambda^3 I / (2\pi\hbar c\tau)$ , giving finally

$$\sigma^1(v_\infty) = \frac{3\lambda^2 v_\infty}{2\pi\tau} [\text{He}] \int \pi db^2 \frac{|c_e|^2}{\epsilon_0^2}. \quad (3.13)$$

This expression is then averaged over a Maxwellian velocity distribution.

We begin by considering absorption to the  $5p[3/2]$  curve in Fig. 3.1. This state is of pure  $P_{3/2}$  character, so that  $\beta = \pi$ . D1 light is sufficiently far detuned that non-adiabatic effects should not be too important, and we consider the process as a Landau-Zener transition from the ground state  $5s\sigma+h\nu$  at the crossing point. The probability of excitation is

$$P_{LZ} = \frac{\pi\hbar\epsilon^2}{v_r|d\Delta/dr|}, \quad (3.14)$$

with all quantities evaluated at the crossing point. Performing the impact parameter integration, the thermal average, and accounting for the two-fold  $|\Omega|$  degeneracy then gives

$$\sigma_{\text{opt}} = [\text{He}] \frac{3\pi^{3/2}\lambda^2 r_c^2}{8\tau|d\Delta/dr|} e^{-V_{5s\sigma}/T}. \quad (3.15)$$

For 1 amg of He, this evaluates to  $1.8 \times 10^{-18} \text{ cm}^2$  at the D1 resonance, about a factor of 2 smaller than a direct numerical integration (performed by my advisor Thad Walker) of Eq. 3.10 that gives  $3.9 \times 10^{-18} \text{ cm}^2$ .

For the  $5p[1/2]$  curve that correlates to the  $P_{1/2}$  state at  $r = \infty$ , the Landau-Zener approximation is invalid because the phase  $\alpha$  does not vary rapidly enough with  $r$ . The  $r$ -dependent wavefunction, written in terms of the atomic fine-structure states  $|JM\rangle$ , is  $|5p[1/2]\rangle = \cos(\beta/2)|\frac{1}{2}\frac{1}{2}\rangle + \sin(\beta/2)|\frac{3}{2}\frac{1}{2}\rangle$ . Professor Walker also calculated the mixing angle  $\beta(r)$  as shown in Fig. 3.2. Numerical integration of Eqs. 3.10 and 3.13 gives  $5.5 \times 10^{-18} \text{ cm}^2$  at 1 amg.

### 3.5 Preliminary Result

As reported in Earl Babcock's thesis ([1]), preliminary measurements of  $P_\infty$  were made in the wings of the D1 line in two SEOP cells; One cell, Betty, as  $[^3\text{He}]=0.80 \text{ amg}$  and the other cell, NHRb, has  $[^3\text{He}]=3.27 \text{ amg}$ . In that experiment, a 30 W frequency narrowed (50 GHz linewidth) external cavity laser was used to optically pump the atoms at different frequencies  $\nu$ , and the resulting polarization  $P_{\text{Rb}}(\nu)$ , pumping rate  $R_p(\nu)$ , and ground state spin-relaxation rate  $\Gamma_{\text{Rb}}$  were measured. For off-resonant pumping, they assumed  $P_\infty$  was essentially constant over the small range of frequencies present in the pumping beam, so Eq. 3.5 becomes

$$P_\infty(\nu) = \left(1 + \frac{\Gamma_{\text{Rb}}}{R_p(\nu)}\right) P_{\text{Rb}}(\nu) \quad (3.16)$$

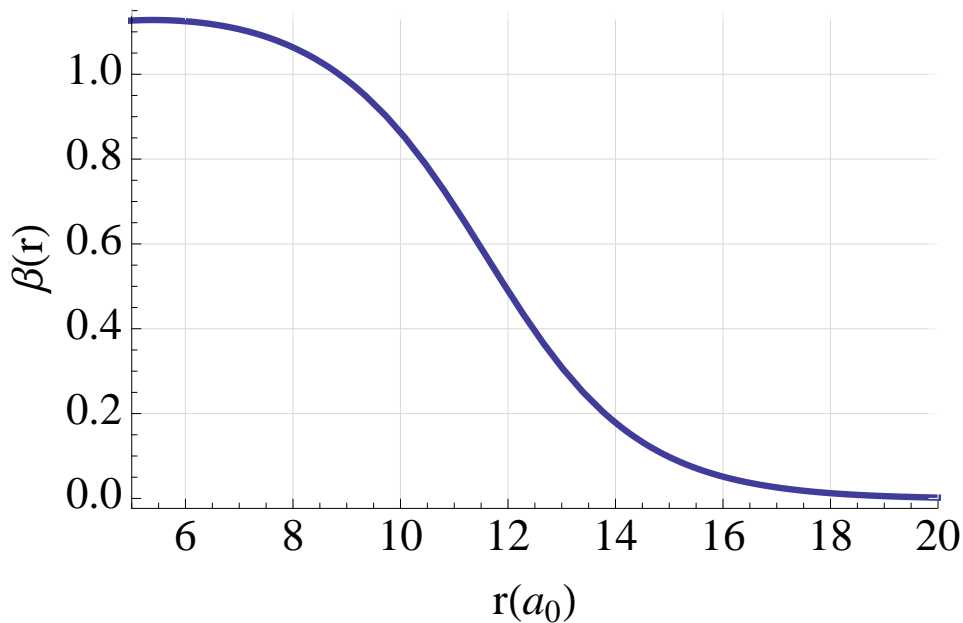


Figure 3.2 Fine-structure mixing angle for the 5p[1/2] states as a function of interatomic separation.

The results are shown in Fig. 3.3, along with a naive model that uses Lorentzian lineshapes for the D1 and D2 transitions. The data show that  $P_\infty$  drops off much faster than the model predicts in the wings of the D1 transition, but since the linewidth of the laser is large, the frequency resolution of this measurement is too poor to measure  $P_\infty$  precisely near resonance.

### 3.6 Overview

To measure  $P_\infty$  with good frequency resolution, we deduced  $P_\infty$  by comparing the absorption of spectrally narrow,  $\lambda = 1$  probe beam light by atoms with polarizations  $\pm P_{\text{Rb}}$  using the apparatus and methods described here. We measured the transmissions  $I_\pm = I_0 e^{-[\text{Rb}]l\sigma_{\pm P}^1(\theta)}$  at rubidium density [Rb], and the transmission with zero Rubidium density  $I_0$ . From this we can calculate the normalized circular dichroism  $C$ , where, as shown below, [Chann et al., 2002b] show that correcting Eq. 3.6 for the probe beam angle relative to the z-direction  $\theta_p$ , gives  $C = P_\infty P_{\text{Rb}} \cos \theta_p$ . We also measure  $P_{\text{Rb}}$ , and calculate  $P_\infty(\nu)$ .

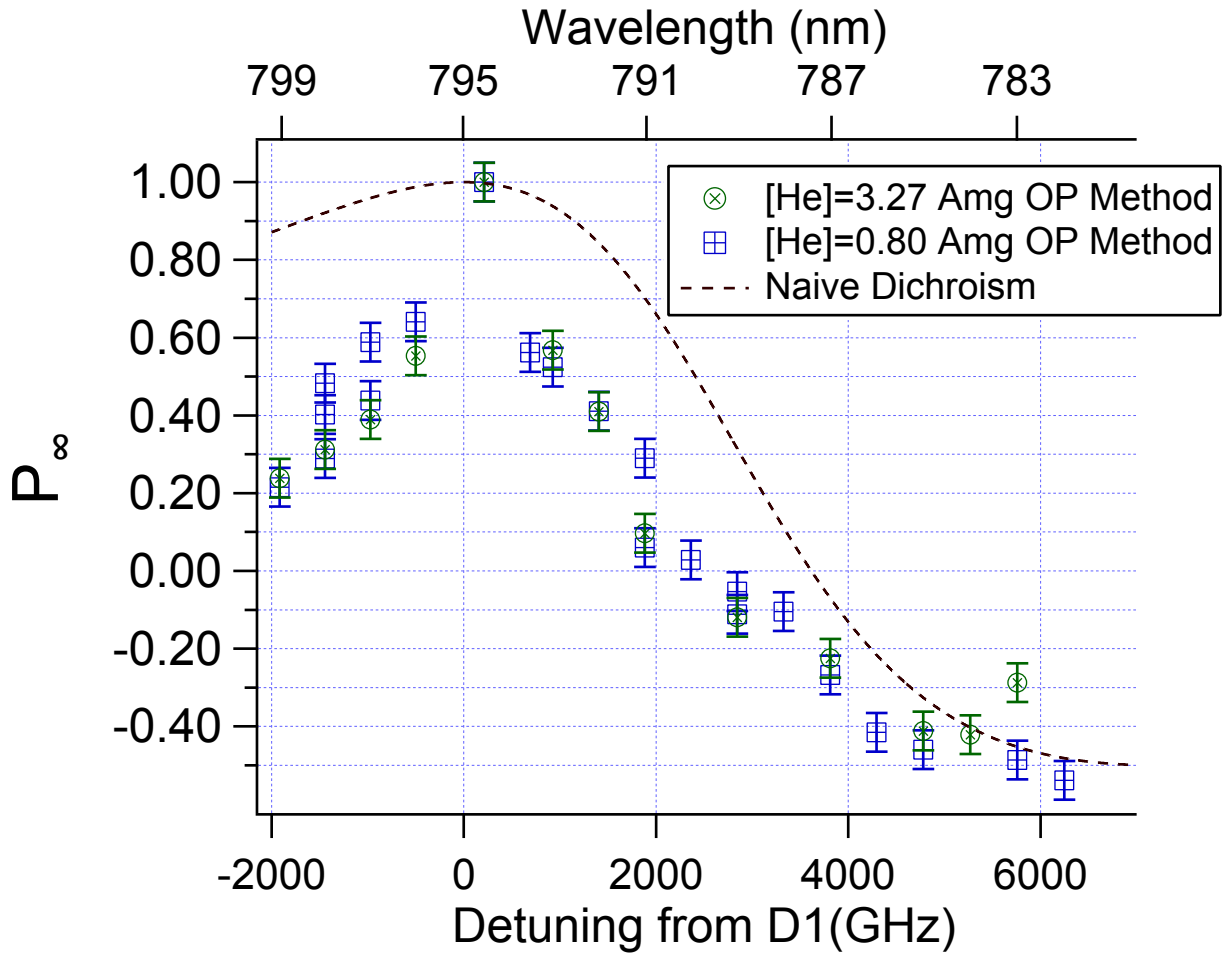


Figure 3.3  $P_\infty$  measured by tuning the pump laser to a range of frequencies and measuring the resulting polarization  $P_{Rb}(\nu)$ , pumping rate  $R_p(\nu)$ , and ground state spin-relaxation rate  $\Gamma_{Rb}$ . The dashed line is a naive model assuming Lorentzian lineshapes for the D1 and D2 resonances.

We measured  $P_\infty$  as a function of frequency in the same two SEOP cells as in Babcock's experiment, Betty and NHRb, and in one cell with no  $^3\text{He}$  and  $[\text{N}_2]=2.80$ . From this we deduced the dark state absorption near the D1 resonance due to RbHe and RbN<sub>2</sub> collisions

$$\frac{\sigma_1^1(\nu_1)}{[\text{N}_2]} = 1.49 \pm 0.15 \times 10^{-17} \frac{\text{cm}^2}{\text{amg}} \quad (3.17)$$

$$\frac{\sigma_1^1(\nu_1)}{[^3\text{He}]} = 1.10 \pm 0.12 \times 10^{-17} \frac{\text{cm}^2}{\text{amg}} \quad (3.18)$$

These cross-sections are large enough to greatly reduce the efficiency of optical pumping, particularly at high  $^3\text{He}$  and with broadband pumping sources.

### 3.7 Experimental Procedure

A schematic of the apparatus is shown in Fig. 3.4. A Rb vapor cell, contained in a flowing hot-air oven, was optically pumped by a circularly polarized frequency narrowed diode array bar providing 35 Watts of power at 795nm, with a spectral width of 125 GHz [20]. A holding field of  $\sim 50$  G was applied in the pump propagation direction. A probe beam was attenuated to  $P < 50 \mu\text{W}$ , sent through a chopper operating at 485 Hz, and linearly polarized with a polarizing beam splitter cube. Directly in front of the oven, the beam went through a non-polarizing beam splitter plate to provide a reference signal proportional to the incident intensity, and a quarter wave plate to produce circular polarization. The reference and transmitted intensities were measured on silicon photo-diodes and sent to lock-in amplifiers referenced to the chopper frequency. To change the direction of the atomic spin polarization relative to the probe helicity, the pump  $\lambda/4$  plate was rotated  $90^\circ$ , reversing the pump laser helicity.

To obtain the relationship between the incident and transmitted intensities in the absence of Rb (thus accounting for loss in the windows of the oven and cell), a measurement was taken at room temperature. If the probe beam propagated in a direction nearly perpendicular to the oven and cell walls, there were large etalon fringes in the transmission (as much as  $\sim 10\%$  fluctuations). When the probe beam was sent through the oven at an angle of  $\theta_p \sim 15^\circ$  to the perpendicular, the etalon effects were reduced to  $\sim 1\%$  in the cylindrical Betty and less in the spherical cells. Also, care was taken to select optical elements with the minimum frequency dependence to their transmission, but a small slope in the transmission versus frequency was observed. Thus, a series of measurements of the transmission was made across the range of frequencies of interest, and a linear fit was made. The standard deviation of the points from the linear fit was factored into the uncertainty calculation. When the cell was heated to put Rb into the vapor phase, the ratio of incident to transmitted intensities without atoms present ( $I_0$ ) was calculated at each probe frequency from the linear fit to the room temperature data.

For the pure  $\text{N}_2$  cell, Rb liquid droplets on the walls of the cell scattered a significant fraction of the probe light. This produced an uncontrolled temperature dependence to the probe transmission

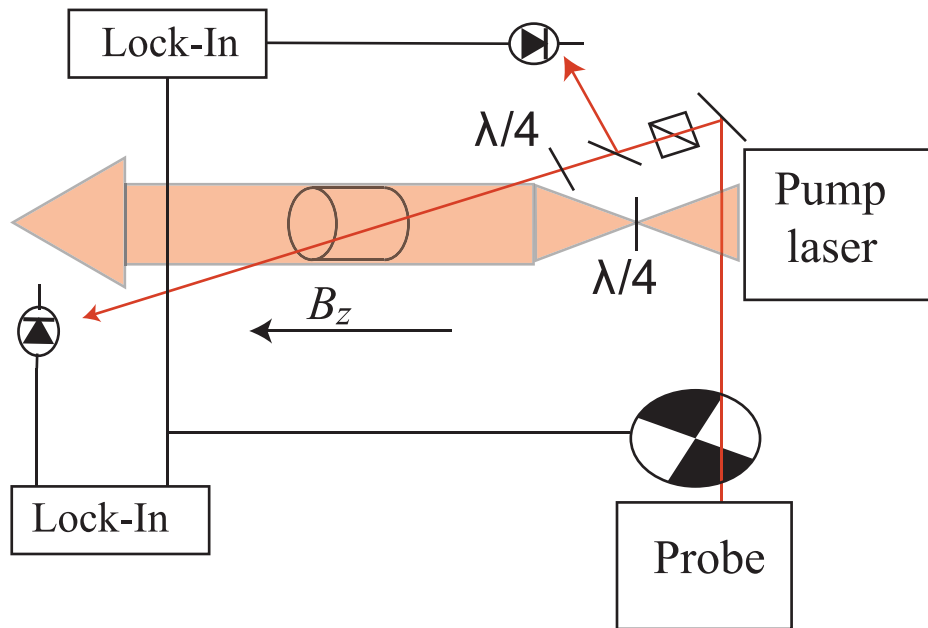


Figure 3.4 Apparatus for measuring the circular dichroism of Rb-He vapor. The pump laser, propagating parallel to a magnetic field, spin-polarizes Rb atoms by optical pumping. The polarization is set either parallel or antiparallel to the field, as determined by the orientation of a quarter-wave plate. The fractional transmission of a weak, circularly polarized, tunable probe laser is determined by the ratio of photodiode voltages before to those after traversal of the cell. The circular dichroism is then determined from the transmissions for both directions of Rb polarization.

as the droplets moved on the face of the cell. Typically, the transmission was stable in time at a given temperature, but changed by large amounts as the temperature was changed. To account for this, the probe laser and an additional 856 nm laser were coupled into a fiber, with the 856 nm laser transmission serving to measure small variations of the transmission of the cell walls with time and temperature (this beam is very far off-resonance, so atomic absorption is negligible). A measurement of the transmission of the 856 nm laser was made at room temperature, and after the cell was heated measurements were made periodically. The ratio of the hot and cold measurements was used to correct  $I_o$  derived from room temperature measurements of the 795nm transmission. It was noted that Rb liquid droplets tended to be least prevalent on the parts of the cell that the hot air from the oven flowed over, so we made a small vent that directed the flowing air across the front

and back of the cell, which greatly reduced amount of Rb liquid in the beam path. Under these conditions, the 856nm transmission changed only by a small amount with temperature.

Temperatures ranging from  $\sim 60^\circ \text{C}$  to  $180^\circ \text{C}$ , corresponding to  $[\text{Rb}] = 1 - 200 \times 10^{12} \text{ cm}^{-3}$ , were used to produce appropriate optical thickness for transmission measurements at a range of frequencies. At the lower temperatures, the pump laser power was reduced to lower background noise. At each temperature,  $P_{\text{Rb}}$  was measured using transverse EPR spectroscopy as described in Chapter 2. As only the transverse component of the probe beam is used, the modulated component of the Faraday rotation is proportional to  $P_x \cos \theta_p$  and is therefore much smaller than would be detected by a transverse probe. However, we wished to know the polarization averaged along the probe beam path, so a measurement with a separate transverse beam would not have been appropriate. The measured DC circular dichroism was degraded by a factor of  $\cos \theta_p$ , so an angle of  $\theta_p = 17.52 \pm 0.2$  was chosen as a trade off between the dichroism signal size, EPR signal quality, and reduced etalon fringing.

High quality EPR signals were crucial for deducing  $P_{\text{Rb}}$  at low density, where the atoms were not in spin-temperature and many EPR peaks needed to be resolved to accurately deduce  $P_{\text{Rb}}$ . At each temperature,  $P_{\text{Rb}}$  for  $^{85}\text{Rb}$  was measured for both pump helicities before and after each set of transmission measurements. At low temperatures, where the atoms were not in spin temperature, measurements of  $^{87}\text{Rb}$  were done as well. The two isotopes were always found to have the same  $P_{\text{Rb}}$ , within uncertainty.

### 3.8 Analysis

We wish to find the normalized circular dichroism  $C$ , from which we can deduce  $P_\infty$ . The basic quantities measured in the experiment are the transmissions  $I'_\pm$  for nearly circularly polarized light of  $\lambda \approx .997$ , propagating at angle  $\theta_p$  to the atomic polarization  $\pm P_{\text{Rb}}$ .

First, the transmission data was corrected for an observed residual transmission  $I_{res}$  of the probe beam even on resonance at very high optical depths ( $> 0.5\%$ ). This probably results from a small amount of light at the free-running probe laser wavelength. Data points with transmission  $\leq 2\%$  were not used due to the uncertainty in this correction. We assume that a fraction  $f_{res} =$

$I_{res}/I_0$  of the probe light is transmitted at all frequencies. So we write the transmissions

$$I'_{\pm}(\nu) = I_0((1 - f_{res})e^{-[Rb]l\sigma_{\pm P}^{\lambda}(\nu)(\theta_p)} + f_{res}) \quad (3.19)$$

and solve for

$$e^{-[Rb]l\sigma_{\pm P}^{\lambda}(\nu)(\theta_p)} = \left(\frac{I'_{\pm}(\nu)}{I_0} - f_{res}\right)/(1 - f_{res}) \quad (3.20)$$

Then, using the measured value of  $\lambda$ , we solve for the transmissions  $I_{\pm}$  for  $\lambda = 1$  light by atoms with  $P_{Rb} = \pm P$

$$I_{\pm}(\nu) = I_0 e^{-[Rb]l\sigma_{\pm P}^1(\nu)(\theta_p)} \quad (3.21)$$

and the cross sections for absorption are, adapting Eq. 3.2 for skew light propagation as described in [Chann et al., 2002b]

$$\sigma_{\pm P}^1(\nu) = \sigma_0(\nu)(1 \mp P_{\infty}(\nu)P \cos \theta_p) \quad (3.22)$$

We then extract the normalized circular dichroism from the corrected intensities

$$C(\nu) = \frac{-\ln(\frac{I_{-}}{I_0}) + \ln(\frac{I_{+}}{I_0})}{-\ln(\frac{I_{-}}{I_0}) - \ln(\frac{I_{+}}{I_0})} = \frac{\sigma_{-P}^1(\nu) - \sigma_{+P}^1(\nu)}{\sigma_{-P}^1(\nu) + \sigma_{+P}^1(\nu)} = PP_{\infty}(\nu) \cos \theta_p \quad (3.23)$$

Note that in forming  $C$ , the optical thickness  $[Rb]l$  and instrumental gains cancel. Thus, the density does not have to be measured to determine  $P_{\infty}$ , and  $P_{\infty}$  can be combined with previous measurements of  $\sigma_0$  ([Romalis et al., 1997]) to completely describe the resonant and near-wing light absorption. Combination with the measured  $P_{Rb}$  gives

$$P_{\infty}(\nu) = \frac{C(\nu)}{P_{Rb} \cos \theta_p} \quad (3.24)$$

When the pump polarization was reversed, the atomic polarization satisfied  $(1 - P_{Rb}) = (1 - |P_{Rb}'|)$  to within 5% at worst, and typically to within much less. The average of  $P_{Rb}$  and  $|P_{Rb}'|$  was used in calculating  $P_{\infty}$ .

Note that eq. 3.24 is not correct at the line center, where the hyperfine splitting of the Rb ground state is important. Although the hyperfine splittings (3.0 GHz for  $^{85}\text{Rb}$ , 6.8 GHz for  $^{87}\text{Rb}$ ) are smaller than the pressure-broadened atomic linewidth, the hyperfine effect on the measured normalized circular dichroism is striking, as shown in Fig. 3.6.

The shape of  $C$  near resonance is primarily due to a frequency shift between the absorption cross sections of light of  $\delta=\pm 1$ . An unpolarized vapor has the same cross section for absorption of light of any spin. In a highly polarized vapor, most of the atoms are pushed into a stretched state in the upper hyperfine manifold,  $|F = 2, m_F = 2\rangle$  for  $^{87}\text{Rb}$ , which does not absorb light of spin  $\delta = 1$  (for the case of full dichroism). The rest of the atoms are in other states of high  $m_F$  in both the upper and the lower hyperfine manifolds. The high- $m_F$  states in the upper manifold are preferentially electron-spin up, while those in the lower manifold are preferentially electron-spin down. Thus, in a spin-temperature-like distribution, most of the atoms that absorb light of spin  $\delta = 1$  are in the lower manifold, while the overwhelming majority of atoms absorbing light of  $\delta = -1$  are in the upper manifold. As the two manifolds have slightly different center frequencies, this leads to the structure shown in Fig. 3.5.

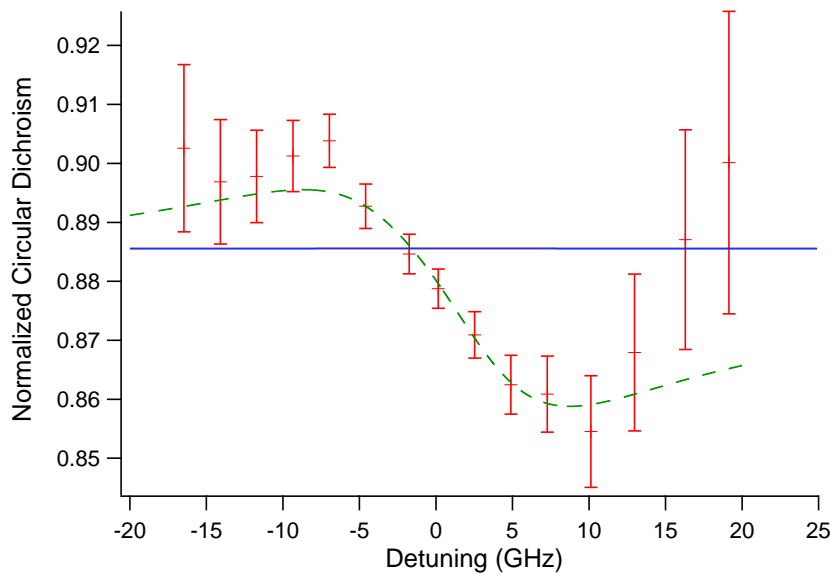


Figure 3.5 Normalized circular dichroism,  $C$ , near resonance, taken at a low density and low polarization,  $P_{\text{Rb}} = 0.929$ . Modeling with  $P_{\infty} = 1$  that omits the hyperfine splitting [solid (blue) line] predicts a nearly flat  $C$  at  $P_{\text{Rb}} \cos \theta_p$ . Modeling with  $P_{\infty} = 1$ , but including the ground-state hyperfine structure [dashed (green) line], is in good agreement with the data.

To model  $C$  for near-resonance conditions, we can write the spin-dependence of the cross sections  $\sigma_{Fm_F}^{\delta}$  in terms of the cross sections in the fine structure basis  $\sigma_{\pm}^{\delta}(\nu)$  (Eq. 3.1) [Chen et al., 2007,

Chann et al., 2002b] using Clebsch-Gordan coefficients. Ignoring small corrections due to the hyperfine structure of the excited state gives

$$\sigma_{Fm_F}^{\lambda}(\nu) = \sigma_0(\nu - \nu_F) \left(1 \mp \frac{m_F}{F} \lambda P_{\infty} \cos \theta_p\right) \quad (3.25)$$

for  $F = I \pm 1/2$ , where the center frequencies of the hyperfine lines are  $\nu_F$ . Note that, in these cross sections, reversing the sign of the alkali-metal spins  $m_F$  is equivalent to reversing the sign of the light spin  $\lambda$ . Then we can build the cross sections, using the populations  $\rho_{Fm_F}$  deduced from EPR spectroscopy,

$$\sigma_P^{\pm 1} = \sigma_{\pm P}^1 = \sum_F \sum_{m_F} \sigma_{Fm_F}^{\pm 1}(\nu) \rho_{Fm_F} \quad (3.26)$$

We can then write the equation for  $C$ , using the cross sections including the hyperfine structure, and invert it to solve for  $P_{\infty}$  from the near-resonance area.

For regions of the data where  $P_{\infty} \approx 1$ , it is particularly crucial to make an accurate measurement of  $1 - P$ . This was complicated by the fact that we did not achieve high atomic polarizations at low [Rb], where the on resonance data must be taken. At [Rb]  $\sim 1.5 \times 10^{12} \text{ cm}^{-3}$  we observed  $P$  from 90% to 95% in all three cells, while at [Rb]  $> 50 \times 10^{12} \text{ cm}^{-3}$  we observed  $P \geq 0.99$  in the He-N<sub>2</sub> cells, and  $P \sim 0.95$  in the N<sub>2</sub> cell. Since the atoms are not in spin-temperature equilibrium at low temperatures, we found it necessary to be able to resolve EPR peaks that were less than 1/500th the size of the primary peak to accurately deduce the polarization from the EPR peak areas. It was also necessary to measure the polarization of the two isotopes independently at low temperatures. Although the spin-polarization was typically the same in the two isotopes, spin temperature could not be used to predict the sublevel populations, and they had to be derived from the EPR spectra of the two isotopes. The typical uncertainty of the EPR measurements was  $\sim 10\%$  or less in  $(1 - P)$ . The details of the EPR spectroscopy diagnostic are described in detail in Chapter 2.

The failure of our laser to fully optically pump the atoms at low temperatures is a puzzle. The low polarization at low temperatures was insensitive to pump laser power and detuning and was observed for other cells as well. The natural explanation for this is poor circular polarization. At high temperatures, where the optical thickness is large, this would not be a problem, as the vapor

strongly attenuates light of the wrong polarization, allowing only light of the correct polarization to propagate through most of the cell. However, our measured circular polarization of  $> 99\%$  is much too high to explain the low atomic polarization at small optical thicknesses. Note that the low polarizations occur at temperatures where the vapor is not at spin temperature, but this should not significantly affect the polarization produced by a relatively spectrally broad pumping source.

For the near-resonance data taken in the spherical cells, the uncertainty in  $P$  was the largest uncertainty. Etalon interference effects in the walls of the cylindrical cell (0.75% to 1.0%) were comparable to the uncertainty in  $P$  near resonance and were the dominant contribution to the errors off-resonance. Etalon effects were smaller in the spherical cells ( $< 0.25\%$ ), where drifts in  $I_0$  (0.25% to 0.5%) dominated off-resonance uncertainties for the spherical SEOP cell, and relative intensity drift between the 795-nm and the 856-nm lasers (0.5%) was the primary source of off-resonant error in the pure  $N_2$  cell. For most of the frequency range covered, the data were taken at a high density where  $P$  was close to 1 and the uncertainty in  $P$  was a minor component of the total uncertainty. The uncertainties in the probe propagation angle and the measured probe intensities were small under all conditions.

### 3.9 Results

The measured  $P_\infty$  near resonance, from transmission data, for both SEOP cells is shown in Fig. 3.6.  $P_\infty$  drops significantly below 1 for much smaller detunings than a naive prediction using Lorentzian lineshapes for the D1 and D2 resonances predicts;  $P_\infty$  is much less than 1 within the typical 1000-GHz bandwidth of broadband sources such as diode array bars often used for SEOP. The implications of this finding are discussed in section 3.11. A very important result in Fig. 3.6 is the agreement between the two cells, despite their very different  $^3\text{He}$  pressures. At detunings outside the atomic linewidth of 15–60 GHz [Romalis et al., 1997], the absorption of  $\lambda = -1$  light is proportional to the buffer-gas pressure. Thus, only if the normally forbidden dark state absorption is also proportional to the buffer-gas pressure will the dichroism be pressure independent. The agreement between the two cells at different pressures confirms that the source of the impure dichroism in these cells is Rb-buffer-gas collisions.

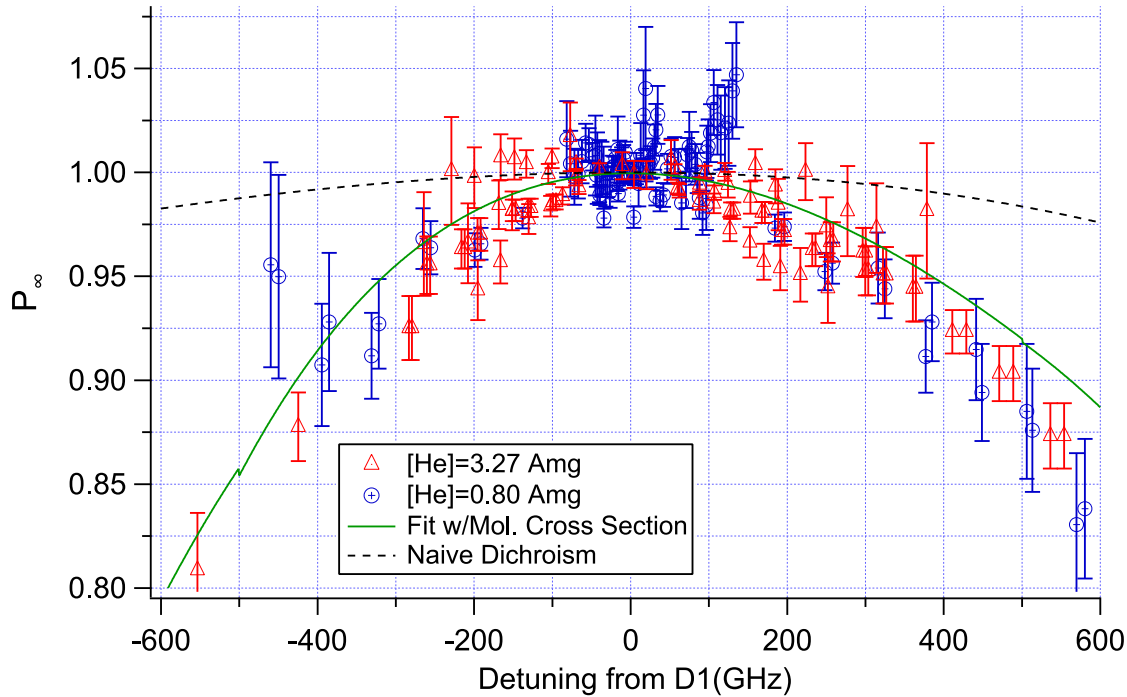


Figure 3.6  $P_\infty$  results near the D1 resonance line. The agreement between cells of different He pressure verifies that the effects originate from absorption in RbHe collisions. The dashed line denotes the frequency dependence of the dichroism, making the naive assumption of purely Lorentzian line broadening, and the solid line is the result of using the molecular absorption cross section from Eq. ??.

For NHRb, the high [ $^3\text{He}$ ] cell, we were able to measure  $P_\infty$  across the entire frequency range from the D1 to the D2 resonance, and this is plotted in Fig. 3.7. (The gap in the data from 784 to 786 nm is due to lack of coverage of that range by our two probe lasers.) The measurements are in good agreement with those made by Babcock using the distinct optical pumping method. As expected,  $P_\infty$  goes from +1 to -0.5 as the light is tuned between the two resonances. However, the sign of the dichroism flips at  $790.325 \pm 0.03$  nm, a significant shift from the 787.5-nm zero crossing that would result from a naive model that takes the cross section at each frequency to be the sum of Lorentzian pressure-broadened D1 ( $P_\infty = 1$ ) and D2 ( $P_\infty = -1/2$ ) line shapes.

To allow us to isolate the contributions of Rb- $\text{N}_2$  collisions, we measured  $P_\infty$  in the pure  $\text{N}_2$  cell (Fig. 3.8). Pure He cells cannot be used for these measurements because some  $\text{N}_2$  is necessary to prevent radiation trapping [Walker and Happer, 1997]. The results for  $\text{N}_2$  are quite similar to

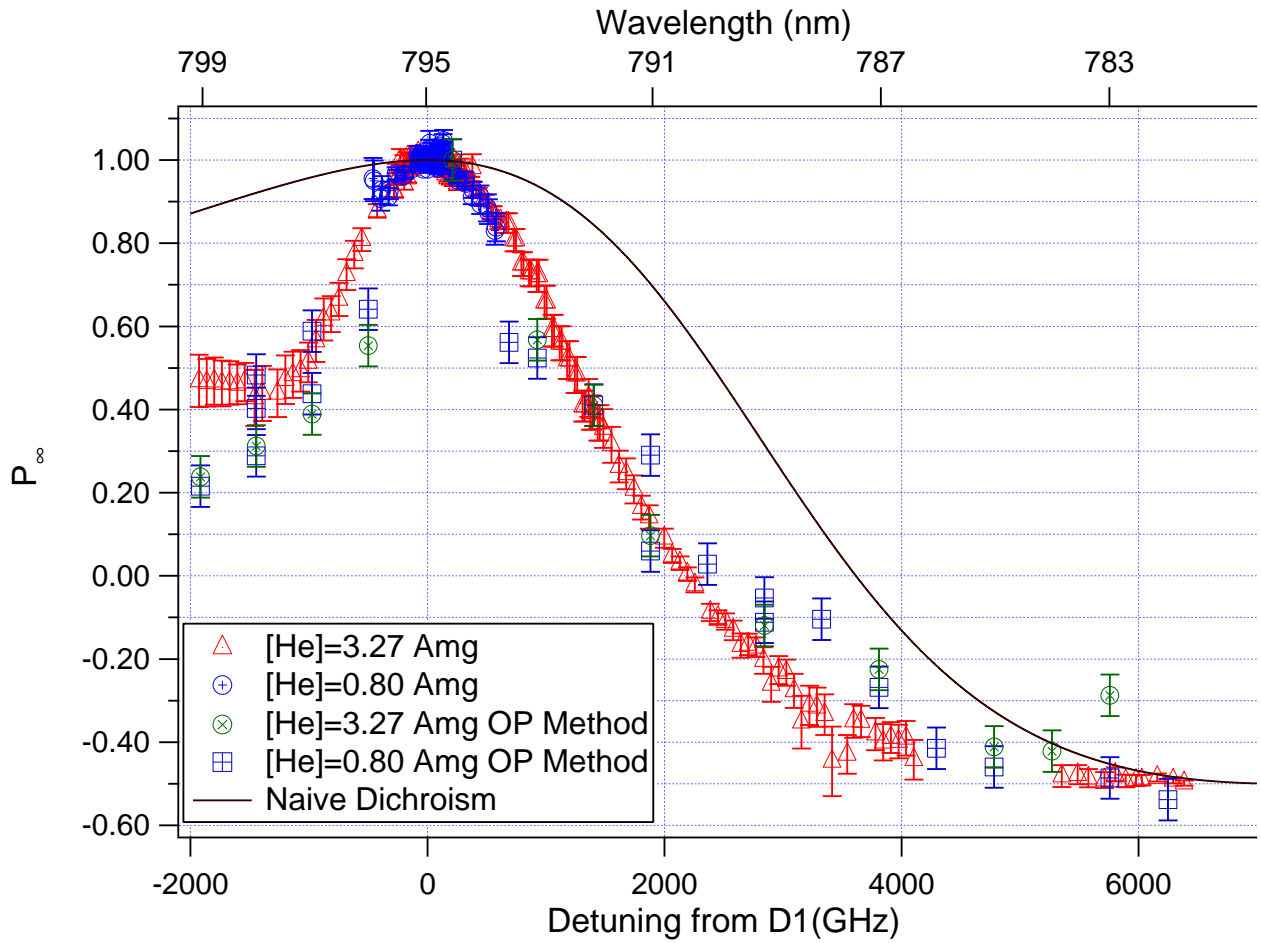


Figure 3.7 Measured  $P_\infty$  of RbHe molecules in the region between the first resonance lines of Rb. The solid curve shows the expected dichroism from the very naive assumption of purely Lorentzian broadened lines.

those found in the SEOP cells, meaning the dark state absorption cross sections per unit density are similar for RbHe and RbN<sub>2</sub> molecules. Thus, in general, the  $P_\infty$  we measured in SEOP cells can be used regardless of the particular ratio of <sup>3</sup>He and N<sub>2</sub> buffer gasses present, particularly if there is much more <sup>3</sup>He than N<sub>2</sub>. For the region of most interest for pumping, our measured  $P_\infty$  can be combined with the lineshape from [Romalis et al., 1997] to characterize absorption in optical pumping models.

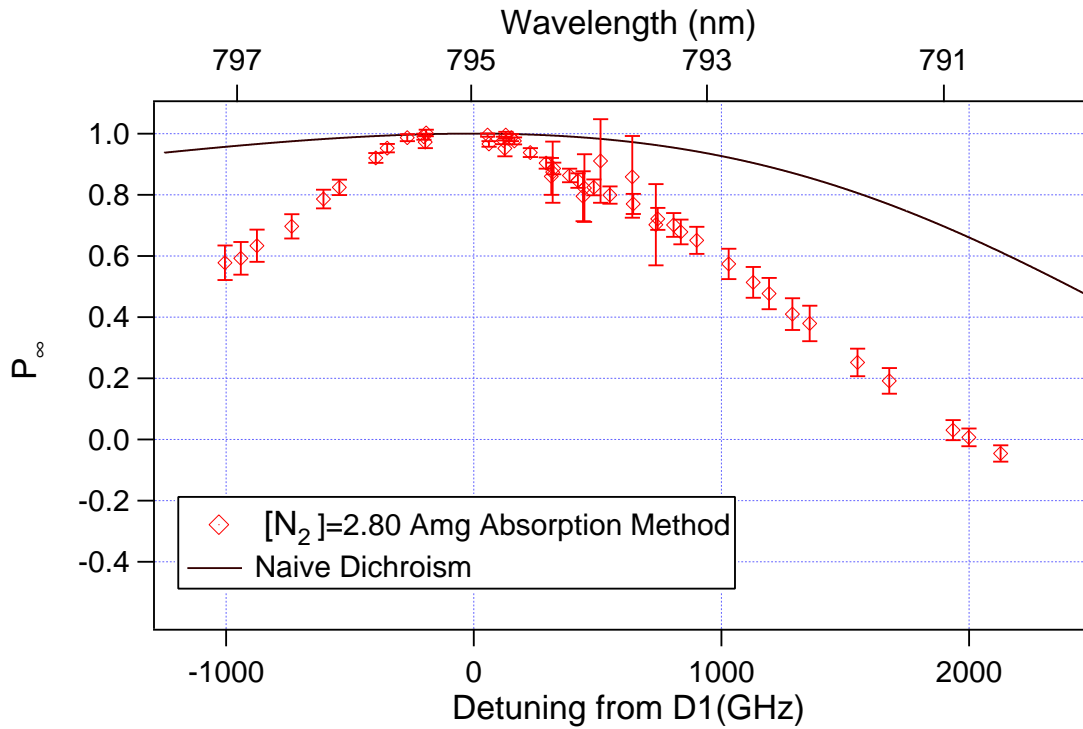


Figure 3.8 Measured  $P_\infty$  of RbN<sub>2</sub> molecules in the region between the first resonance lines of Rb. The solid curve shows the expected dichroism from the very naive assumption of purely Lorentzian broadened lines.

### 3.10 Cross-Sections

Given the importance of these measurements for D1 optical pumping, it is convenient to extract the absorption cross section for  $\lambda = 1$  light by fully polarized atoms. To find the cross section, we need to extract [Rb] from our data. To do this, we derive the product

$$[\text{Rb}]l\sigma_0 = \frac{-\ln(I_+/I_0) - \ln(I_-/I_0)}{2} \quad (3.27)$$

from the transmission data and fit it near resonance to the expected lineshape from [Romalis et al., 1997] to find [Rb], as described in detail in chapter 2.

Romalis *et al.* characterized the Rb-N<sub>2</sub> and Rb-<sup>3</sup>He absorption cross-sections at low [Rb] density, where for Rb-N<sub>2</sub> broadening at a similar [N<sub>2</sub>] to what in our N<sub>2</sub> cell they did not observe any deviation of their measured cross-section from a fit to the lineshape from [Walkup et al., 1984]. We also observe a good fit to the lineshape at small detunings. However, at high [Rb] and detunings

of more than  $\sim 200$  GHz our measured  $N_2$  transmission data deviate from the [Romalis et al., 1997] line shape. For data sets taken at larger detunings, measurements were overlapped in detuning with the previous set, so that [Rb] could be found by fixing the overlapping part of the cross section to that found in the previous set. The full range of  $\sigma_0$  for 2.80 amg of  $N_2$  buffer gas is shown in Fig. 3.9

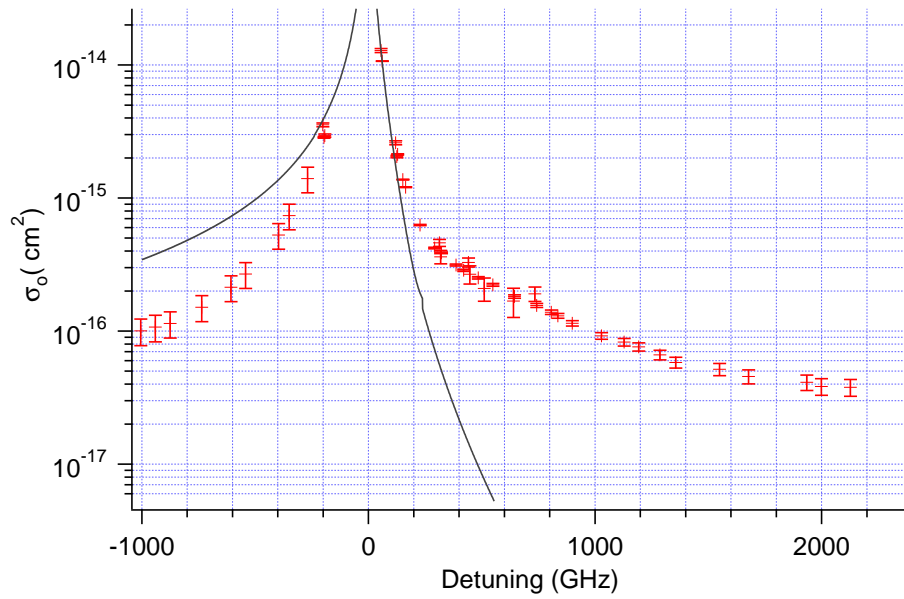


Figure 3.9 Cross section for absorption of unpolarized light by Rb atoms in the presence of 2.80 amg of  $N_2$  buffer gas. For detunings larger than  $\sim 200$ GHz, the lineshape deviates significantly from the lineshape in [Romalis et al., 1997](Solid black line).

Given  $\sigma_0$  and  $P_\infty$  for  $N_2$ , we then deduce  $\sigma_{\pm 1}^1$  in the pure  $N_2$  cell. Dividing this by  $[N_2]$  gives the cross sections for 1 amg  $N_2$ (Fig. 3.10). The dark state absorption cross section is non-resonant, as expected from absorption in Rb-buffer gas molecules, and a linear fit gives the dark state cross section per amg  $N_2$

$$\sigma^1(\nu) = \sigma_1^1(\nu_1) + (\nu - \nu_1) \left. \frac{d\sigma_1^1}{d\nu} \right|_{\nu_1} \quad (3.28)$$

$$\frac{\sigma_1^1(\nu_1)}{[N_2]} = 1.49 \pm 0.15 \times 10^{-17} \text{cm}^2/\text{amg} \quad (3.29)$$

$$\frac{1}{[N_2]} \left. \frac{d\sigma^1}{d\nu} \right|_{\nu_1} = -6 \pm 5 \times 10^{-22} \text{cm}^2/(\text{amg GHz}) \quad (3.30)$$

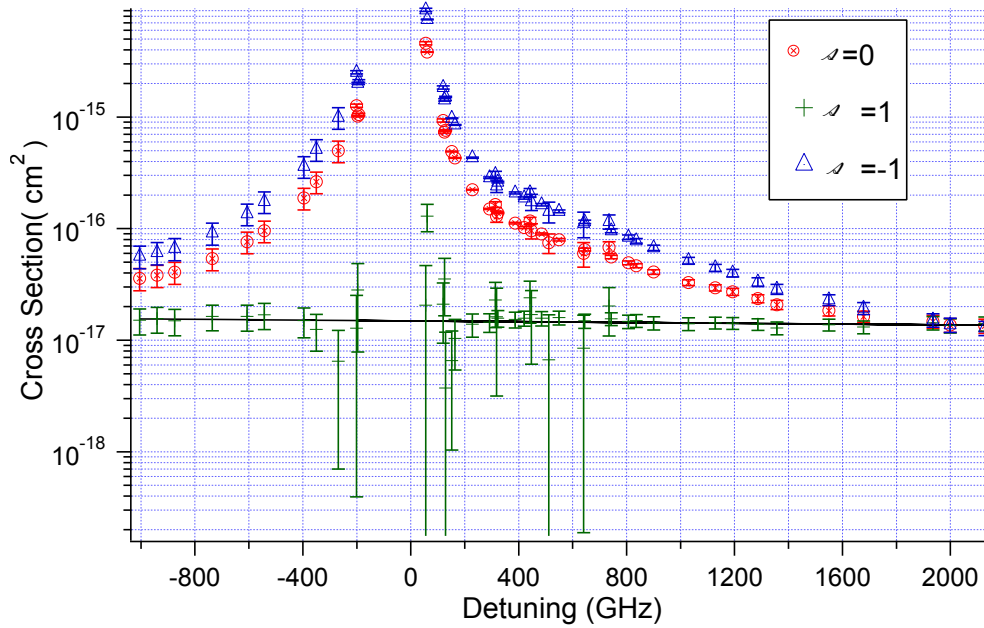


Figure 3.10 Cross sections, normalized to a 1-amg  $N_2$  density, for absorption of  $\delta = 1$ ,  $\delta = -1$ , and  $\delta = 0$  light by fully polarized Rb atoms. The solid line is the linear fit to the  $\delta = 1$  data

Similarly, the density can be extracted from the SEOP cell data near resonance using the  $Rb^3He$  and  $RbN_2$  lineshapes from [Romalis et al., 1997]. The product  $[Rb]l$  is fit to the lineshape in Eq. 2.40 with a linewidth equal to the sum of  $[^3He]$  times the  $Rb^3He$  broadening coefficient and  $[N_2]$  times the  $RbN_2$  broadening coefficient, and with an asymmetry parameter

$$T'_d = \frac{T_{d,^3He}[^3He] + T_{d,N_2}[N_2]}{[^3He] + [N_2]} \quad (3.31)$$

Our measured lineshapes fit well to the Romalis *et al.* lineshape in the region of detunings from  $\sim -650$  GHz to  $\sim +750$  GHz. The data also deviates from the Romalis *et al.* lineshape in the far wing of the D2 resonance. Our measurements did not extend into the near wing of the D2 resonance. Again, for larger detunings, densities were determined by overlapping high  $[Rb]$  datasets with calibrated data sets at lower  $[Rb]$ . To extract the dark state absorption due to  $Rb^3He$  collisions, the linear fit to the dark state absorption cross section in  $RbN_2$  collisions was scaled to  $[N_2]$  in each SEOP cell and subtracted from the total dark state absorption cross section. Then the cross sections from the two SEOP cells were divided by  $[^3He]$  in each cell to give the dark state absorption due to  $RbHe$  collisions at  $[^3He]=1$  amg (Fig. 3.12) The dark state absorption cross section due to  $RbHe$

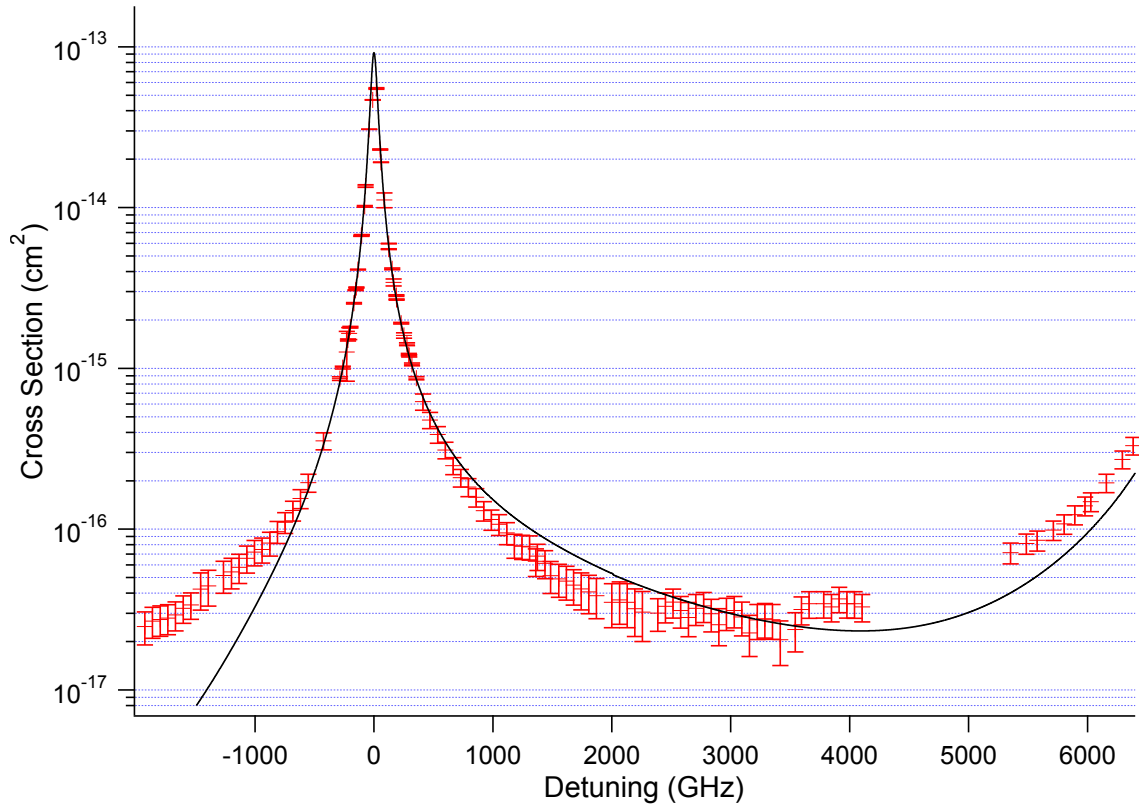


Figure 3.11 Cross section for absorption of unpolarized light by Rb atoms in the presence of 3.27 amg of  $^3\text{He}$  buffer gas. For detunings larger than  $\sim 700\text{GHz}$ , the lineshape deviates significantly from the lineshape in [Romalis et al., 1997](Solid black line). The rise in cross section on the right side of the data is the D2 resonance.

molecules is also non-resonant, as expected from inspection of the RbHe molecular potentials. A linear fit in the region near the D1 resonance gives

$$\frac{\sigma_1^1(\nu_1)}{[{}^3\text{He}]} = 1.10 \pm 0.12 \times 10^{-17} \text{cm}^2/\text{amg} \quad (3.32)$$

$$\frac{1}{[{}^3\text{He}]} \left. \frac{d\sigma^1}{d\nu} \right|_{\nu_1} = 6 \pm 5 \times 10^{-22} \text{cm}^2/(\text{amg GHz}) \quad (3.33)$$

Our estimate of the absorption cross section  $\sigma^1 = 9.4 \times 10^{-18} \text{cm}^2$  is very close to the measured value. Given that we have ignored rotational coupling of the adiabatic curves and the anisotropic nature of the light-molecule Rabi coupling, this excellent agreement may be considered somewhat fortuitous. Nevertheless, it confirms that it is quite reasonable for the circular dichroism of RbHe molecules to be at the level we observe in the experiment.

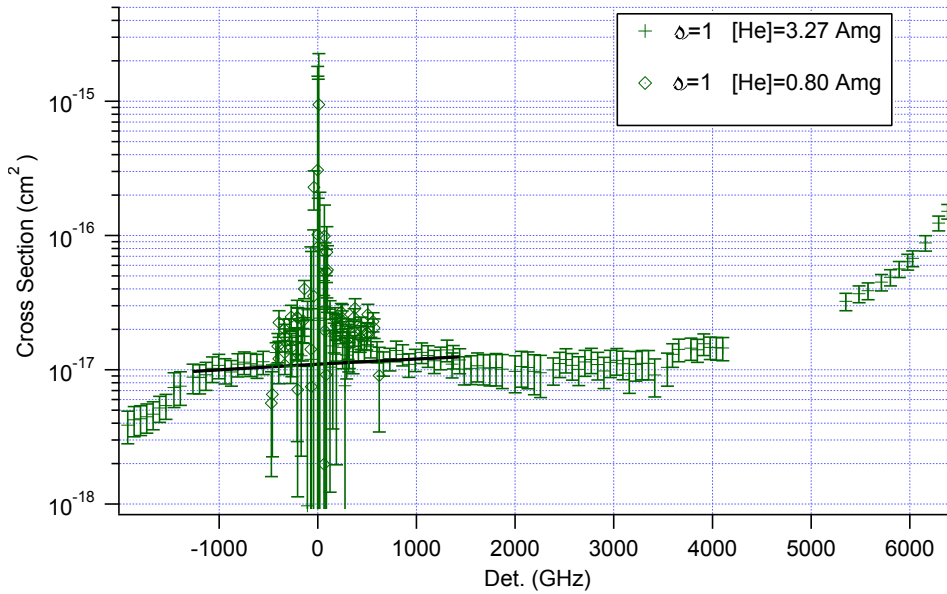


Figure 3.12 Cross section for dark state absorption due to RbHe molecules, normalized to 1 amg  $^3\text{He}$  density. The solid line is a linear fit in the region of the D1 resonance.

To extract the absorption cross section for unpolarized light due to Rb $^3\text{He}$  collisions, the cross section due to RbN $_2$  collisions was subtracted from the total cross section. In the line center region, the Romalis *et al.* lineshape was used, and for the wings a fit was made to our measured RbN $_2$  cross section at [N $_2$ ]=2.80 amg (Appendix D) and it was scaled assuming that the cross section is linear in [N $_2$ ] in the wings. The extracted cross section is shown in Fig. 3.11

### 3.11 Significance

We now turn to the implications of these results for spin-exchange optical pumping of  $^3\text{He}$ . With the advent of high-power diode-array bars having tens to hundreds of watts of low-cost power available at 795 nm, it has become standard practice to use these lasers for SEOP [Driehuys *et al.*, 1996]. One drawback of these lasers is that they have relatively broad spectral widths, typically several nanometers (1 nm = 475 GHz at 795 nm). This was shown to be mitigated by the practice of running at multiatmosphere  $^3\text{He}$  pressures, where the atomic line could be broadened and directly interact with a more substantial fraction of the laser linewidth [Driehuys *et al.*, 1996]. However, the highest  $^3\text{He}$  polarizations, about 80%, have only been obtained with spectrally narrowed lasers

[Chen et al., 2007, Chann et al., 2000, Chann et al., 2003]. We shall see that the dark state absorption explains much of this behavior, since the off-resonant light of an un-narrowed laser is absorbed by Rb-buffer-gas molecules. In addition, the frequency spectrum of the light changes as the light propagates through the cell, as the resonant portions of the spectrum are preferentially attenuated, while the off-resonant portions experience little attenuation. This causes a further decrease in the effective dichroism as the light propagates. We begin by generalizing Eq. 3.3 to pumping sources with nonzero bandwidth.

$$\frac{dF_z}{dt} = -\frac{1}{2} \left( \int_0^\infty \phi(\nu) \sigma_0(\nu) (1 - P_\infty(\nu)) d\nu \right) \rho_{1/2} + -\frac{1}{2} \left( \int_0^\infty \phi(\nu) \sigma_0(\nu) (1 + P_\infty(\nu)) d\nu \right) \rho_{-1/2} - \Gamma_{Rb} \frac{P}{2} \quad (3.34)$$

where the first term represents pumping out of the dark state, which leads to the loss of -1/2 unit of angular momentum per excitation, and the second term is pumping out of the normally allowed spin down ground-state. This can be written

$$\frac{dF_z}{dt} = \frac{1}{2} \left( \int_0^\infty \phi(\nu) \sigma_0(\nu) P_\infty(\nu) d\nu - \int_0^\infty \phi(\nu) \sigma_0(\nu) (\rho_{1/2} - \rho_{-1/2}) \right) - \Gamma_{Rb} \frac{P}{2} \quad (3.35)$$

$$= \frac{1}{2} \left( \int_0^\infty \phi(\nu) \sigma_0(\nu) P_\infty(\nu) d\nu - R_p P \right) - \Gamma_{Rb} \frac{P}{2} \quad (3.36)$$

In steady state, the spin polarization is

$$P = \frac{\int_0^\infty \phi(\nu) \sigma_0(\nu) P_\infty(\nu) d\nu}{R_p + \Gamma_{Rb}} \quad (3.37)$$

To explore the consequences of reduced dichroism for optical pumping at high densities, we have simulated the optical pumping and light propagation effects as described fully in Chapter 6. At each point in the optical pumping cell, the pumping rate is calculated from the spectral profile of the light at that position, using our measured  $\sigma_0$ , and the atomic polarization is calculated from the pumping rate  $R_p$ ,  $P_\infty$  and the ground-state spin-relaxation rate  $\Gamma_{Rb}$  (calculated as described in [Chen et al., 2007]) according to Eq. 3.37. Then the spectral profile of the light is propagated to the next place in the cell using

$$\frac{dI(\nu)}{dz} = -[\text{Rb}] \sigma_0(\nu) I(\nu) (1 - P P_\infty(\nu)) \quad (3.38)$$

The diffusion layer at the front of the cell is accounted for in an approximate manner using the model in Ref. [Walker and Happer, 1997]. Heating effects [Walter et al., 2001] have been neglected. The electron spin is assumed to completely relax in the excited state, and the nuclear spin is assumed to be conserved in the excited state.

The effects of reduced dichroism are most readily seen for broadband pumping light at a high [He], shown in Fig. 3.13. We assume that 100 W of broadband pumping light (spectral profile shown in Fig. 3.14) enters a 10-cm-diameter, 7-cm-long cell with 8 atm of  $^3\text{He}$  and 50 Torr of  $\text{N}_2$ , with  $[\text{Rb}] = 4 \times 10^{14} \text{ cm}^{-3}$ . Under these conditions, we estimate a spin-relaxation rate of 630/s [Chen et al., 2007]. Without dark state absorption, the light is attenuated only due to ground-state spin relaxation, and the 35 W dissipated in the cell is consistent with this. The polarization is maintained at a very high level, averaging 97%, as the pumping rate has not been sufficiently reduced to cause a substantial Rb polarization drop at the back end of the cell. The on-resonant portion of the laser spectral profile is not yet completely attenuated, as shown in Fig. 3.14, again consistent with maintenance of a high pumping rate. When the reduced dichroism is taken into account, several changes occur. The power dissipation per unit length is substantially increased, as shown in Fig. 3.13, even at the entrance to the cell before the spectral hole is burned. The total power dissipation is much greater than in the ideal case, now 65 W. The polarization drop is now quite substantial, decreasing to 75% at the back of the cell. This is due to two effects: (i) the pumping rate is lower at the back of the cell, compared to the ideal case, due to the greater power dissipation and the production of a complete hole in the spectral profile (shown in Fig. 13), and (ii) the remaining light is in the off-resonant spectral region with low circular dichroism. The removal of the resonant portion of the pump spectrum has greatly reduced the optical pumping rate, while the broadband dark state absorption, which competes with the optical pumping, has been reduced by a smaller amount.

This cell is very similar to those used in [Chen et al., 2007], yet the model predicts a  $P_{\text{Rb}}$  that is only slightly reduced at the front of the cell due to dark state absorption. This implies that the effective  $P_\infty$  for the pump laser is much greater than the  $P_{\text{max}}=0.91$  observed in [Babcock et al., 2003].

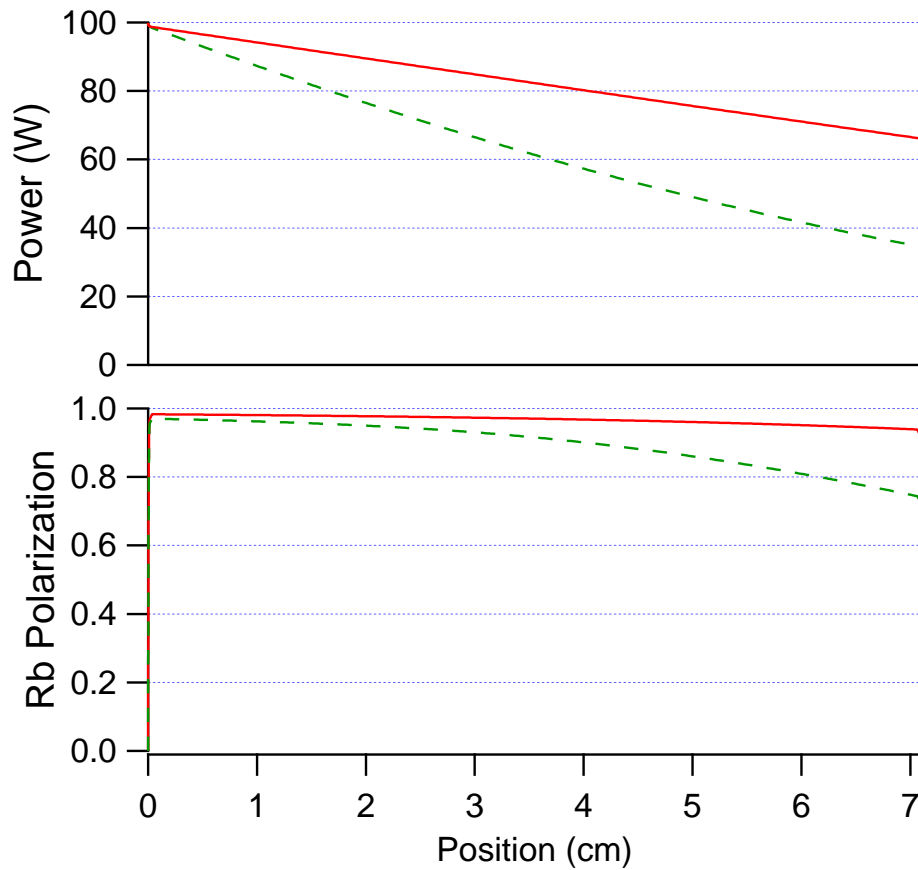


Figure 3.13 Light propagation results without [solid (red) line], and with [dashed (green) line] dark state absorption, for pumping with a laser whose spectral profile is shown in Fig. ???. Top: power as a function of position. The reduced dichroism produces a faster attenuation of the light. Bottom: Corresponding Rb polarizations, which are limited to values less than 100% even at the cell entrance, but then decay further as the spectral profile of the light is increasingly off-resonant (see Fig. 3.14)

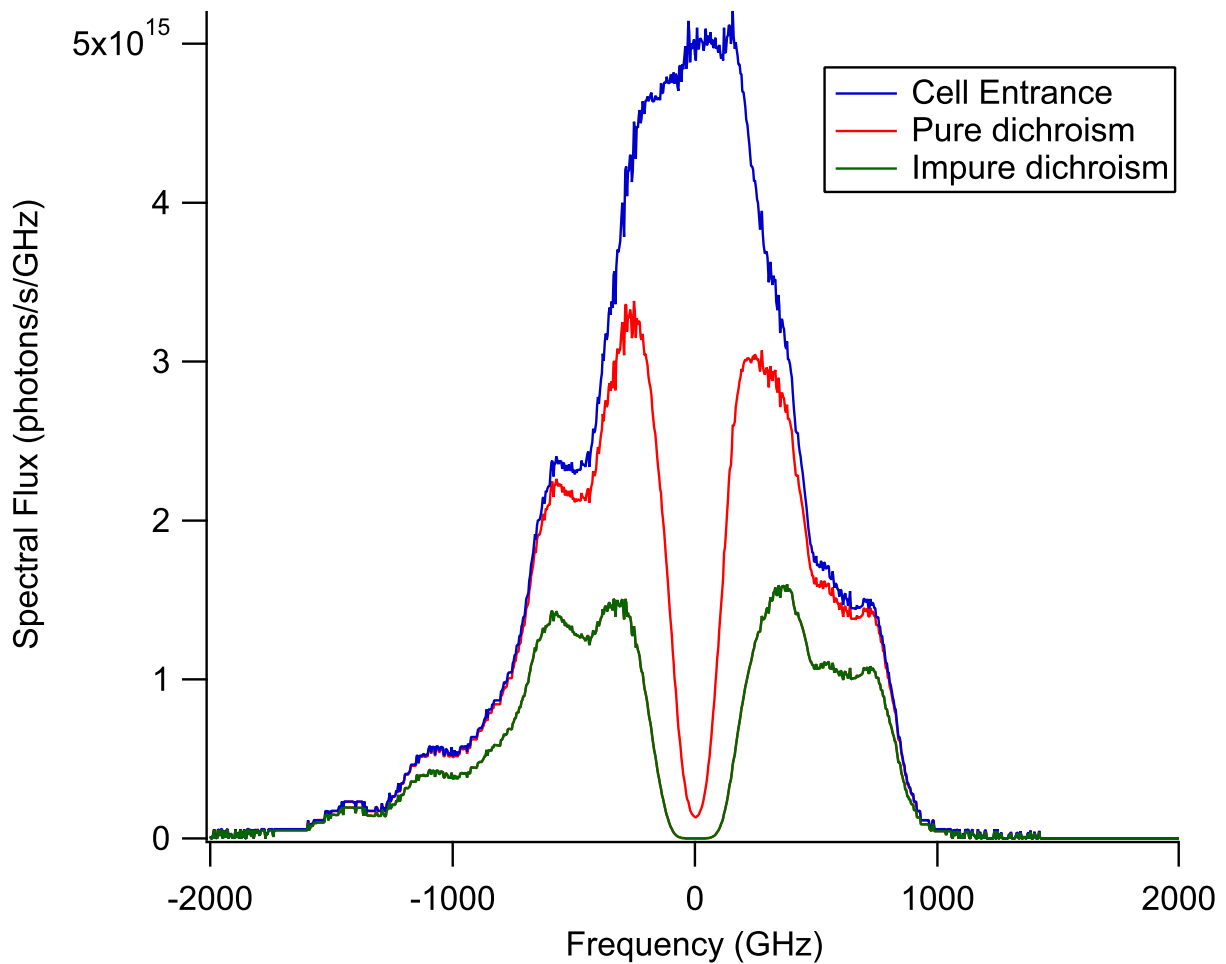


Figure 3.14 Measured spectra before and modeled spectra after propagation through the cell shown in Fig. 3.13, modeled as described in the text. Light in the wings of the spectrum contributes disproportionately to the dark state absorption, while contributing comparatively less to the resonant, dipole allowed D1 absorption. The net effect is significantly greater absorption than expected.

If we define the effective  $P_\infty$ ,

$$P_\infty^{eff} = \frac{\int_0^\infty \phi(\nu)\sigma_0(\nu)P_\infty(\nu)d\nu}{\int_0^\infty \phi(\nu)\sigma_0(\nu)d\nu} \quad (3.39)$$

This should be equivalent to  $P_{max}$  as derived in [Chen et al., 2007]. Calculated from the initial pump spectrum in our simulation,  $P_\infty^{eff} = .988$ , much higher than 0.91. After the light has propagated through the cell, and the resonant portion removed from the spectrum,  $P_\infty^{eff} = .930$ . Still, the inclusion of the reduced  $P_\infty$  greatly reduces the modeled photon efficiency. The model predicts that the ratio of the photon efficiency to the spin exchange efficiency  $\frac{\eta_\gamma}{\eta_{se}} = 0.53$ .

## Chapter 4

### Potassium Absorption at Rb D1 Resonance

#### 4.1 Motivation

Previous HySEOP experiments [Babcock et al., 2003, Chen et al., 2007] found that at high K to Rb density ratios  $\mathcal{D}$  it was not possible to optically pump alkali atoms to full polarization, even at very high optical pumping rates. Babcock *et al.* measured the alkali-metal polarization as a function of pumping rate in a series of [He]=8 amg cells with  $\mathcal{D}$  from 0 to 500. From these measurements they deduced  $P_{max}$ , the alkali-metal polarization with infinite pumping power(Fig. 4.1).

They found that  $P_{max}$  fell off dramatically with increasing  $D$ . The most natural explanation for this is that there is weak off-resonant optical pumping of the K atoms by the 795 nm pumping light. Assuming no spin-dependence to this absorption, this acts as a light-induced spin relaxation mechanism that keeps the atoms from becoming fully polarized. This assumption seems justified by the fact that the detuning of the 795nm light from the potassium D1 and D2 resonances is large compared to the splitting between the two resonances. Since the fine structure is unresolved, there should be no spin dependence to the absorption.

If the alkali-metal atoms are in spin-temperature equilibrium, so that their electronic spin-polarizations  $P$  are equal, and ground state spin relaxation can be ignored, the optical pumping equation becomes

$$[\text{Rb}]\frac{dF_R}{dt} + [\text{K}]\frac{dF_K}{dt} = [\text{Rb}]\frac{R_p}{2}(P_\infty - P) - [\text{K}]\frac{R_K}{2}P \quad (4.1)$$

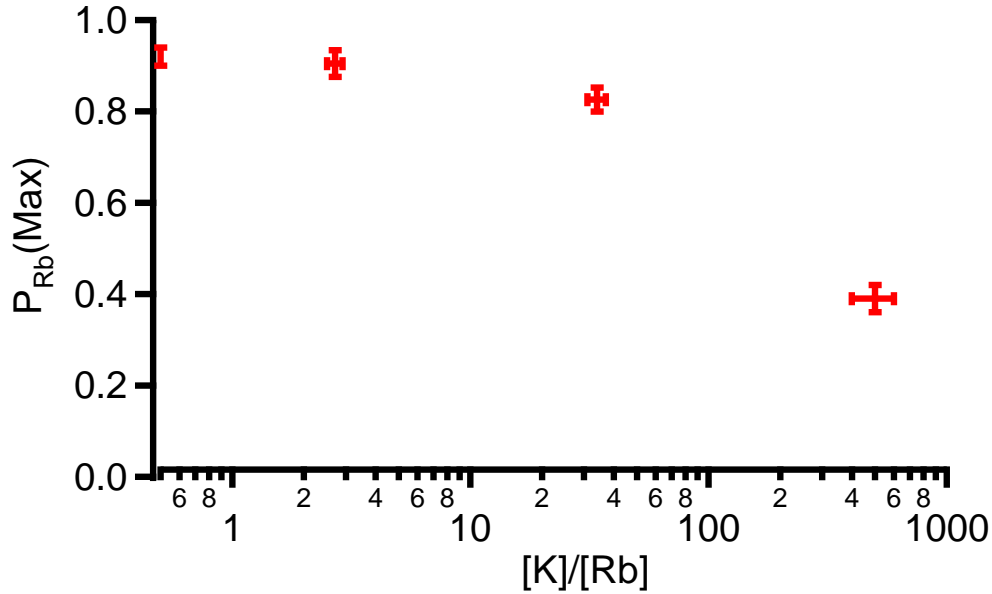


Figure 4.1 Alkali-metal polarization with infinite pumping power,  $P_{max}$ , measured as a function of K to Rb density ratio  $\mathcal{D}$  measured in [Babcock et al., 2003].

which is basically a statement of angular momentum conservation. The total angular momentum density  $[\text{Rb}]F_R + [\text{K}]F_K$  of the Rb and K atoms increases by optical pumping of the Rb atoms at a rate  $R_p$ , increasing  $P$  towards its maximum possible value  $P_\infty$  [Lancor et al., 2010a, Lancor et al., 2010b]. The angular momentum is also relaxed by light absorption at a rate  $R_K$  by the potassium atoms. The factors of 1/2 assume relaxation of the electronic angular momentum in the excited state, and that sufficient  $\text{N}_2$  quenching gas is included in the cell so that the nuclear spin is conserved in the excited-state [Lancor and Walker, 2010].

In steady-state, the polarization becomes

$$P = P_\infty \frac{[\text{Rb}]R_p}{R_p[\text{Rb}] + R_K[\text{K}]} = P_\infty \frac{R_p}{R_p + \mathcal{D}R_K} \quad (4.2)$$

so the spin-polarization is significantly reduced when  $\mathcal{D}R_K$  becomes comparable to  $R_p$ . Since both  $R_p$  and  $R_K$  are proportional to the pumping light intensity, the attainable polarization saturates at a value less than  $P_\infty$ . As has been noted before [Babcock et al., 2003, Lancor et al., 2010b], the

extreme optical depths of SEOP experiments make them particularly sensitive to such polarization limiting processes, because the vapor does not become transparent to the pumping light.

In this chapter we discuss an experiment measuring the absorption of K atoms at the 795nm Rb D1 resonance frequency due to K-<sup>3</sup>He and K-N<sub>2</sub> collisions. The cross sections were found to be, as published in [Lancor and Walker, 2011],

$$\sigma_{\text{K-He}} = 2.19 \pm .39 \times 10^{-18} \frac{\text{cm}^2}{\text{amg}} [\text{He}] \quad (4.3)$$

and

$$\sigma_{\text{K-N}_2} = 8.8 \pm 7.6 \times 10^{-18} \frac{\text{cm}^2}{\text{amg}} [\text{N}_2] \quad (4.4)$$

These cross-sections are shown to explain the low maximum alkali-metal polarizations at high  $D$ .

## 4.2 Experimental Procedure

Using the apparatus described in detail in Chapter 3, we deduced the absorption cross section  $\sigma_K$  for K atoms near the Rb pumping wavelength of 795 nm. We measured the relative transmission  $1 - e^{-[\text{K}]\sigma l}$  of a weak (50 $\mu$ W) linearly-polarized probe beam through 2 K cells, one  $l = 4.8$  cm diameter sphere containing 0.063 amg of N<sub>2</sub> and 2.93 amg of <sup>3</sup>He and one  $l = 5.7$  cm sphere with 0.083 amg N<sub>2</sub> and 0.924 amg of <sup>3</sup>He. First, the transmission was measured at room temperature, to obtain the cell transmission with no alkali gas. Then, the cell was heated to achieve the desired [K] and the transmission was measured again. Dividing by  $I_0$  gives the relative transmission. The transmission of a second probe beam at 855 nm, spatially overlapped with the first, was also monitored to account for drifts in the cell transmission that occur due to K droplet formation and migration on the cell walls. The measured K transmissions ranged from 99% to 100%, depending on the cell and temperature used.

The potassium density [K] and the helium density [He] were deduced from K line-center absorption spectroscopy using the recently measured K-<sup>3</sup>He lineshape [Singh, 2010]. The procedure of fitting transmission data is the same as that for Rb-<sup>3</sup>He described in chapter 2. The K-<sup>3</sup>He asymmetry parameter is unknown, but our data fit well with an asymmetry parameter of zero. This is not surprising given the small asymmetry of the Rb-<sup>3</sup>He and Na-<sup>3</sup>He D1 lineshapes([Romalis et al., 1997,

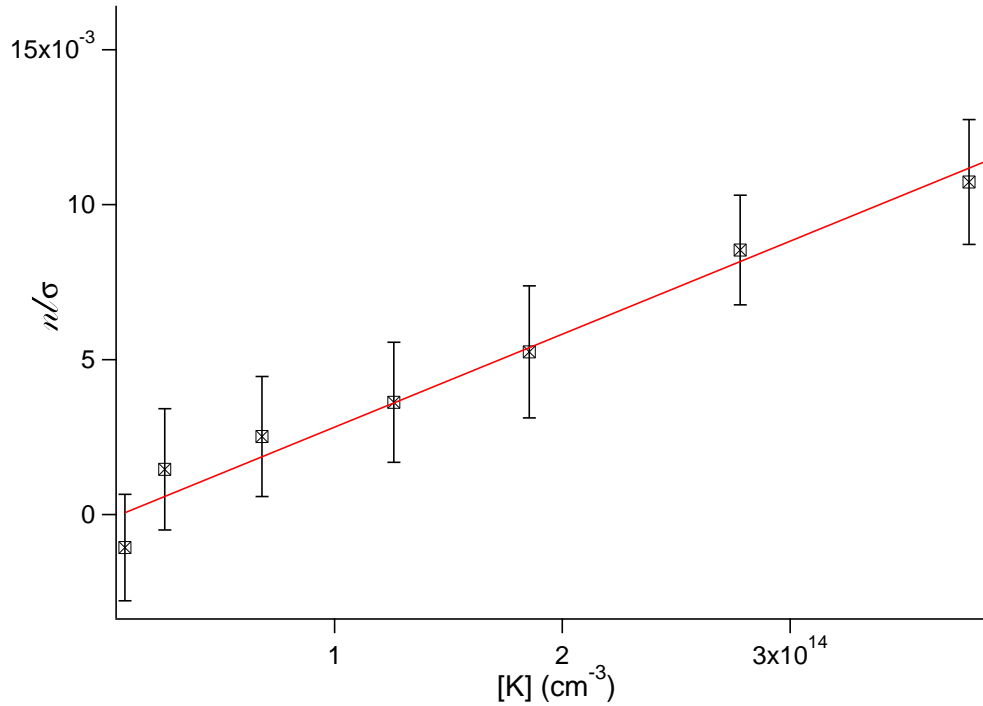


Figure 4.2 Optical thickness at 794.41 nm, as a function of [K] in [He]=2.93 amg cell. The slope of the linear fit gives  $l\sigma$ . The y-intercept of the fit is fixed at zero.

Kielkopf, 1980]). A measurement of the potassium absorption at relatively low potassium density, where the line center absorption is modest, was fit to the K-<sup>3</sup>He lineshape. Under these conditions, the linewidth can be determined precisely, and [He] deduced. Knowing [He], fits of absorption spectra have only [K] as a free parameter, and [K] can be determined precisely.

Measurements of the absorption cross-sections in the two cells were made over a range of wavelengths near 795 nm. We avoided measurements directly at the 795nm Rb D1 resonance, due to an observable, resonant Rb absorption. We performed transmission spectroscopy on the Rb at 795nm in the high [He] cell, from which we extracted [He]=2.93 amg by fitting to the Rb-<sup>3</sup>He lineshape, in agreement with the value obtained from K-<sup>3</sup>He spectroscopy. This differs slightly from the value 3.03 amg inferred from the intended fill pressure. We were also able to compare [Rb] and [K] at  $T \approx 200$  °C to determine that  $D \approx 10000$  in the nominally pure K cell. At the detunings used for determining the K-<sup>3</sup>He absorption cross-section, Rb absorption was negligible.

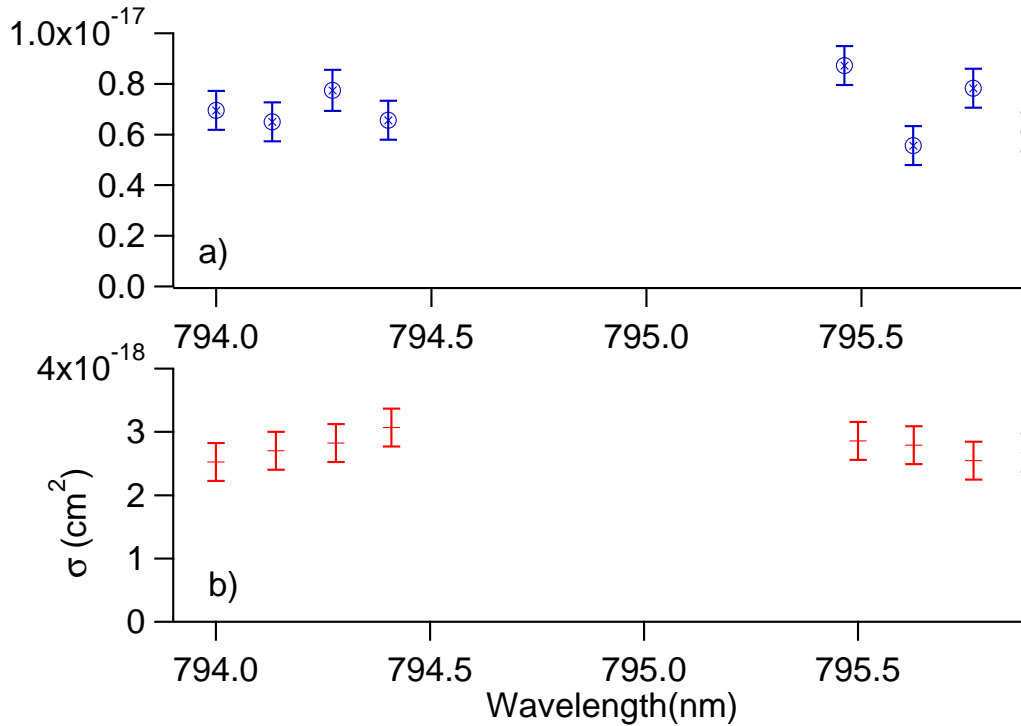


Figure 4.3  $\sigma$  as a function of wavelength in cells of a)  $[\text{He}] = 2.93 \text{ amg}$  and b)  $[\text{He}] = .0924 \text{ amg}$ . Due to 1/10000 Rb contamination of this nominally pure K cell, we avoid measurements directly on the Rb resonance.

At each wavelength, the absorption was measured at several temperatures, corresponding to several potassium densities. A plot of the optical depth versus potassium density (Fig. 4.2) was made and the cross section for absorption deduced from dividing the slope of a linear fit, with the y-intercept fixed to zero, by the length  $l$  of each cell. The deduced cross sections are shown as a function of wavelength in Fig. 4.3.

The uncertainty in the measurements arises mainly from etalon effects on the transmission of the 795 nm and 850 nm probe beams. The etalon fringing gives a small frequency variation to the transmission through the oven and cell walls, that shifts with temperature. The size of the fringing is measured at room temperature, and the magnitude is applied as an uncertainty to the determination of  $I_0$ , what the transmission would be at high temperature without alkali gas. Etalon effects contributed an uncertainty of 0.11% to the transmission of both beams in the high

$^3\text{He}$  cell, and 0.07% to the transmission in the low  $^3\text{He}$  cell. In the low  $^3\text{He}$  density cell, there is also a 0.10% percent uncertainty in the correction of  $I_0$  due to migration of K droplets on the cell wall. Considering that the measured absorptions were all  $\leq 1.0\%$ , these small uncertainties in the transmission are large uncertainties in the absorption. There are small contributions from uncertainty in the path length (2.5% in the high  $^3\text{He}$  cell and 2.1% in the low  $^3\text{He}$  cell).

### 4.3 K-He Cross Section

In both cells, there was no discernible frequency dependence to the absorption (Fig. 4.3), so weighted averages of all the measured cross-sections were taken as the cross-sections at the Rb D1 resonance. Using the cross-sections and  $^3\text{He}$  and  $\text{N}_2$  densities from the two cells we obtain the K- $^3\text{He}$  and K- $\text{N}_2$  cross sections

$$\sigma_{\text{K-He}} = 2.19 \pm .39 \times 10^{-18} \frac{\text{cm}^2}{\text{amg}} [\text{He}] \quad (4.5)$$

and

$$\sigma_{\text{K-N}_2} = 8.8 \pm 7.6 \times 10^{-18} \frac{\text{cm}^2}{\text{amg}} [\text{N}_2] \quad (4.6)$$

The large uncertainty in the  $\text{N}_2$  cross section is due to the low abundance of  $\text{N}_2$  in the cells used.

The cross section being measured here corresponds to absorption in the quasistatic wings of the K resonance line [Allard and Kielkopf, 1982]. Recent theoretical investigation of K- $^4\text{He}$  far wing line broadening in the context of understanding the spectra of cool brown dwarfs were reported in [Allard et al., 2003]. They present a plot of the cross-section due to K- $^4\text{He}$  collisions as a function of wavelength at  $[\text{He}] = 1 \times 10^{19}$  and at  $T = 227^\circ\text{C}$ . Assuming the cross-section scales linearly with  $[\text{He}]$ , the value at 795nm gives  $\sigma_{\text{K-}^4\text{He}} = 2.7 \times 10^{-18} \frac{\text{cm}^2}{\text{amg}} [^4\text{He}]$ , within  $2\sigma$  of our result.

### 4.4 Significance

We now want to evaluate the effect of this absorption by K- $^3\text{He}$  molecules on optical pumping of K-Rb mixtures. The standard equation for the evolution of the alkali-metal spins during

HySEOP is [Babcock et al., 2003]

$$[\text{Rb}] \frac{dF_z^{\text{Rb}}}{dt} + [\text{K}] \frac{dF_z^{\text{K}}}{dt} = [\text{Rb}] R_p \frac{1}{2} (1 - P_A) - ([\text{Rb}] \Gamma_{\text{Rb}} + [\text{K}] \Gamma_{\text{K}}) P_A \quad (4.7)$$

Generalizing this equation to account for a broadband pump, dark state absorption as discussed in the previous chapter (Eq. 3.36), and absorption by K-<sup>3</sup>He molecules give

$$[\text{Rb}] \frac{dF_z^{\text{Rb}}}{dt} + [\text{K}] \frac{dF_z^{\text{K}}}{dt} = [\text{Rb}] \frac{1}{2} \left( \int_0^\infty \phi(\nu) \sigma_0(\nu) P_\infty(\nu) d\nu - R_p P_A \right) - \frac{1}{2} \left( [\text{Rb}] \Gamma_{\text{Rb}} + [\text{K}] (\Gamma_{\text{K}} + R_K) \right) P_A \quad (4.8)$$

where  $R_K = [\text{He}] \int_0^\infty \phi(\nu) \sigma_{\text{K-}^3\text{He}}(\nu) d\nu$ . Inserting the density ratio  $D$ , we get

$$\frac{1}{D} \frac{dF_z^{\text{Rb}}}{dt} + \frac{dF_z^{\text{K}}}{dt} = \frac{1}{2D} \left( \int_0^\infty \phi(\nu) \sigma_0(\nu) P_\infty(\nu) d\nu - R_p P_A \right) - \frac{1}{2} \left( \frac{\Gamma_{\text{Rb}}}{D} + (\Gamma_{\text{K}} + R_K) \right) P_A \quad (4.9)$$

The steady state solution is

$$P_A = P_\infty^{\text{eff}} \frac{R_p/D}{R_p/D + \Gamma_{\text{Rb}}/D + \Gamma_{\text{K}} + R_K} \quad (4.10)$$

where, as defined in Chapter 3,  $P_\infty^{\text{eff}} = \frac{\int_0^\infty \phi(\nu) \sigma_0(\nu) P_\infty(\nu) d\nu}{R_p}$ . In the limit of infinite pumping power, the steady state solution goes to

$$P_{\text{max}} = P_\infty^{\text{eff}} \frac{R_p/D}{R_p/D + R_K} \quad (4.11)$$

To model  $P_{\text{max}}$  in the cells used by Babcock *et al.*, we solve Eq. 4.10 with a very high power, broadband (~1000 GHz bandwidth) pump profile, [<sup>3</sup>He]=7.9 amg, the appropriate  $D$  for each cell,  $P_\infty$  as derived in Chapter 3, and our measured K-<sup>3</sup>He cross section. The modeling is described completely in Chapter 6. The results, shown in Fig 4.4, are in good agreement with the high  $D$  data from [Babcock et al., 2003]. Note that without potassium absorption, the model predicts very high maximum alkali-metal polarization even at high  $D$ . This indicates that the K-<sup>3</sup>He and dark state absorptions we have characterized well explain the low alkali polarizations observed in high  $D$  cells. The low  $P_{\text{max}}$  at low  $D$  is still unexplained.

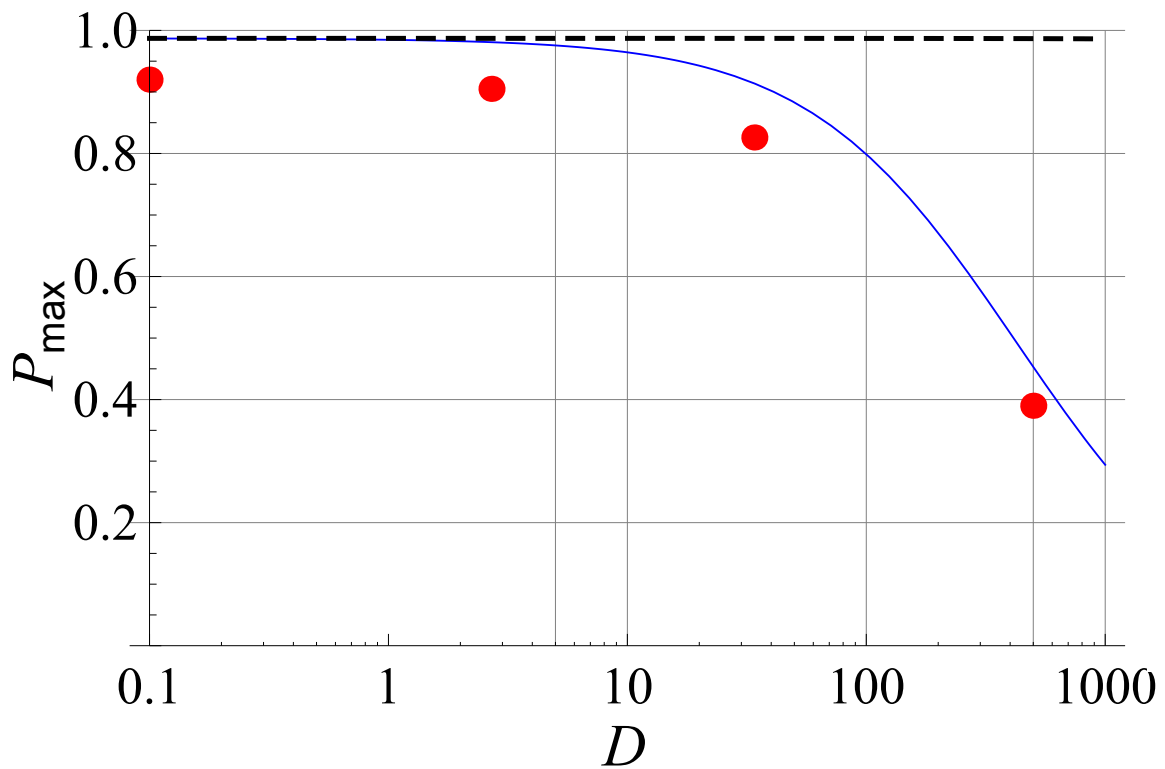


Figure 4.4 Comparison of measured [Babcock et al., 2003] and modeled maximum achievable alkali polarization as a function of K/Rb density ratio  $D$  in a  $[^3\text{He}] = 8.0$  amg hybrid cell pumped by a 1000 GHz bandwidth source. Modeling was done with (solid blue) and without (dashed black) off-resonant potassium absorption.

## Chapter 5

### Excited State Spin Relaxation

#### 5.1 Motivation

An essential but little studied component of any successful SEOP experiment is 10 to 100 Torr of nitrogen gas, provided to inhibit relaxation due to radiation trapping [Walker and Happer, 1997]. For applications such as high-pressure spin-polarized targets at storage rings [Singh et al., 2009, Slifer et al., 2008], it is desirable to minimize the nitrogen content of the gas, as it contributes to scattering backgrounds. In addition, recent work on the supposedly less demanding application of neutron spin filters has shown an unexpectedly large influence of high-flux neutron beams on the spin-exchange process [Sharma et al., 2008, Babcock et al., 2009]. Further investigations suggest that the very high observed alkali relaxation rates when performing SEOP on neutron beams correlate positively with the nitrogen pressure, again giving motivation to use as little nitrogen as necessary. It therefore becomes important to quantify the nitrogen density requirements for SEOP.

This chapter presents an analysis of the optical pumping process under conditions typical of SEOP, in particular, considering the effects of excited-state spin relaxation and hyperfine evolution and of radiation trapping. The bulk of this chapter has been published as [Lancor and Walker, 2010]. Nitrogen gas is a key player in these effects. In addition to quenching, nitrogen is usually the primary source of fine-structure-changing collisions in the excited state and a contributor to excited-state electron spin relaxation [Rotondaro and Perram, 1998] and line broadening [Romalis et al., 1997]. All of these effects would be minor, were it not for excited-state hyperfine couplings that cause relaxation of the alkali nuclear spin while the atom is in the excited state. This effect is usually assumed to be small [Walker and Happer, 1997], but we shall see that, especially for low-He-pressure

applications such as neutron spin filters, nuclear spin nonconservation is significant even at typical  $N_2$  pressures. Especially when this effect is coupled with relaxation from radiation trapping, we find that the photon demands increase rapidly at low nitrogen pressures.

## 5.2 Excited State Nuclear Spin Relaxation

First, we consider the relaxation of alkali-metal nuclear spin in the excited state. During optical pumping, the ground-state hyperfine interaction couples the alkali-metal nuclear and electron spins, polarizing the nuclear spins. In the excited state, collisions with the  $^3\text{He}$  and  $N_2$  buffer gases rapidly relax the alkali-metal electron spins, leaving the nuclear spins unchanged. If there is sufficient time between spin relaxing or quenching collisions, the excited-state hyperfine interaction causes the spin polarized nuclear spins to transfer angular momentum to the randomized electron spins.

We can make an estimate of this effect by considering that there is a mean time  $\tau$  between spin-relaxing collisions in the excited state, and the nuclei precess at a rate  $A$ , where  $A\mathbf{I} \cdot \mathbf{S}$  is the excited-state hyperfine coupling. The amount of nuclear spin lost in a single coherence time is given by first-order time-dependent perturbation theory as  $\delta I_z \approx (2\pi A\tau)^2 I_z$ , or the nuclear spin polarization decays with time at a rate  $(2\pi A)^2 \tau$ . If the time before a nitrogen quenching collision is  $\tau_Q$ , there will be  $\tau_Q/\tau$  coherent precession intervals while in the excited state. Thus we expect to lose a fraction  $f_I \approx 1 - \exp[-(2\pi A)^2 \tau \tau_Q]$  of the nuclear spin in the excited state. At 1 Atm He pressure and 50 Torr  $N_2$  pressure, we can calculate  $\tau$  and  $\tau_Q$  from the collisional cross sections summarized in Table 5.1, giving an estimate  $f_I \approx \{0.06, 0.53\}$  for  $^{85,87}\text{Rb}$ . A significant amount of angular momentum is potentially lost through this effect.

Figure 5.1 shows a more realistic simulation of the total angular momentum as a function of time for atoms that are initially excited to the fully polarized  $m'_F = I + 1/2$  state. The calculation includes collisions with He and  $N_2$ , but no  $N_2$  quenching collisions or spontaneous emission. Results are shown with and without collisional transfer to the  $P_{3/2}$  state [Rotondaro and Perram, 1998], which slows the nuclear spin-relaxation due to significantly reduced hyperfine interaction in that state. The electron spin polarization is very rapidly lost, making  $F_z \approx I$ . Then, as the electron and nucleus precess around each other, the rapid He collisions continue to remove the electronic

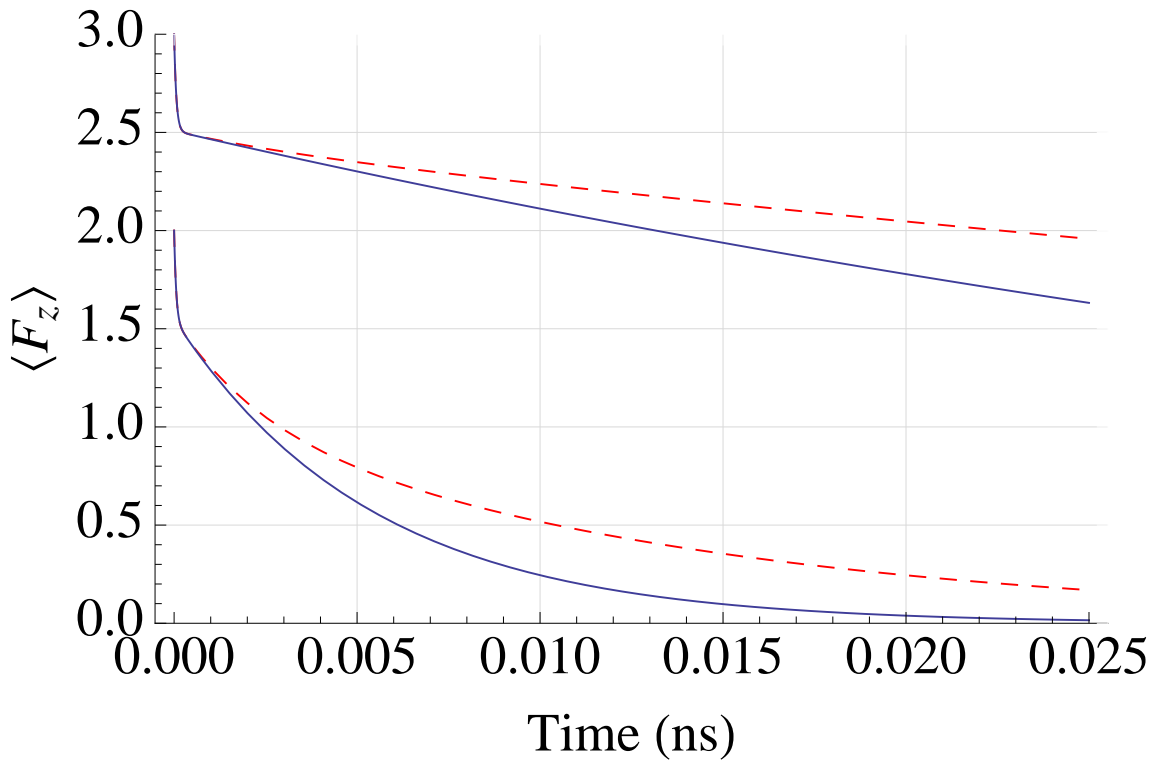


Figure 5.1 Total angular momentum evolution in the excited state, for initially fully polarized  $P_{1/2}$   $^{85}\text{Rb}$  (upper curves) and  $^{87}\text{Rb}$  (lower curves) in 1 amg of He gas and 0.065 amg of  $\text{N}_2$ , assuming no quenching. Collisions rapidly relax the electronic angular momentum to nearly zero, but hyperfine coupling partially repolarizes the electron so that repeated collisions eventually relax the nucleus as well. The substantially smaller hyperfine splitting in  $^{85}\text{Rb}$  makes the effect much smaller in that isotope. The dashed curves include fine-structure changing collisions.

angular momentum. This results in a slow decrease in the total angular momentum. Without  $\text{N}_2$  quenching to shorten the excited-state lifetime below the 27 ns spontaneous decay lifetime, nearly all the angular momentum would be lost from initially polarized  $^{87}\text{Rb}$  atoms.

### 5.3 Effect of Excited State Spin Relaxation on Optical Pumping

It is convenient to parameterize excited state spin relaxation using  $f_I$ , the fraction of the nuclear spin lost in the excited state per excitation. Section 5.5 will detail the calculation used to determine  $f_I$  over a range of  $^3\text{He}$  and  $\text{N}_2$  densities. The results are shown in Fig. 5.2.

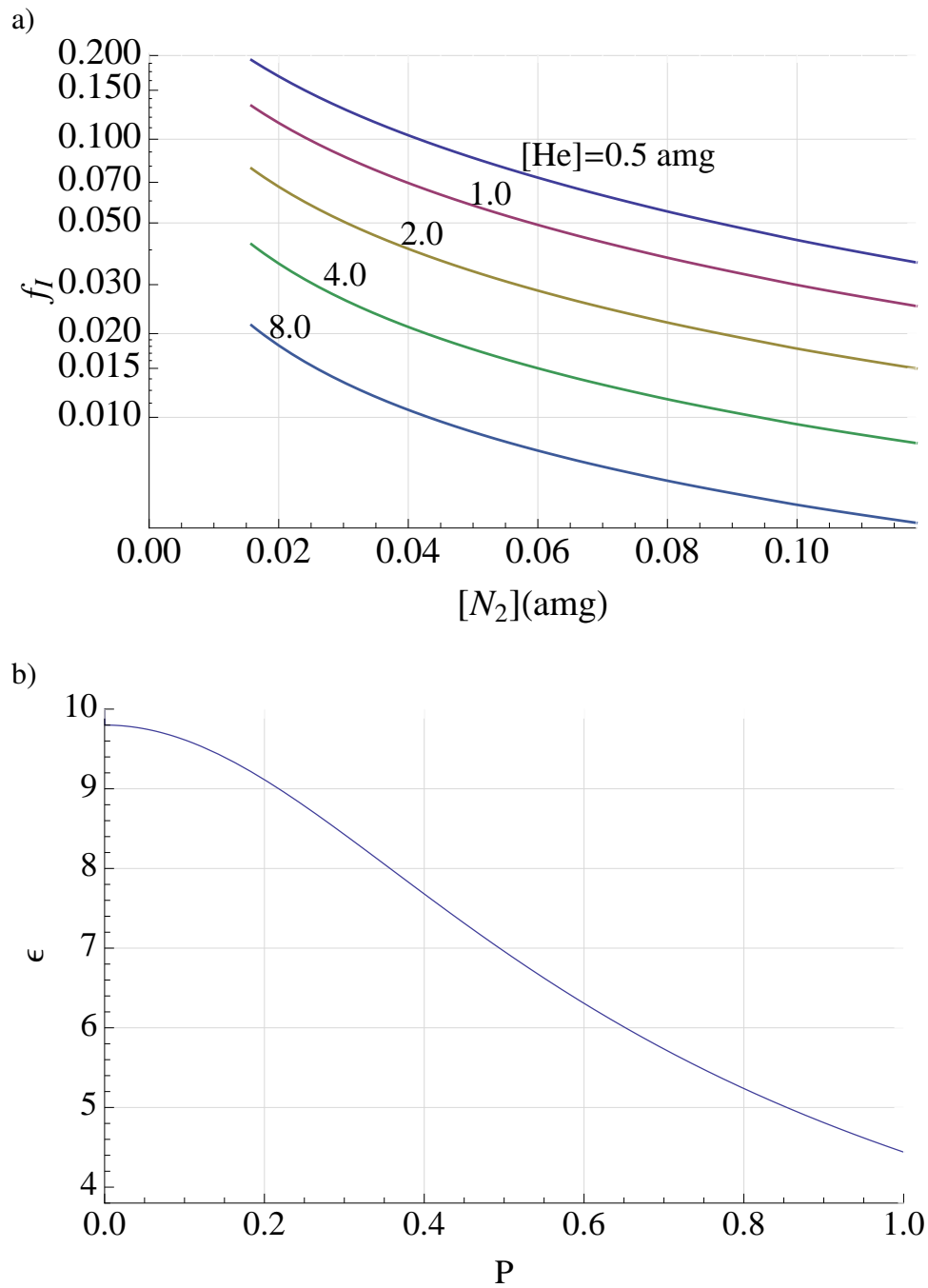


Figure 5.2 a) Calculated fraction of nuclear spin lost in the excited state during the optical pumping cycle,  $f_I$ , at various nitrogen and He densities. b) Paramagnetic coefficient  $\epsilon$  for natural abundance Rb vapor in spin-temperature equilibrium, as a function of electron spin-polarization.

For monochromatic pumping of Rb near the D1 resonance, the evolution of the alkali-metal spin is typically described by

$$\frac{dF_z}{dt} = \frac{1}{2}R_p(1 - P_{\text{Rb}}) - \Gamma_{\text{Rb}}\frac{P_{\text{Rb}}}{2} \quad (5.1)$$

(this assumes  $P_\infty = 1$ , a good assumption very near resonance.) The rate at which atoms are excited is  $R_p(1 - P_{\text{Rb}})$ , so including the loss of a fraction  $f_I$  of the nuclear spin per excitation, we get

$$\frac{dF_z}{dt} = \left(\frac{1}{2} - f_I\langle I_z \rangle\right)R_p(1 - P_{\text{Rb}}) - \Gamma_{\text{Rb}}\frac{P_{\text{Rb}}}{2} \quad (5.2)$$

$$= (1 - f_I\epsilon(P_{\text{Rb}})P_{\text{Rb}})\frac{R_p}{2}(1 - P_{\text{Rb}}) - \Gamma_{\text{Rb}}\frac{P_{\text{Rb}}}{2} \quad (5.3)$$

In spin temperature the nuclear and electron spins are related by the paramagnetic coefficient  $\epsilon(P_{\text{Rb}}) = \langle S_z \rangle / \langle I_z \rangle$ , which varies from  $4I(I + 1)/3$  at low polarizations to  $2I$  at high polarizations. (For a natural mixture of the two Rb isotopes, it ranges from 9.8 at low polarizations to 4.44 at high polarizations.) At high polarizations,  $P \sim 1$ , the excited-state nuclear spin relaxation is effectively a reduction in the optical pumping rate from  $R$  to  $R(1 - f_I\epsilon)$ .

An interesting and important feature of Eq. 5.3 is that if  $f_I\epsilon > 1$ , the atom cannot be fully spin-polarized even at infinitely large pumping rates. The maximum steady-state polarization is  $P_{\text{max}} = \min(1, 1/f_I\epsilon)$ , shown in Fig. 5.3.

The steady-state photon absorption rate is, not too surprisingly, also increased by the excited-state relaxation. The absorption rate or photon demand  $A = R(1 - P_{\text{Rb}})$ , can be found from solving Eq. 5.3 in steady state

$$A = R(1 - P_{\text{Rb}}) = \frac{\Gamma_{\text{sd}}P_{\text{Rb}}}{1 - f_I\epsilon P_{\text{Rb}}} \quad (5.4)$$

Again, as  $f_I\epsilon P$  approaches 1, the absorption rate increases dramatically, as shown in Fig. 5.4.

## 5.4 Radiation Trapping

Due to the extreme optical thickness of SEOP cells, often 100 optical depths, any resonance light emitted in the optical pumping process is re-absorbed before leaving the cell. Since this light

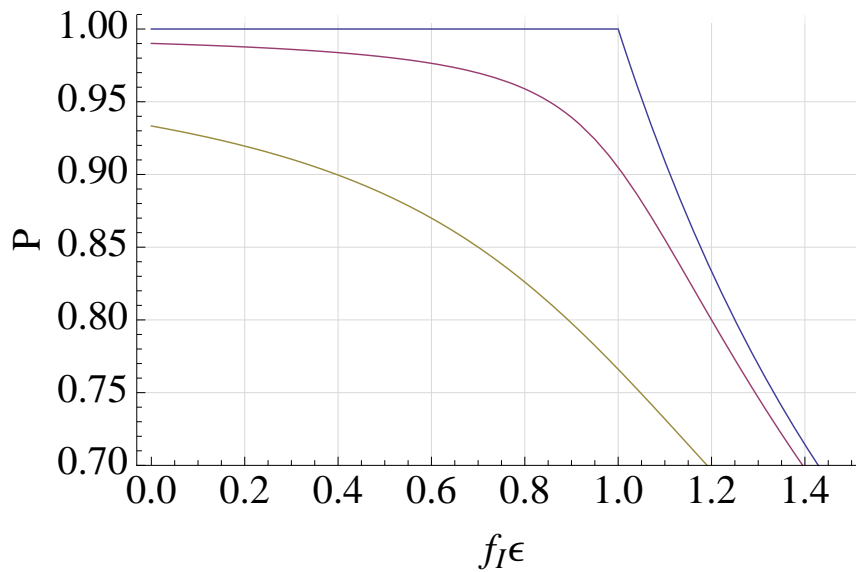


Figure 5.3 The steady-state polarization as a function of the product  $f_I \epsilon$ , which is approximately twice the angular momentum lost by the nucleus during the excited-state evolution. The three curves are, top to bottom, for  $R = \infty$ ,  $R = 100\Gamma_{sd}$ , and  $R = 14\Gamma_{sd}$ .

is nearly unpolarized, it acts as an efficient relaxation agent with the consequence that optically thick cells cannot be polarized without some means of suppressing the relaxation from radiation trapping. One solution, proposed by Peterson and Anderson [Peterson and Anderson, 1991], is to apply a large magnetic field so that the fluorescent light has an emission profile with at least one component that is non-resonant with spin-polarized atoms. This method is very effective for optical pumping of dense, non-pressure-broadened cells and has been in intensive use for decades at polarized ion sources around the world [Anderson, 1979, Levy and Zelenski, 1998]. For spin-exchange optical pumping, the required magnetic fields would be on the order of 1 Tesla, which is impractical.

The second means of circumventing radiation trapping is to collisionally quench any optically excited atoms in a time short compared to the spontaneous lifetime of the excited state [Happer, 1972]. Nitrogen is by far the most convenient molecule for this purpose. It is one of the few molecules that does not chemically react with hot alkali vapor, and it has vibrational excitations that are nearly resonant with the 1.5 eV alkali resonance lines, resulting in very large ( $\sim 50$

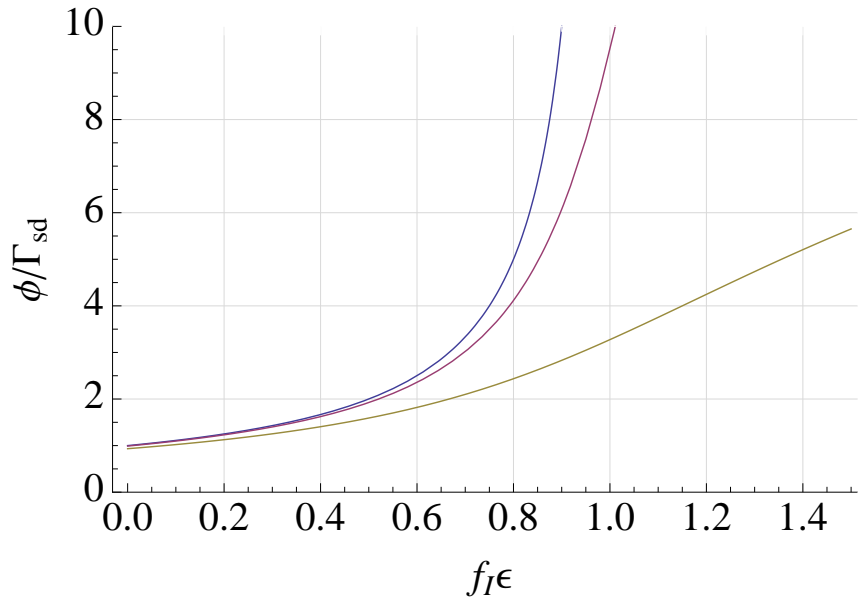


Figure 5.4 The photon demand as a function of the product  $f_I\epsilon$ , normalized to the ground-state spin-relaxation rate  $\Gamma_{sd}$ , the value that would be obtained in the absence of excited-state nuclear spin-precession. The three curves, top to bottom, are for  $R = \infty$ ,  $R = 100\Gamma_{sd}$ , and  $R = 14\Gamma_{sd}$ .

FIX AXIS LABEL

$\text{\AA}^2$ ) quenching cross sections. With tens of Torr of nitrogen pressure, the probability of spontaneous emission can be reduced by a factor of ten or more, allowing the vapor to become optically pumped with only a minor impact on the laser power demand from radiation trapping.

To our knowledge, radiation trapping has not been explicitly treated in models of spin-exchange optical pumping. In general, radiation transport is a highly nonlinear problem. A simple representation of the effects of radiation trapping in the spirit of Eq. 5.3 is given by the following argument. Upon absorption of an unpolarized photon emitted by another atom, the subsequent excited-state evolution causes virtually all the electronic angular momentum and a fraction  $f_I\langle I_z \rangle$  of the nuclear angular momentum to be lost. Thus the total change in angular momentum due to absorption of a radiated photon is  $-(\langle S_z \rangle + f_I\langle I_z \rangle) = -(1 + f_I\epsilon)P/2$ . The radiated photons are emitted at the rate  $R(1 - P)\frac{\Gamma_s}{(\Gamma_s + \Gamma_Q)}$  and must therefore be absorbed by other atoms at that same rate. In terms of the spontaneous emission probability  $f_s = \Gamma_s/(\Gamma_s + \Gamma_Q)$ , the optical pumping rate equation then

becomes

$$\frac{d\langle F_z \rangle}{dt} = \frac{R}{2} (1 - P) (1 - P [f_I' \epsilon + f_s]) \quad (5.5)$$

where

$$f_I' = f_I (1 + f_s). \quad (5.6)$$

The photon demand of Eq. 5.4 becomes

$$A = R(1 - P) = \frac{\Gamma_{sd} P}{1 - [f_I' \epsilon + f_s] P} \quad (5.7)$$

The two terms in square brackets in Eqs. 5.5 and 5.7 correspond to the nuclear spin lost per photon scattered from the pump beam and the electron spin lost due to absorption of spontaneously emitted photons. A more sophisticated calculation is described below, although typically  $f_I$  as calculated using the sophisticated model (Fig. 5.2) can be used with this simpler model to produce sufficiently accurate results, as described in Chapter 6.

## 5.5 Quantitative Optical Pumping Model

We have developed a detailed model of the optical pumping portion of the spin-exchange process using the formalism of Ref. [Happer et al., 2010], hereafter cited as HJW. For the optical pumping simulations we write the density matrix in block form

$$\rho = \begin{bmatrix} \rho^e & \rho^{eg} \\ \rho^{ge} & \rho^g \end{bmatrix} \quad (5.8)$$

where  $\rho^g$ , for example, is the  $g_g \times g_g$  matrix spanning the basis of ground state sub levels. Optical coherences between the ground state and the excited state are stored in the off diagonal blocks. For the conditions of SEOP, pumping rates are small compared to quenching rates due to  $N_2$  collisions. Thus, the quasi-steady-state approximation, where the populations in the ground and excited states are assumed to change slowly compared to the radiative lifetime, can be made. Then, the coherences between the ground and excited states can be related simply to the populations, and need not be considered directly in the simulations; Only the blocks  $\rho^g$  and  $\rho^e$  are needed.

It is beneficial to perform computation in Liouville space, where the density matrix is transformed into a column vector by placing each successive column of the matrix below the one to

its left. The  $g_g \times g_g$  matrix  $\rho^g$  is transformed into a  $g_g^2$  long column vector  $|\rho^g\rangle$ , and  $\rho^e$  becomes a  $g_e^2$  long column vector  $|\rho^e\rangle$ . An operator  $A_p$  in Schrodinger space that connects density matrix blocks  $\rho^i$  and  $\rho^j$  becomes a  $g_i^2 \times g_j^2$  matrix  $A_p^{ij}$  in Liouville space. In the text that follows the vector notation for the transformed density matrix has been dropped. See also Ref. [Appelt et al., 1998] for a similar approach.

### 5.5.1 Atom-light Interaction

We assume circularly polarized optical pumping light of a Gaussian spectral profile and with a bandwidth of 100 GHz, a value now common to many SEOP experiments [Chen et al., 2007]. The full hyperfine structure of the ground  $5S_{1/2}$  and excited  $5P_J$  states are taken into account, and a magnetic field of 5 Gauss is assumed to be applied along the laser propagation direction. Pressure broadening of the resonance lines is taken to be Gaussian, with widths from [Romalis et al., 1997]. The pumping rate  $R_p$  is assumed to be an adjustable parameter. With the large laser linewidth as compared to the hyperfine structure,  $R_p$  is nearly the same for the two Rb isotopes.

### 5.5.2 Excited State Evolution

The excited-state density matrix  $\rho^e$  is sourced by optical excitation, evolves due to hyperfine interactions and collisions with  $^3\text{He}$  and  $\text{N}_2$  atoms (at a rate  $\Gamma_c$ ), and decays via nitrogen quenching and spontaneous emission at rates  $\Gamma_Q$  and  $\Gamma_s$ :

$$\dot{\rho}^e = RA_p^{eg}\rho^g - (iH^{e\odot} + \Gamma_c A^{ee})\rho^e - (\Gamma_s + \Gamma_Q)\rho^e \quad (5.9)$$

Assuming no coherence in the ground-state density matrix  $\rho^g$ , the excitation matrix  $A_p^{eg}$ , HJW (6.35), couples only ground state populations to excited-state populations. The matrix  $H^{e\odot}$ , HJW (5.90), operating on  $\rho^e$  is equivalent to a commutator of  $\rho$  and  $H_0$  in Schrodinger space, describing the free evolution of the atoms.  $H^{e\odot}$  is diagonal in the Liouville representation and contains the Bohr frequencies associated with the excited-state hyperfine structure. Due to fine-structure changing collisions, included in  $A^{ee}$ , both  $P_{1/2}$  and  $P_{3/2}$  evolution are important. The matrix  $A^{ee}$  and the collision rate  $\Gamma_c$  will be discussed further in Sec. 5.5.3.

It is convenient to combine the last two terms in Eq. 5.9 into an excited-state evolution matrix  $G^{ee} = iH^{e\odot} + \Gamma_c A^{ee} + \Gamma_s + \Gamma_Q$ . Then the steady-state solution to Eq. 5.9 is

$$\rho^e = R[G^{ee}]^{-1} A_p^{eg} \rho^g \quad (5.10)$$

### 5.5.3 Excited-state Spin Relaxation

Collisions with  $N_2$  and  $^3\text{He}$  cause excited-state spin-relaxation, including transfer between fine-structure levels. These collisions are assumed to be binary and of sufficiently short duration to conserve nuclear spin. The relaxation is conveniently described by a multipole expansion of  $\rho^e$  [Baylis, 1979], or equivalently by expanding  $A^{ee}$  in terms of multipole projection operators  $\Pi_l^{J'J}$  of HJW Sect. 11.1:

$$A^{ee} = \sum_{lJ'} \alpha_l^{J'J} \Pi_l^{J'J} \quad (5.11)$$

The coefficients with  $J' \neq J, l = 0, 1$  describe fine-structure changing collisions. The coefficients with  $J' = J = 3/2, l = 1, 2, 3$ , describe spin relaxation in the  $P_{3/2}$  state. The coefficient  $\alpha_1^{1/2,1/2}$  represents spin relaxation in the  $P_{1/2}$  state. The multipole relaxation rates  $\Gamma_c \alpha_l^{J'J}$  can be calculated from the cross sections measured by [Rotondaro and Perram, 1998] (Table 5.1). The rates for a gas of density  $[G]$  are  $\Gamma_c \alpha_l^{J'J} = \sigma_l^{J'J} v [G]$ , where  $v = \sqrt{8kT/\pi\mu}$  is the mean thermal velocity for atom pairs of reduced mass  $\mu$  at temperature  $T$ . The quenching rate  $\Gamma_Q = \sigma_Q v [N_2]$ .

While the fine-structure-changing and multipole relaxation processes conserve nuclear spin, they produce coherences between the different excited-state hyperfine levels. The subsequent precession of these hyperfine coherences results in loss of angular momentum from the Rb nuclei.

### 5.5.4 Optical Pumping

We now consider how optical pumping of the ground-state is affected by the excited-state spin-precession. There are two contributions to the optical pumping. Depopulation pumping removes atoms from the ground state, while repopulation pumping replenishes the ground state from the excited-state either by quenching or spontaneous emission.

Multipole process ( $5P_J \rightarrow 5P_{J'}$ )	l=0	1	2	3
$5P_{3/2} + \text{He} \rightarrow 5P_{3/2} + \text{He}$		240	280	200
$5P_{3/2} + \text{N}_2 \rightarrow 5P_{3/2} + \text{N}_2$		214	283	266
$5P_{1/2} + \text{He} \rightarrow 5P_{1/2} + \text{He}$		32		
$5P_{1/2} + \text{N}_2 \rightarrow 5P_{1/2} + \text{N}_2$		65		
$5P_{1/2} + \text{He} \rightarrow 5P_{3/2} + \text{He}$	0.072	0*		
$5P_{1/2} + \text{N}_2 \rightarrow 5P_{3/2} + \text{N}_2$	10.1	-0.3		

Quenching	$\sigma_Q$
$5P_{3/2} + \text{N}_2 \rightarrow 5S_{1/2} + \text{N}_2$	43
$5P_{1/2} + \text{N}_2 \rightarrow 5S_{1/2} + \text{N}_2$	58

Table 5.1 (top) Multipole relaxation cross sections  $\sigma_l^{J'J}$  (in  $\text{\AA}^2$ ), adapted from Ref. [Rotondaro and Perram, 1998]. The asterisk denotes an assumed quantity. The multipole relaxation rates for a gas of density  $[G]$  are  $\Gamma_c \alpha_l^{J'J} = \sigma_l^{J'J} v [G]$ , where  $v = \sqrt{8kT/\pi\mu}$  is the mean thermal velocity for atom pairs of reduced mass  $\mu$  at temperature  $T$ . (bottom) Quenching rates  $\Gamma_Q = \sigma_Q v [\text{N}_2]$ .

This repopulation pumping obeys

$$\dot{\rho}_{\text{RP}}^g = (\Gamma_s A_s^{ge} + \Gamma_Q A_Q^{ge}) \rho^e = G^{ge} \rho^e \quad (5.12)$$

The spontaneous emission matrix  $A_s^{ge}$  is given by HJW (5.50), while the quenching matrix is

$$A_Q^{ge} = \sum_J \Pi_0^{SJ} \quad (5.13)$$

We are assuming that the quenching process fully transfers nuclear polarization from the excited state to the ground state, with no transfer of electronic polarization. The depopulation pumping obeys

$$\dot{\rho}_{\text{DP}}^g = -R A_p^{gg} \rho^g \quad (5.14)$$

The net evolution from optical pumping is the sum of the depopulation and repopulation pumping terms.

$$\dot{\rho}_{\text{OP}}^g = -RA_{\text{p}}^{gg}\rho^g + G^{ge}\rho^e \quad (5.15)$$

Using Eq. 5.10 for  $\rho^e$ , this becomes

$$\dot{\rho}_{\text{OP}}^g = -RA_{\text{p}}^{gg}\rho^g + RG^{ge}[G^{ee}]^{-1}A_{\text{p}}^{eg}\rho^g \quad (5.16)$$

$$= -RA_{\text{OP}}\rho^g \quad (5.17)$$

Under typical pumping conditions, no Zeeman or hyperfine coherences are generated, so we assume that the ground state density matrix is well represented by populations alone, so that evolution due to light shifts and ground-state hyperfine interactions are not necessary to include in Eq. 5.17.

### 5.5.5 Ground-state Spin-Randomization

There are a variety of important ground-state spin-relaxation mechanisms at work in spin-exchange optical pumping. The most important, spin-exchange collisions between the alkali-metal atoms, conserves the total angular momentum and produces a spin-temperature distribution. These will be treated in Sec. 5.5.6.

Depending on conditions, the most important relaxation mechanisms that do not conserve the total angular momentum are typically electron randomization due to the spin-rotation interaction in Rb-He and Rb-N<sub>2</sub> collisions [Ben-Amar Baranga et al., 1998], electron randomization due to the spin-axis interaction in Rb-Rb collisions [Kadlecek et al., 2001], and the formation of Rb<sub>2</sub> molecules [Kadlecek et al., 1998, Erickson et al., 2000]. We lump them together into an effective electron randomization rate  $\Gamma_{\text{sd}}$  and simply represent the ground-state relaxation as

$$\dot{\rho}_{\text{SR}}^g = -\Gamma_{\text{sd}}A_{\text{sd}}^{gg}\rho^g \quad (5.18)$$

where the spin-damping matrix  $A_{\text{sd}}^{gg}$  is given in HJW 6.88. Combining the optical pumping and spin randomization gives

$$\dot{\rho}^g = -G^{gg}\rho^g \quad (5.19)$$

$$G^{gg} = RA_{\text{OP}} + \Gamma_{\text{sd}}A_{\text{sd}}^{gg} \quad (5.20)$$

for the ground-state density matrix evolution.

### 5.5.6 Rb-Rb Spin-Exchange

Spin-exchange collisions between Rb atoms conserve the total angular momentum, but redistribute the spin and nuclear Zeeman populations toward a spin-temperature distribution [Happer, 1972, Happer et al., 2010]

$$\rho_{\text{ST}}(P) = Z(P)^{-1} e^{-\beta(P)F_z} \quad (5.21)$$

where the spin-temperature parameter  $\beta$  is determined by the Rb electron spin polarization  $P$  via  $P = \tanh(\beta/2)$ , and  $Z$  is a normalizing factor. At the high Rb densities used in spin-exchange experiments, the Rb-Rb spin-exchange rates dominate any of the other rates in the system and so the ground-state density matrix should be well described by a spin-temperature distribution.

To this point, the two isotopes were treated separately. The rapid spin-exchange collisions directly couple the two isotopes, so their density matrices are not independent; the electron spin-polarizations are equal. In the spin-temperature limit, the simplest way to treat the spin-exchange effects is to consider the isotopic fraction weighted total angular momentum

$$\langle F_z \rangle = \sum_i \eta_i \langle F_{zi} \rangle \quad (5.22)$$

where  $\eta_i$  is the isotopic abundance of isotope  $i$ . (In the following, analogous isotope subscripts will be added to various quantities as needed.) Then the rate equation for  $\langle F_z \rangle$  is

$$\left\langle \dot{F}_z \right\rangle = - \sum_i \eta_i \text{Tr}[F_{zi} G_i^{gg} \rho_{i,\text{ST}}^g(P)] \quad (5.23)$$

Eq. 5.23 is a non-linear equation, as  $\langle F_z \rangle$  and  $P$  are non-linearly related, but it is easy to find the steady state solution by varying  $P$  until Eq. 5.23 is zero.

Having found  $P$  and the absorption rate  $A = R \text{Tr}(A_p^{gg} \rho^g)$ , we calculate  $\epsilon$  and rearrange Eq. 5.4 to solve for

$$f_I = \frac{R - (R + \Gamma_{\text{sd}})P}{\epsilon A} \quad (5.24)$$

where  $R$  is the isotopically averaged pumping rate.

The parameterization  $f_I$  is only useful if it is relatively insensitive to the polarization. Indeed, we find that it generally decreases by 10% or less as the polarization is decreased (by decreasing the pumping rate in the model) to values well below 50%. The results in Fig. 5.2 were calculated at a pumping rate of  $R = 14\Gamma_{\text{sd}}$ .

### 5.5.7 Radiation Trapping

Since the line-center optical thickness of most SEOP cells is on the order of 100, to a good approximation photons emitted in the line core will be reabsorbed before leaving the cell. These photons, which are essentially unpolarized, will therefore be absorbed by nearby atoms and they will act as an additional spin-relaxation mechanism. In the limit that the quenching is rapid compared to spontaneous decay, the probability of the absorption of a photon from the optical pumping laser resulting in more than one re-emitted photon is very small. Thus since photons are being spontaneously emitted at a rate  $R_s = \text{Tr}[\Gamma_s \rho^e]$ , on average the absorption rate of the unpolarized emission photons must be the same.

We therefore approximately model the effects of radiation trapping by

$$\dot{\rho}_{\text{RT}}^g = -R_s(1 - G^{ge}[G^{ee}]^{-1}A_{\text{RT}}^{eg})\rho^g = -R_s G_{\text{RT}}\rho^g \quad (5.25)$$

where the matrix  $A_{\text{RT}}^{eg}$  is generated in the same manner as the spontaneous decay matrix  $A_s^{ge}$ , only with the roles of excited and ground states reversed. Thus in the notation of HJW

$$A_{\text{RT}}^{eg} = \frac{2}{3} \sum_{J_j} f_J \Delta_j^T \otimes \Delta_j^\dagger \quad (5.26)$$

where  $f_J$  is the fraction of light emitted by atoms in the excited state with angular momentum  $J$ .

Thus we find the steady-state solution for our full optical pumping model by solving

$$0 = \sum_i \eta_i \text{Tr}[F_z(G_i^{gg} + R_s G_{i,\text{RT}})\rho_{i,\text{ST}}^g(P)] \quad (5.27)$$

Since  $R_s$  depends on  $P$ , it is necessary to iterate a few times to obtain a consistent solution.

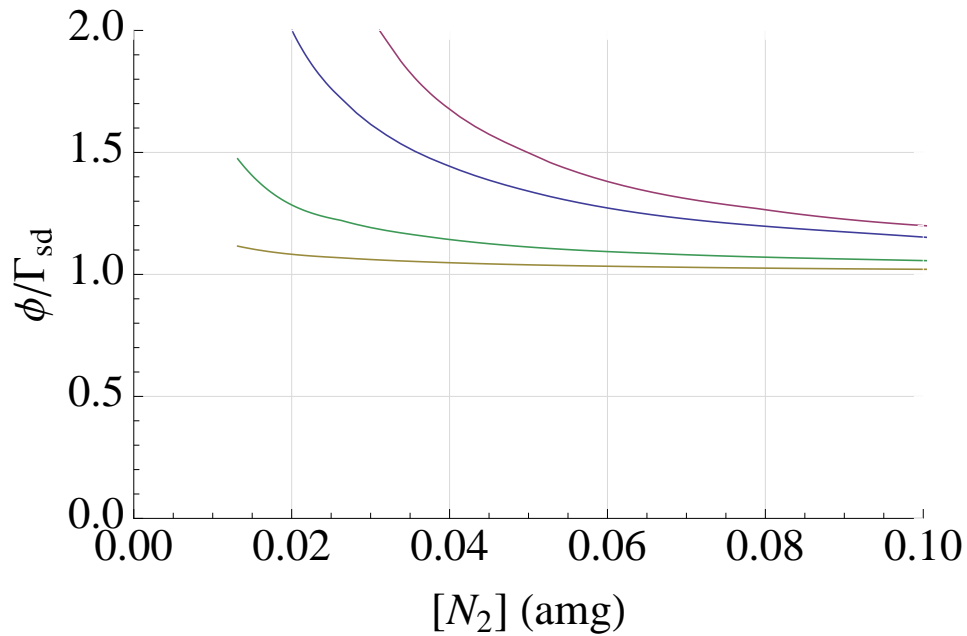


Figure 5.5 The photon demand normalized to its ideal value. The upper two curves are for 1 amg He density, the lower two for 8 amg. The upper curve of each pair includes both radiation trapping and excited-state relaxation effects, while the lower includes only excited-state relaxation.

## 5.6 Discussion and Conclusions

A convenient figure of merit for evaluating these effects is the ratio of the photon demand  $A$  to the ground-state relaxation rate  $\Gamma_{sd}$ ; at high Rb polarization this ratio would be unity in the absence of excited-state nuclear relaxation and radiation trapping. Fig. 5.5 shows the calculated photon demand as a function of  $N_2$  density, with and without radiation trapping, for two different representative He densities.

At high pressures we see that radiation trapping is somewhat more important than excited-state hyperfine precession, but the total effect is less than 10% with 0.05 amg or more of nitrogen. At 1 amg densities, however, the excess photon demands can become quite serious if insufficient nitrogen is present. The photon demands doubles below 0.03 amg and is still about 20% larger than the ideal value at 0.1 amg.

While we have concentrated in this discussion on the importance of nitrogen for suppressing excess relaxation from hyperfine precession and radiation trapping, there are at least four

other important considerations for spin-exchange optical pumping that concern the nitrogen density and we mention them here for completeness. First, the energy stored in the vibrational degrees of freedom of the  $N_2$  following quenching collisions is dissipated by collisions with the He [Walter et al., 2001]. This produces heating of the gas to temperatures that may exceed that of the wall by more than  $100^\circ\text{C}$ . Since Rb-He spin-relaxation is strongly temperature dependent [Ben-Amar Baranga et al., 1998], this effect should be taken into account when considering the actual photon demand.

The second additional effect is spin-relaxation in ground-state Rb- $N_2$  collisions which, though usually a small contributor to  $\Gamma_{sd}$ , come into play if the  $N_2$  fraction becomes too large [Ben-Amar Baranga et al., Chen et al., 2007]. Generally one wishes to work at  $N_2$  densities small enough that the  $N_2$  contribution to spin-relaxation is a small effect. Third, we note that  $N_2$  also is a contributor to pressure broadening.

Finally, Chapter 2 describes the experiment that demonstrated that He and  $N_2$  collisions allow fully polarized Rb atoms to absorb resonant circularly polarized D1 light [Lancor et al., 2010b, Lancor et al., 2010a], an effect forbidden for free atoms. This effect also has important consequences for the photon budget in spin-exchange optical pumping. All of these effects are combined in the modeling described in the next chapter.

## Chapter 6

### Modeling

#### 6.1 Overview

We now describe a model of SEOP that includes the effects of dark state absorption, excited state relaxation, radiation trapping, and K-<sup>3</sup>He absorption, as described in previous chapters. The model takes in experimental parameters: Cell size, gas composition, temperature, hybrid ratio  $D$ , and pump laser power and spectral composition. This information is plugged into an equation for the evolution of the atomic spins, which is solved in steady state to find the alkali-metal spin polarization. (A spin temperature distribution is assumed.) The polarization is used to compute the attenuation of the pump beam as it travels a small distance through the cell. Then, the spin polarization is solved for again, with the attenuated pump light. This process is iterated, producing lists of the spin polarization and pump profile as a function of position in the cell. The equation for the evolution of the spins contains some or all of the following terms.

#### 6.2 Optical Pumping

For an  $\lambda = 1$  circularly polarized pump beam, ignoring dark state absorption, the cross section for absorption by spin-down atoms is  $2\sigma_0(\nu - \nu_1)$ , where  $\sigma_0(\nu - \nu_1)$  is the cross section for absorption of unpolarized light, centered at the D1 resonance frequency  $\nu_1$ . Assuming no dark state absorption, atoms in the spin-up ground state have zero cross section for absorption. Our modeling includes the ground state hyperfine splittings of <sup>85</sup>Rb and <sup>87</sup>Rb, so there are different center frequencies for absorption out of each hyperfine manifold. The total absorption rate is calculated as the sum of absorption out of each hyperfine sub level. Each sublevel is composed of

one spin-up and one spin-down state in the fine structure basis, where the squares of the Clebsch-Gordan coefficients  $C_{m_J m_I}^{F m_f} = \langle F m_f | J m_J I m_I \rangle$  give the probability that an atom in each sub-level will be measured to have electron spin  $m_J$ . Atoms are excited only from the  $m_J = -1/2$  state, so the absorption rate is given by

$$A = .72 \left( \sum_{F=2}^3 \sum_{m_f=-F}^F \rho_{F m_f} |C_{-1/2(m_f+1/2)}^{F m_f}|^2 \int_0^\infty 2\phi(\nu) \sigma_0(\nu - \nu_1^{85,F}) d\nu \right) + .28 \left( \sum_{F=1}^2 \sum_{m_f=-F}^F \rho_{F m_f} |C_{-1/2(m_f+1/2)}^{F m_f}|^2 \int_0^\infty 2\phi(\nu) \sigma_0(\nu - \nu_1^{87,F}) d\nu \right) \quad (6.1)$$

where the sublevel populations  $\rho_{F m_F}$  are related to  $P_A$  through spin temperature (Appendix C),  $\phi(\nu)$  is the photon flux of the pump laser, and, for example,  $\nu_1^{85,3}$  is the resonance frequency of the  $F = 3$  manifold of  $^{85}\text{Rb}$ . It is assumed that decay from the excited state will repopulate  $m_J = \pm 1/2$  states with equal probability, so on average  $+1/2$  units of angular momentum are gained per excitation. So

$$\left( \frac{dF_z}{dt} \right)_P = \frac{1}{2} A = \frac{1}{2} \left( 72 \left( \sum_{F=2}^3 \sum_{m_f=-F}^F \rho_{F m_f} |C_{-1/2(m_f+1/2)}^{F m_f}|^2 \int_0^\infty 2\phi(\nu) \sigma_0(\nu - \nu_1^{85,F}) d\nu \right) + .28 \left( \sum_{F=1}^2 \sum_{m_f=-F}^F \rho_{F m_f} |C_{-1/2(m_f+1/2)}^{F m_f}|^2 \int_0^\infty 2\phi(\nu) \sigma_0(\nu - \nu_1^{87,F}) d\nu \right) \right) \quad (6.2)$$

### 6.3 Dark State Absorption

When dark state absorption is included, the absorption cross sections for  $\delta = 1$  pump light by the atoms with  $m_J = \pm 1$  become

$$\sigma_{\pm 1}^1(\nu) = \sigma_0(\nu) (1 \mp P_\infty(\nu)) \quad (6.3)$$

Thus, the absorption rate must include terms for both the  $m_J = \pm 1/2$  components of each hyperfine sublevel

$$A_{down} = .72 \left( \sum_{F=2}^3 \sum_{m_f=-F}^F \rho_{Fm_f} |C_{-1/2(m_f+1/2)}^{Fm_f}|^2 \int_0^\infty \phi(\nu) \sigma_0(\nu - \nu_1^{85,F}) (1 + P_\infty(\nu)) d\nu \right) \\ + .28 \left( \sum_{F=1}^2 \sum_{m_f=-F}^F \rho_{Fm_f} |C_{-1/2(m_f+1/2)}^{Fm_f}|^2 \int_0^\infty \phi(\nu) \sigma_0(\nu - \nu_1^{87,F}) (1 + P_\infty(\nu)) d\nu \right) \quad (6.4)$$

$$A_{up} = .72 \left( \sum_{F=2}^3 \sum_{m_f=-F}^F \rho_{Fm_f} |C_{1/2(m_f-1/2)}^{Fm_f}|^2 \int_0^\infty \phi(\nu) \sigma_0(\nu - \nu_1^{85,F}) (1 - P_\infty(\nu)) d\nu \right) \\ + .28 \left( \sum_{F=1}^2 \sum_{m_f=-F}^F \rho_{Fm_f} |C_{1/2(m_f-1/2)}^{Fm_f}|^2 \int_0^\infty \phi(\nu) \sigma_0(\nu - \nu_1^{87,F}) (1 - P_\infty(\nu)) d\nu \right) \quad (6.5)$$

and the evolution of the atomic spins due to pumping becomes

$$\left( \frac{dF_z}{dt} \right)_P = \frac{1}{2} A_{down} - \frac{1}{2} A_{up} \quad (6.6)$$

## 6.4 Ground State Spin Relaxation

Formulas for the relaxation rates for Rb and K in ground state collisions are taken from [Chen et al., 2007], and converted for [ $^3\text{He}$ ] and [ $\text{N}_2$ ] given in amagats, and [Rb] in  $\text{cm}^{-3}$ . For Rb, we use

$$\Gamma_{\text{Rb-Rb}} = 4.2 \times 10^{-13} [\text{Rb}] \text{ s}^{-1} \quad (6.7)$$

$$\Gamma_{\text{Rb-}^3\text{He}} = 66.4 [\text{He}] \left( \frac{T}{473} \right)^{4.259} \text{ s}^{-1} \quad (6.8)$$

$$\Gamma_{\text{Rb-N}_2} = 300 [\text{N}_2] \left( \frac{T}{473} \right)^3 \text{ s}^{-1} \quad (6.9)$$

The values of  $\Gamma_{\text{Rb-Rb}}$  and  $\Gamma_{\text{Rb-}^3\text{He}}$  were taken from measurements in [Ben-Amar Baranga et al., 1998], and  $\Gamma_{\text{Rb-N}_2}$  was derived from a measurement at 480K by [Kadlecek, 2000], with an assumed  $T^3$  scaling. Then,  $\Gamma_{\text{Rb}} = \Gamma_{\text{Rb-Rb}} + \Gamma_{\text{Rb-}^3\text{He}} + \Gamma_{\text{Rb-N}_2}$ , and

$$\left( \frac{dF_z}{dt} \right)_{\Gamma_{\text{Rb}}} = -\Gamma_{\text{Rb}} S_z \quad (6.10)$$

For Potassium

$$\Gamma_{K-K} = 9.6 \times 10^{-14}[\text{K}] \text{ s}^{-1} \quad (6.11)$$

$$\Gamma_{K-^3\text{He}} = (5.5 \times 10^{-20} + 5.8 \times 10^{-31}T^{4.259})[\text{He}]2.51 \times 10^{19} \text{ s}^{-1} \quad (6.12)$$

$$\Gamma_{K-\text{N}_2} = 1.76 \times 10^{-6}T^3[\text{N}_2] \text{ s}^{-1} \quad (6.13)$$

The rates for  $\Gamma_{K-K}$  and  $\Gamma_{K-\text{N}_2}$  are from [Kadlecek, 2000], again with an assumed  $T^3$  scaling for  $\Gamma_{K-\text{N}_2}$ .  $\Gamma_{K-^3\text{He}}$  has a spin-rotation and a spin-exchange component. The spin rotation was measured for  $\text{K-}^4\text{He}$  by [Walker et al., ] at 423K, scaled for the lower reduced mass of  $\text{K}^3\text{He}$ , and given the same  $T^{4.259}$  dependance as spin rotation of  $\text{Rb-}^3\text{He}$ . The  $\text{K-}^3\text{He}$  spin exchange coefficient is from [Babcock, 2005]. Given  $\Gamma_K = \Gamma_{K-K} + \Gamma_{K-^3\text{He}} + \Gamma_{K-\text{N}_2}$

$$\left( \frac{dF_z}{dt} \right)_{\Gamma_K} = -\Gamma_K S_z \quad (6.14)$$

The K-Rb rate coefficient  $q_{KRb}$  is estimated as  $2 \times 10^{-13}$ , the average of the K-K and Rb-Rb rate coefficients.

## 6.5 Wall Relaxation

Wall relaxation is handled in the approximate way suggested in [Walker and Happer, 1997].

We define a diffusion length

$$l_D = \sqrt{\frac{4}{3} \frac{7.5}{\gamma_{\text{Rb}}} \frac{1}{\Gamma_{\text{Rb}} + R_p} \left( .72\sqrt{6} + .28\sqrt{4} \right)} \quad (6.15)$$

where  $\gamma_{\text{Rb}}$  is the Rb D1 absorption linewidth in GHz. At each position  $z$  in the cell,  $P'_A$  is computed as the steady state solution for the differential equation for the alkali-metal spins. Then we include the wall layer by computing

$$P_A = P'_A * \left( 1 - e^{-\frac{z}{l_D}} \right) \left( 1 - e^{-\frac{z-l}{l_D}} \right) \quad (6.16)$$

where  $l$  is the length of the cell,  $\left( 1 - e^{-\frac{z}{l_D}} \right)$  characterizes the reduction in  $P_A$  due to collisions with the front wall of the cell, and  $\left( 1 - e^{-\frac{z-l}{l_D}} \right)$  characterizes the reduction in  $P_A$  due to collisions with the back wall of the cell.

## 6.6 Excited State Relaxation

Excited state spin relaxation is characterized by the parameter  $f_I$ , the fraction of nuclear spin lost per excitation. This can be determined from fig. 5.2, given  $[^3\text{He}]$  and  $[\text{N}_2]$ . Then the contribution to the evolution of the spins is simply the rate of excitation times the fraction of the nuclear spin lost per excitation, times the average nuclear spin. This is

$$\left(\frac{dF_z}{dt}\right)_{ESR} = (A_{up} + A_{down})f_I\langle I_z \rangle = (A_{up} + A_{down})f_I\epsilon(S_z)S_z \quad (6.17)$$

where the paramagnetic coefficient  $\epsilon(S_z)$  relates  $I_z$  to  $S_z$  in spin temperature.

## 6.7 Radiation Trapping

Radiation trapping is characterized, in the way described in Chapter 5, by the parameter  $f_s$ , the fraction of decay through spontaneous emission. This depends on the temperature and nitrogen density, through the quenching rate  $\Gamma_Q$ . From [Rotondaro and Perram, 1998],  $\Gamma_Q = v\sigma_Q[\text{N}_2]$ , where  $\sigma_Q = 50\text{\AA}$  and  $v = \sqrt{8kT/\pi\mu}$  is the mean thermal velocity for atom pairs of reduced mass  $\mu$  at temperature  $T$ . Then, given the 27ns spontaneous decay time of the excited state, we can calculate  $f_s = \frac{\Gamma_s}{\Gamma_Q + \Gamma_s}$ . Since  $[\text{Rb}]$  is typically very high, we assume every spontaneously emitted photon is reabsorbed. The emitted photons have random polarization, so they are absorbed at the same rate by all ground state atoms. In the excited state the atoms lose another fraction  $f_I$  of their nuclear spin and decay into both spin up and spin down ground states with equal probability. Thus, per decay through spontaneous emission, angular momentum  $\frac{1}{2}S_z + f_I\epsilon(S_z)S_z$  is lost from the atoms. Because  $f_s$  is small, and to simplify the analysis, we assume that no atoms excited by the absorption of a spontaneously emitted photon spontaneously emit another photon. So a term

$$\left(\frac{dF_z}{dt}\right)_{RT} = -\frac{\Gamma_s}{\Gamma_Q + \Gamma_s}(A_{up} + A_{down})\left(\frac{1}{2}S_z + f_I\epsilon(S_z)S_z\right) \quad (6.18)$$

can be added to account approximately for the evolution of the spins due to radiation trapping .

## 6.8 Potassium-Helium Absorption

Chapter 4 describes the experiment in which we measured the cross-section for absorption by K atoms near 795nm due to K-<sup>3</sup>He and K-N<sub>2</sub> collisions

$$\sigma_{K-He} = 2.19 \pm .39 \times 10^{-18} \frac{\text{cm}^2}{\text{amg}} [\text{He}] \quad (6.19)$$

and

$$\sigma_{K-N_2} = 8.8 \pm 7.6 \times 10^{-18} \frac{\text{cm}^2}{\text{amg}} [\text{N}_2] \quad (6.20)$$

We assume that this absorption, which is detuned by nearly the same amount from both the  $J = 1/2$  and  $J = 3/2$  potassium excited states, has the same cross-section for both potassium ground states.

Thus, it acts like a spin relaxation mechanism

$$\left( \frac{dF_z}{dt} \right)_{K-^3He} = - \left( \int_0^\infty \phi(\nu) ([^3\text{He}] \sigma_{K-He} + [\text{N}_2] \sigma_{K-N_2}) d\nu \right) S_z = -R_K S_z \quad (6.21)$$

## 6.9 Hybrid SEOP

For simulation of hybrid pumping, the density ratio is used to calculate the molar fractions of Rb and K, by

$$m_{Rb} = \left( \frac{D}{.16} + 1 \right)^{-1} \quad (6.22)$$

and  $m_K = 1 - m_{Rb}$ . This effectively assumes that the input  $D$  is correct at  $T=195^\circ\text{C}$ . Then, the densities [Rb] and [K] are calculated by multiplying the molar fractions by the densities predicted by the vapor pressure curves (Appendix B) at the chosen  $T$ . Then, we write an equation for the evolution of the total angular momentum,  $[\text{Rb}] \left( \frac{dF_z}{dt} \right)_{Rb} + [\text{K}] \left( \frac{dF_z}{dt} \right)_K$ , weighting terms by the density of the associated alkali species

$$\begin{aligned} [\text{Rb}] \left( \frac{dF_z}{dt} \right)_{Rb} + [\text{K}] \left( \frac{dF_z}{dt} \right)_K &= [\text{Rb}] \left[ \left( \frac{dF_z}{dt} \right)_P + \left( \frac{dF_z}{dt} \right)_{ESR} + \left( \frac{dF_z}{dt} \right)_{RT} + \left( \frac{dF_z}{dt} \right)_{\Gamma_{Rb}} \right] \\ &+ [\text{K}] \left[ \left( \frac{dF_z}{dt} \right)_{\Gamma_K} + \left( \frac{dF_z}{dt} \right)_{K-^3He} \right] + [\text{K}][\text{Rb}] q_{KRb} S_z \quad (6.23) \end{aligned}$$

There is also a modification to the diffusion length in Eq. 6.15. In Eq. 6.15,  $(\Gamma_{Rb} + R_p)$  describes the rate at which Rb atoms undergo spin changing collisions and photon absorptions. This, in part,

determines how far from the cell walls atoms move before their spins are brought into equilibrium with average spin in the bulk of the cell. For hybrid cells,  $(\Gamma_{Rb} + R_p)$  is replaced with the normalized rate of spin resetting events per alkali-metal atom  $\frac{([Rb](\Gamma_{Rb} + R_p) + [K]\Gamma_K)}{[K] + [Rb]}$ . This results in a diffusion length

$$l_D = \sqrt{\frac{4}{3} \frac{7.5}{\gamma_{Rb}} \frac{[K] + [Rb]}{[Rb](\Gamma_{Rb} + R_p) + [K]\Gamma_K}} (.72\sqrt{6} + .28\sqrt{4}) \quad (6.24)$$

## 6.10 Efficiencies

We can now use these simulations to assess whether the angular momentum loss processes described in the last three chapters can explain the poor photon efficiencies measured by [Babcock et al., 2003]. As discussed in chapter 1, the photon efficiency is the fraction of the angular momentum transferred by the pump laser to the Rb vapor that goes into polarizing  $^3\text{He}$ , at low  $P_{He}$ .

$$\eta_\gamma = \frac{[^3He] V (dP_{He}/dt)_{P_{He}=0}}{\Delta \phi} \quad (6.25)$$

So,  $\eta_\gamma$  is a measure of the functional efficiency of a SEOP experiment. If ground state collisions accounted for all the alkali-metal spin loss, then  $\eta_\gamma$  should equal the spin exchange efficiency

$$\eta_{SE} = \frac{[^3He](k_{SE}^{Rb-He}[Rb] + k_{SE}^{K-He}[K])}{[Rb]\Gamma_{Rb} + [K]\Gamma_K + [Rb][K]q_{KRb}} \quad (6.26)$$

The spin exchange efficiency is the ratio of the rate of angular momentum transfer to unpolarized  $^3\text{He}$  atoms to the rate of alkali-metal angular momentum lost to ground state collisions. This is a fundamental limit on the fraction of angular momentum deposited in the vapor through photon absorption that can go toward polarizing  $^3\text{He}$  nuclei, based on the characteristics of alkali-metal-buffer gas and alkali-metal-alkali-metal collisions.

In the experiment, Babcock *et al.* measured photon efficiencies factors of 5 to 10 lower than spin exchange efficiencies in  $[^3\text{He}]=8$  amg cells pumped with an un-narrowed diode array bar. Figure 6.1 shows their results, along with a model that includes all of the terms we have discussed. For the modeling, we used the measured frequency spectrum shown in Fig. 3.14, (this is from an unnarrowed diode array bar, but not the one used in the experiment), and the pump power was set

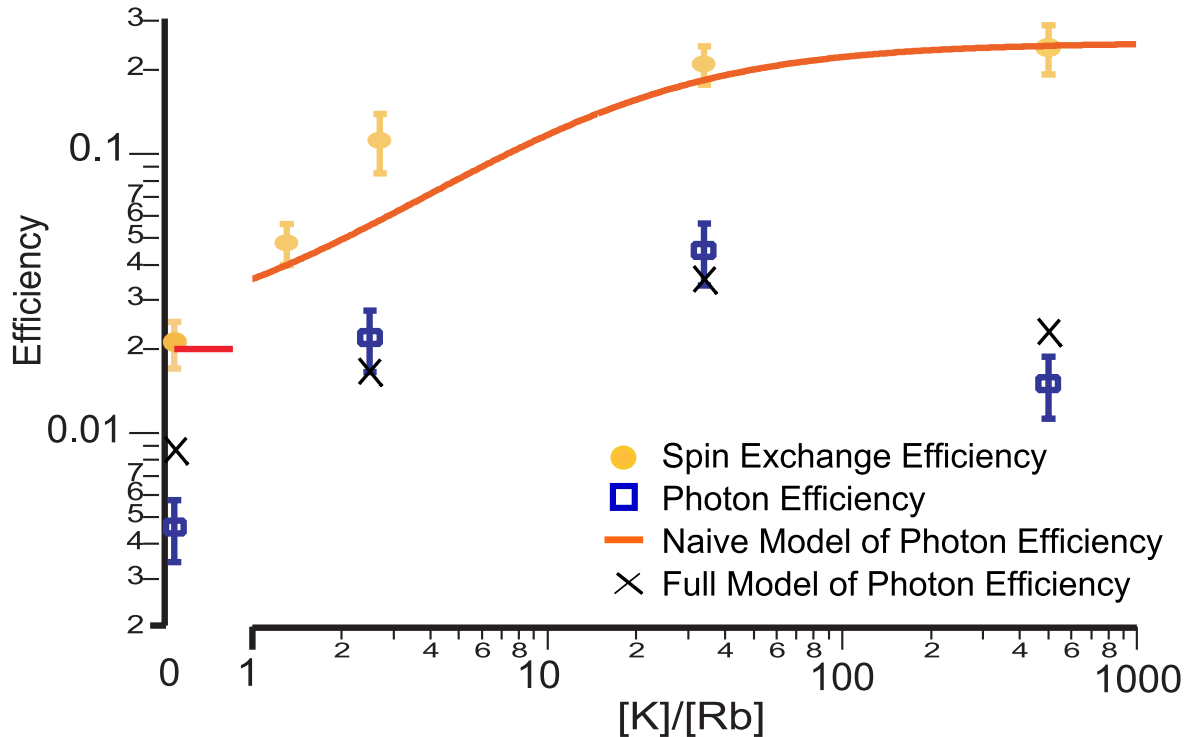


Figure 6.1 Measured spin exchange (yellow circles) and photon efficiencies (blue squares) for  $[\text{He}]=8$  amg cells with  $D=0$  to  $D=500$  [Babcock et al., 2003], along with a naive model for the photon efficiency (red-orange line) and a model that includes dark state absorption, excited state nuclear spin relaxation and potassium absorption at the Rb resonance (black crosses).

to 62 W, the value stated in [Babcock et al., 2003]. In the hybrid cells, the model is now in good agreement with the data. For the pure Rb cell, the modeled photon efficiency is reduced by a factor of  $\sim 3$  by including the dark state absorption, but is still significantly higher than the measured value. This discrepancy is not currently understood.

The relative importance of the angular momentum relaxation mechanisms can be seen in Fig. 6.2. This figure shows models of the ratio of the photon efficiency to the spin exchange efficiency. This ratio is the relative efficiency of optical pumping for the particular experimental conditions compared to the theoretical limit. Fig. 6.2 shows the modeled relative efficiencies in the high  $[\text{}^3\text{He}]$  cells used in [Babcock et al., 2003]. First, models were done including only ground-state spin destruction collisions and wall collisions as spin relaxation mechanisms. Then dark state absorption

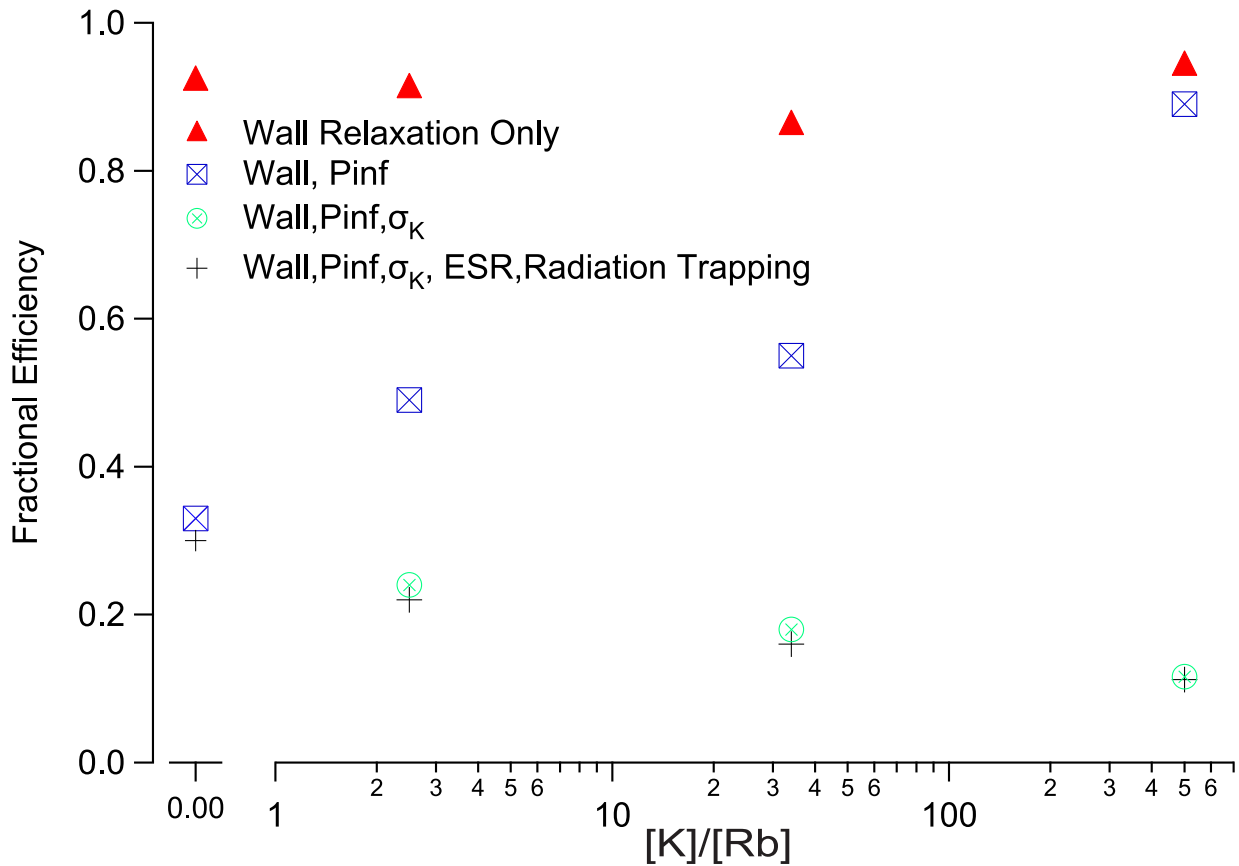


Figure 6.2 Spin exchange and photon efficiencies for  $[\text{He}]=8$  amg cells with  $D=0$  to  $D=500$ . In all cases photon efficiencies are 5 to 10 times lower than the fundamental spin exchange efficiencies. This implies that sources of alkali-metal spin relaxation are not fully understood.

was added, followed by potassium absorption and then excited state nuclear spin relaxation and radiation trapping. First, note that with all relaxation mechanisms included, the efficiencies go from .3 in the pure Rb cell to .11 in the  $D=500$  cell. If ground state spin destruction collisions were the only important relaxation mechanism, the relative efficiencies would be unity. The low efficiencies imply that in high  $[\text{He}]$  cells, the angular momentum loss mechanisms explored in this thesis account for 2 to 9 times as much loss as the ground state collisions, previously considered to be the dominant mechanism. In the  $D=500$  cell, the potassium absorption accounts for almost all of the excess light absorption, in the  $D=34$  cell, the contributions from dark state absorption and potassium absorption are roughly equal, and in the  $D=2.5$  cell, the dark state absorption is somewhat more significant.

To further evaluate the effect of K-<sup>3</sup>He and Rb dark state absorption, we modeled  $P_{max}$  by solving Eq. 6.23 including all terms at very high pump power. Fig. 6.3 shows  $P_{max}$  as a function of  $D$  for a [He]=7.9 amg cell pumped with a broadband ( $\sim 800$  GHz) and a narrowband (100 GHz) pumping source, and for [He]=6.0,4.0,2.0 and 1.0 amg cells with narrowband pumping.  $P_{max}$  is increased dramatically at all  $D$  by using a narrowband pump. The photon efficiencies were also calculated for narrowband pumping of the [He]=7.9 cells, and they were increased by a factor of 2 over broadband pumping at  $D=0$  and up to a factor of 3.2 at  $D=500$ . This illustrates the fact that since both dark state and K-<sup>3</sup>He absorption are broadband, while the Rb absorption that optical pumps the atoms is strongly resonant, it is important to use light as narrow spectrally as is practical.

$P_{max}$  also increases with decreased <sup>3</sup>He pressure, and should remain high even at high  $D$  for [He]=1.0 amg. Both the dark state absorption and the K absorption are proportional to [He], and so their impact is accentuated at high [He]. This helps explain why attempts to improve the optical pumping performance of broadband pumping sources by going to higher [He] did not work as well as predicted.

## 6.11 Optical Pumping Data

Naive models that include only ground state spin destruction collisions as a relaxation mechanism for the alkali-metal spins have consistently failed to accurately model optical pumping in SEOP and HySEOP experiments. There is a limited amount of published data showing the performance of optical pumping under specific experimental conditions, but we shall here attempt to model that data to see if our model, including dark state absorption, K-<sup>3</sup>He absorption and excited state nuclear spin relaxation can reproduce the data accurately.

Chen *et al.* did a thorough study of the performance of SEOP and HySEOP in a variety of cells. First we will look at their measurement of  $P_{Rb}$  as a function of spin exchange rate (which increases linearly with alkali-metal density) in a pure Rb cell. They report a systematic problem with their modeling of pure Rb cells pumped with narrowband sources, which predicts higher  $P_{Rb}$  than experimentally observed. The cell they present extensive data for is a large cylindrical cell

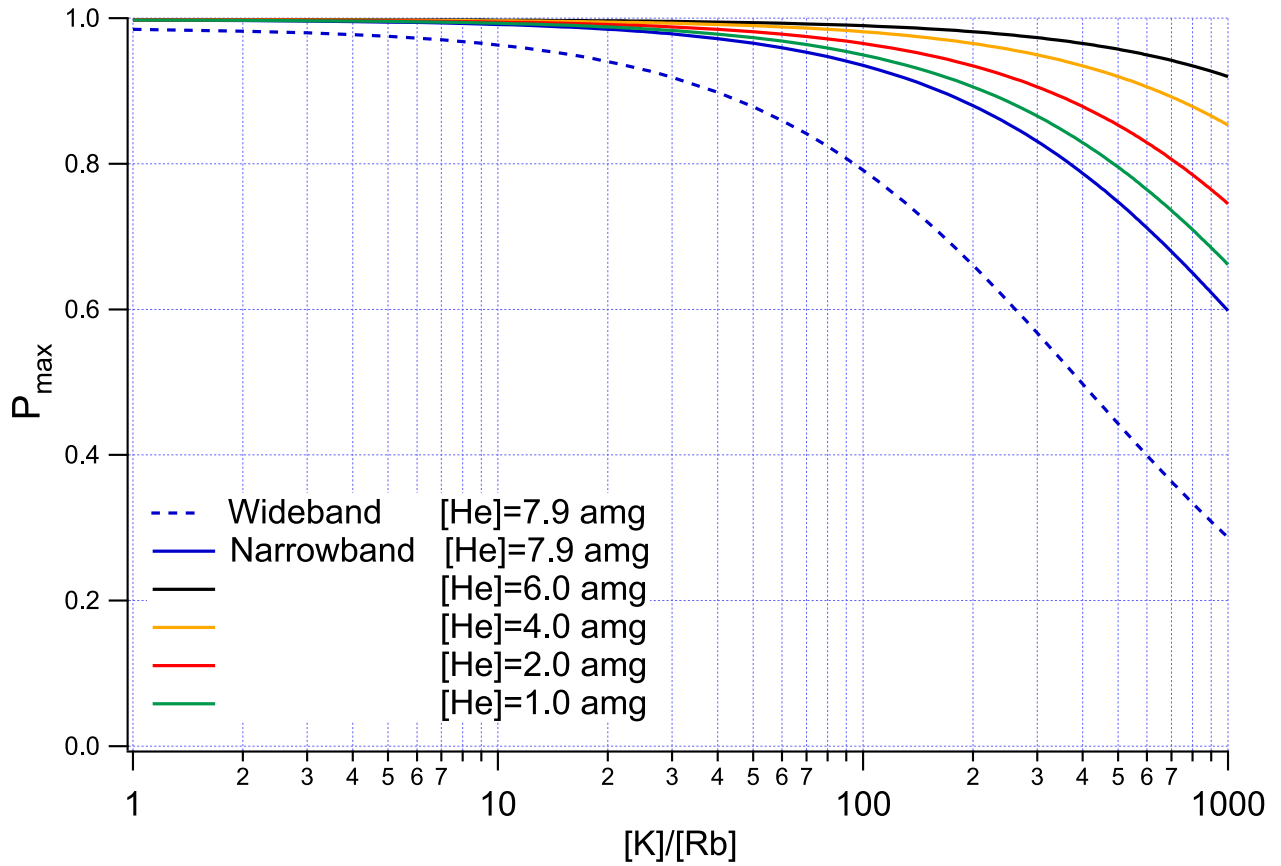


Figure 6.3  $P_{max}$  as a function of  $D$  for  $[\text{He}] = 7.9$  amg with broadband ( $\sim 800$  GHz) and narrowband (100 GHz) pumping sources, and for  $[\text{He}] = 6.0, 4.0, 2.0$  and  $1.0$  with narrowband pumping.

with  $[\text{He}] = 1.25$  amg and  $[\text{N}_2] = 50$  torr. They pumped the cell with two frequency narrowed diode array bars with linewidths of  $0.21$  nm and  $0.25$  nm, and a total of  $52$  W. They observed that  $P_{\text{Rb}}$  fell off much faster with increasing  $[\text{Rb}]$  than their models (which did not include dark-state absorption or excited state nuclear spin relaxation) predicted.

For our model, we used the laser spectrum shown in [Chen et al., 2007] for the  $0.25$  nm linewidth laser, and the total power  $52$  W. From Fig. 5.2, we deduce  $f_I = 0.045$ . Also,  $12\%$  of the pump light is assumed to be lost to reflections at the front surfaces of the oven and cell. The results of our modeling are shown in Fig. 6.4, with and without dark-state absorption and excited state nuclear spin relaxation. As with their modeling, our naive model grossly overestimates  $P_{\text{Rb}}$ . The introduction of dark-state absorption, excited state relaxation and radiation trapping significantly decreases

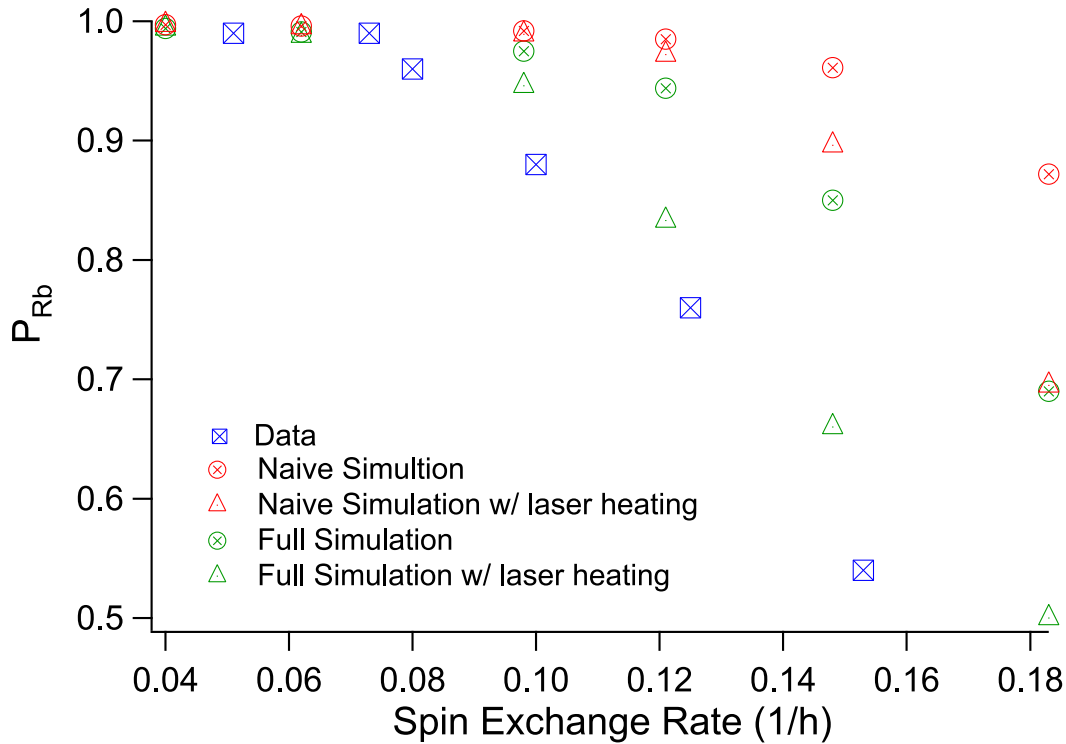


Figure 6.4  $P_{\text{Rb}}$  as a function of the spin exchange rate in a pure Rb,  $[\text{He}] = 1.24$  amg cell pumped with 52W of narrowband ( $\sim 125$  GHz) light. Measured values from [Chen et al., 2007] (blue squares), naive models with (red diamonds) and without (red circles) laser heating, and full models including the relaxation mechanisms described in this thesis with (green diamonds) and without (green circles) laser heating are shown. Including all relaxation mechanisms and estimate laser heating effects produces results in reasonable agreement with the data.

the spin exchange rate at which  $P_{\text{Rb}}$  begins to drop off, but still overestimates  $P_{\text{Rb}}$  at high spin exchange rates.

As briefly mentioned in Chapter 5, another potentially significant effect is the heating of the gases due to absorption of the pump light [Walter et al., 2001]. The inclusion of  $\text{N}_2$  gas in SEOP cells suppresses spontaneous emission, since excited Rb atoms rapidly transfer the pump photon energy to the ro-vibrational modes of the  $\text{N}_2$  buffer gas in quenching collisions. This energy is transferred to the translational motion of the gases, leading to heating. Walter *et al.* showed that in SEOP cells, the absorption of pump light leads to large temperature gradients in SEOP cells, where temperatures in the center of the cells greatly exceeded temperatures at the walls. The wall temperature governs  $[\text{Rb}]$ , so  $[\text{Rb}]$  remains constant if the oven temperature is controlled to keep

the cell wall temperature constant. However, the Rb-N<sub>2</sub> and Rb-<sup>3</sup>He relaxation rates are strongly temperature dependent (the Rb-Rb relaxation rate has a very small temperature dependence) and so the ground state spin destruction rate can increase significantly if the bulk temperature is increased.

We have included this effects in the model in the following way. First, the model is run assuming the cell temperature is uniform. Then, the amount of power dissipated in the cell is calculated, and this power dissipation is used to calculate the temperature increase in the center of the cell. For now, we only make a crude estimate of the temperature increase, based on the information in [Walter et al., 2001]. They list the increase in temperature per Watt of absorbed light for several cells. They also show the temperature profile as a function of transverse position in one cell. At high absorbed power, the temperature profile is fairly flat, with most of the temperature decrease in a thin layer near the wall (characteristic of convective heat flow). from fitting this profile, we estimate that the average temperature in a convective cell is  $\sim 0.8$  times the center temperature. It is difficult to estimate what the increase in center temperature would be in this cell. A cell of similar buffer gas density, but cubic, and with a volume three times smaller had a temperature rise of 8 K/W. The general trend seems to be toward slightly lower temperature increases in larger volume cells. Also, a cell of 3.5 amg buffer gas, but a volume of more than 2/3 that of the [Chen et al., 2007] cell has a temperature rise of 5 K/W. The general trend appears to be toward lower temperature rises at higher buffer gas densities. from this, we guess a temperature rise of 5 K/W, which we feel is conservative.

The model is run again, with the Rb-<sup>3</sup>He and Rb-N<sub>2</sub> relaxation rates calculated at the elevated temperature. The power dissipation is calculated again, the temperature increased accordingly, and the model run again. Further iteration was not necessary, as the power dissipation increases very slowly after the second iteration. The results are shown in Fig 6.4, and are in reasonable agreement with the data. It should be emphasized that these results are preliminary, as the laser heating needs to be dealt with in a more sophisticated way. Also, modeling in the regime where the alkali-metal polarization begins to drop significantly from unity is very sensitive to the pump laser parameters. For narrowband pumping,  $P_{\text{Rb}}$  typically remains quite high until the pump light is nearly completely extinguished. The distance into the cell at which this occurs determines the

bulk average polarization. This distance is quite sensitive to the amount of input power, the pump spectral profile and detuning, and the relaxation rate. Still, the models indicate that the inclusion of both the novel relaxation mechanisms we have studied and a treatment of laser induced heating can account for the poor optical pumping performance of pure Rb cells with narrowband pumping, which was previously not understood.

Chen *et al.* also measured  $P_{\text{Rb}}$  as a function of the spin exchange rate in a  $D=4.8$ ,  $[\text{He}]=3.45$  amg cell. In that cell their pumping appeared to slightly outperform their naive model. This is partly due to the fact that they used a Lorentzian lineshape for the pump laser in their models, while their measured pump profiles are more nearly Gaussian. Still, a naive model we ran using the a combination of the measured spectral profile of the 0.25nm linewidth pump laser and a Gaussian profile (which fits well) for the 0.21nm linewidth pump laser was in good agreement with their data (Fig. 6.5). The inclusion of dark state absorption and excited state spin relaxation produces a model that predicts slightly lower  $P_{\text{Rb}}$  than the measured values.

Again, we attempted to include the laser heating. This cell is very large ( $800 \text{ cm}^3$ ) compared to the largest cell used in [Walter et al., 2001] ( $220 \text{ cm}^2$ ), although the two cells have similar buffer gas pressure. The large cell in [Walter et al., 2001] had a temperature rise of 5 K/W, so we estimate that the larger cell would have a rise of 3 K/W. Inclusion of a heating of this magnitude increases the pump absorption in the simulations, leading to predicted  $P_{\text{Rb}}$  that are much lower than the measured values at high spin-exchange rate. It is unclear why the model compares so much differently to the results from this cell, as compared to the pure Rb cell. It could be that we have overestimated the heating in this cell.

In [Chen et al., 2007], they also report low alkali polarizations measured in two high  $D$  cells pumped with high power narrowband light at modest alkali-metal density. The cells are a  $D=46$ ,  $[\text{He}]=1.91$  amg cell with 50 Torr  $\text{N}_2$  and a  $D=155$ ,  $[\text{He}]=1.10$  amg, with 50 Torr  $\text{N}_2$ . The  $D=46$  cell was pumped with 52W of narrowband power at  $T=210^\circ\text{C}$ , with measured  $P_{\text{Rb}} \sim .77$ , and the  $D=155$  cell was pumped with 18W of narrowband light and 25W of broadband power at  $T=225^\circ\text{C}$ , with measured  $P_{\text{Rb}} \sim .62$ . They achieved high polarization in the pumping of a  $D=6.2$ ,  $[\text{He}]=1.4$  amg cell. The results of our modeling are shown in Table 6.1.

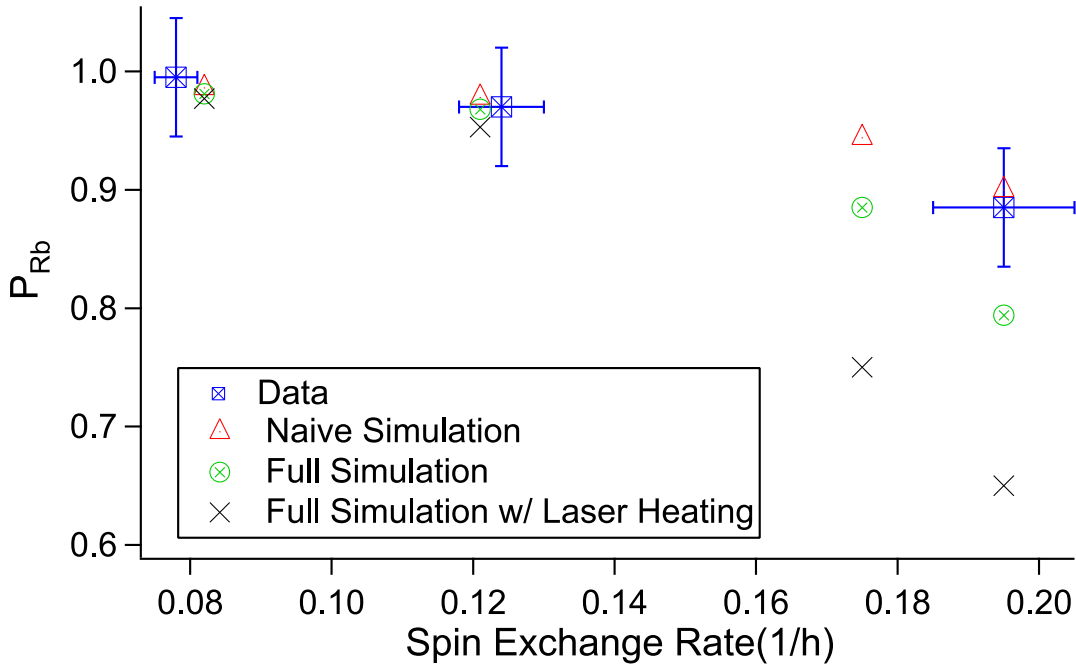


Figure 6.5  $P_{\text{Rb}}$  as a function of the spin exchange rate in a  $D=4.8$ ,  $[\text{He}]=3.45$  amg cell pumped with 52W of narrowband ( $\sim 125$  GHz) light. Measured values from [Chen et al., 2007] (blue squares), naive models without (red circles) laser heating, and full models including the relaxation mechanisms described in this thesis with (black crosses) and without (green circles) laser heating are shown. Models that include all known relaxation underestimate  $P_{\text{Rb}}$  at high spin exchange rate, and the inclusion of laser heating greatly increases the discrepancy.

There is an expectation that, with a fixed amount of laser power, the achieved  $P_A$  should decrease with increasing  $D$  due to the fact that the pump laser directly interacts with a decreasing fraction of the alkali-metal atoms. For the conditions described in [Chen et al., 2007], this accounts for only a fraction of the decrease in  $P_A$ , and the inclusion of dark state absorption, excited state spin relaxation and  $\text{K-}^3\text{He}$  absorption only leads to a small decrease in  $P_A$ . Heating is unimportant under these conditions, as there is a small amount of dissipated power.

One other report of optical pumping performance we can model is from [Chann et al., 2003], where they report the increased optical pumping performance of frequency narrowed diode array bars compared to unnarrowed bars. They show the Rb polarization in a  $[\text{He}]=0.85$  amg,  $[\text{N}_2]=50$  Torr cell as a function of  $[\text{Rb}]$  when pumped by 14W of narrowband (125 GHz) pump light and when pumped by 42W of unnarrowed (1200 GHz) light. The lower power narrowband pumping

$D$	$P_A(expt.)$	$P_A(naive\ model)$	$P_A(full\ model)$
6.2	$\sim .99$	.987	.985
46	.77	.964	.946
155	.62	.861	.816

Table 6.1 Comparison of measured ([Chen et al., 2007]) and modeled  $P_A$  in [He]  $\sim 1.5$  amg cells of increasing  $D$ . Low  $P_A$  at high  $D$  is not explained by dark state and  $K\text{-}^3\text{He}$  absorption.

maintains high  $P_{Rb}$  up to  $[Rb] \sim 4 \times 10^{14} \text{cm}^{-3}$ , while  $P_{Rb}$  drops steadily from  $[Rb] \sim 1 \times 10^{14} \text{cm}^{-3}$ , (Fig. 6.6). Naive modeling predicts very high  $P_{Rb}$  at these densities with both pump sources, making the reason why narrowband pumping performs much better than broadband pumping unclear.

When the additional relaxation mechanisms and laser heating are added to the model (at 12 K/W, a good estimate as this cell is very similar to one used in [Walter et al., 2001]) the qualitative behavior of the data is reproduced. The alkali-metal polarization is shown to drop off starting at fairly low [Rb] for the broadband pumping, although not to the degree which the measured polarization does. High polarization is maintained for the narrowband pumping, although it too drops off more slowly at high [Rb] than the measured values. The absolute agreement between model and data is not very good, but the improved performance of narrowband pumping is demonstrated in the modeling. The inclusion of the additional relaxation methods investigated in this thesis in our models has produced much more accurate results than previous attempts to model SEOP over a wide range of parameters. We have accurately reproduced the efficiency of HySEOP in high [He] cells, which was previously not understood. We have also reproduced the poor optical pumping performance of a pure Rb cell at modest [He], which was previously not understood as well. We are also able to qualitatively understand why the switch to narrowband pumping sources has produced such a increase in optical pumping performance, when previous models suggested that pumping with broadband sources should work nearly as well. Nonetheless, there are still some problems with the modeling. The poor performance reported in high  $D$  cells of modest [He] in

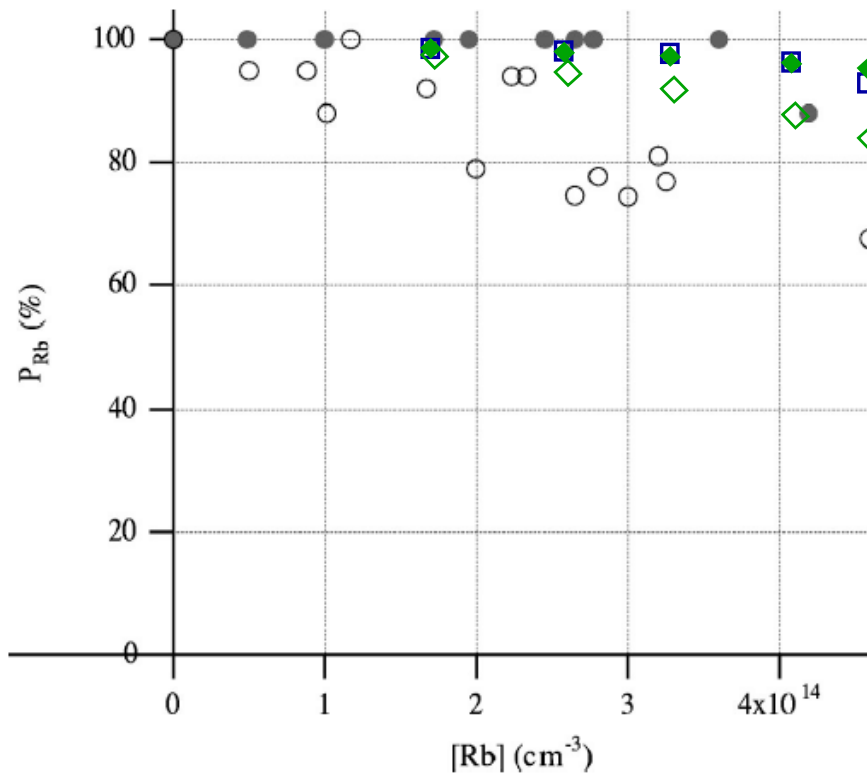


Figure 6.6 Measured values of  $P_{\text{Rb}}$  as a function of Rb density in a pure Rb,  $[\text{He}] = 0.85 \text{ amg cell}$  pumped with 14W of narrowband light (closed circles) and 42W of broadband light (open circles) from [Chann et al., 2003]. Naive (closed green diamonds) and full (open green diamonds) modeling (including laser heating) of the broadband pumping, and full modeling of the narrowband pumping (blue squares) are also shown.

[Chen et al., 2007] cannot be understood with our models. Also, it appears that a strong understanding of laser heating effects will be needed to produce accurate models. We have not yet implemented a sophisticated treatment of laser heating.

**DISCARD THIS PAGE**

## Appendix A: Helium Polarimetry

### A.1 EPR Frequency Shift Polarimetry

Our SEOP apparatus also includes diagnostics for measuring the polarization of the  $^3\text{He}$  spins. Absolute measurements of the  $^3\text{He}$  spin are made by measuring the shift in the Rb ground state sub-level transitions as the  $^3\text{He}$  spins are flipped ([Schaefer et al., 1989, Barton et al., 1994, Romalis and Cates, 1998]). The aligned  $^3\text{He}$  spins apply an effective magnetic field to the Rb atoms, proportional to  $[\text{He}]$ ,  $P_{\text{He}}$ , and an enhancement factor  $\kappa_0$ , which shifts the frequency of the EPR transitions in the Rb ground state. The enhancement factor has been measured accurately by [Romalis and Cates, 1998] for Rb- $^3\text{He}$  and by [Babcock et al., 2005b] for K- $^3\text{He}$ . Thus, a measurement of the EPR frequency shift can be used to deduce  $P_{\text{He}}$  if the  $^3\text{He}$  density is known.

The procedure for measuring the frequency shift is as follows. First, we monitor the polarization of the 780nm probe beam as the frequency of the RF field is scanned to locate the EPR resonance. Then, we frequency modulate the RF field, and send the polarization rotation signal to a lock-in amplifier referenced to the modulation frequency. The output of the lock-in has a dispersion type lineshape as the RF frequency is scanned across the EPR resonance, and is fed to a locking circuit, which locks the RF frequency to the zero-crossing of the dispersion lineshape. The RF frequency is measured by a counter, and read by a DAQ as the  $^3\text{He}$  spins are repeatedly flipped using adiabatic fast passage (AFP). The magnitude of the  $^3\text{He}$  induced frequency shift can then be determined and  $P_{\text{He}}$  deduced.

Using the Breit-Rabi formula [Ramsey, 1953] as shown in chapter 2, we can approximate the EPR frequencies

$$\frac{E_m - E_{m-1}}{\hbar} \approx \frac{g_I \mu_B B_z}{\hbar} \pm \frac{E_{hf}}{\hbar} \left[ \frac{1}{2I+1} \frac{(g_I - g_J) \mu_B B_z}{E_{hf}} + \frac{1}{(2I+1)^2} \left( \frac{(g_I - g_J) \mu_B B_z}{E_{hf}} \right)^2 (1 - 2m) \right] \quad (\text{A.1})$$

where the  $\pm$  is for  $F = I \pm 1/2$ . The field dependence of the frequency is found by taking the derivative with respect to  $B_z$

$$\delta_\omega = \frac{g_I \mu_B \delta B}{\hbar} \pm \frac{1}{2I+1} \frac{(g_I - g_J) \mu_B \delta B}{\hbar} \quad (\text{A.2})$$

where we have dropped the higher order terms in  $B_z$ , since we operate at low fields. Also, since  $g_J \gg g_I$  we can simplify to

$$\delta_\omega \approx \mp \frac{1}{2I+1} \frac{g_J \mu_B \delta B}{\hbar} \quad (\text{A.3})$$

The classical magnetic field seen by the Rb atoms due to the polarized  $^3\text{He}$  atoms is roughly that at the center of a spherical distribution of spins

$$\delta B \approx \frac{8\pi M}{3} \quad (\text{A.4})$$

where  $M = \mu_{\text{He}}[\text{He}]P_{\text{He}}$  is the magnetization of the  $^3\text{He}$  atoms. The Fermi contact interaction in Rb- $^3\text{He}$  collisions produces an additional effective magnetic field, the magnitude of which is  $(\kappa_0 - 1)\delta B$ . Thus we can get the approximate frequency shift

$$\delta_\nu = \frac{8}{3} \pi \frac{g_J \mu_B}{h(2I+1)} \kappa_0 \mu_{\text{He}}[\text{He}] P_{\text{He}} \quad (\text{A.5})$$

$$= \left( 1.13 \frac{\text{KHz}}{\text{amagat}} \right) \kappa_0 [\text{He}] P_{\text{He}} \quad (\text{A.6})$$

The above expression for  $\delta_\nu$  assumes a spherical cell and uses only first order terms in  $B_z$ . The geometric correction for a cylindrical geometry is derived in [Chann, 2003] and [Babcock, 2005]. The total enhancement factor becomes  $\kappa = \kappa_0 + \delta\kappa$ , where

$$\delta\kappa = \frac{3}{2L} (\sqrt{a^2 + L^2} - a) - 1 \quad (\text{A.7})$$

where  $a$  is the radius of the cylinder, and  $L$  is the length. The higher order terms in  $B_z$  are corrected for by multiplying  $\kappa$  by  $(1+\epsilon)$ , where  $\epsilon$  was calculated in [Babcock, 2005] (Fig. B.1). The experimental apparatus was built by Earl Babcock and the details of the EPR locking circuit, AFP power amplifier circuit, and the VCO function generator used as the RF source for EPR frequency locking are described in [Babcock et al., 2005a].

## A.2 FID

A simpler method for measuring the relative magnetization of the  $^3\text{He}$  is free induction decay (FID). In this method, a short RF pulse near the  $^3\text{He}$  Larmor resonance (3.24 KHz/Gauss) is applied

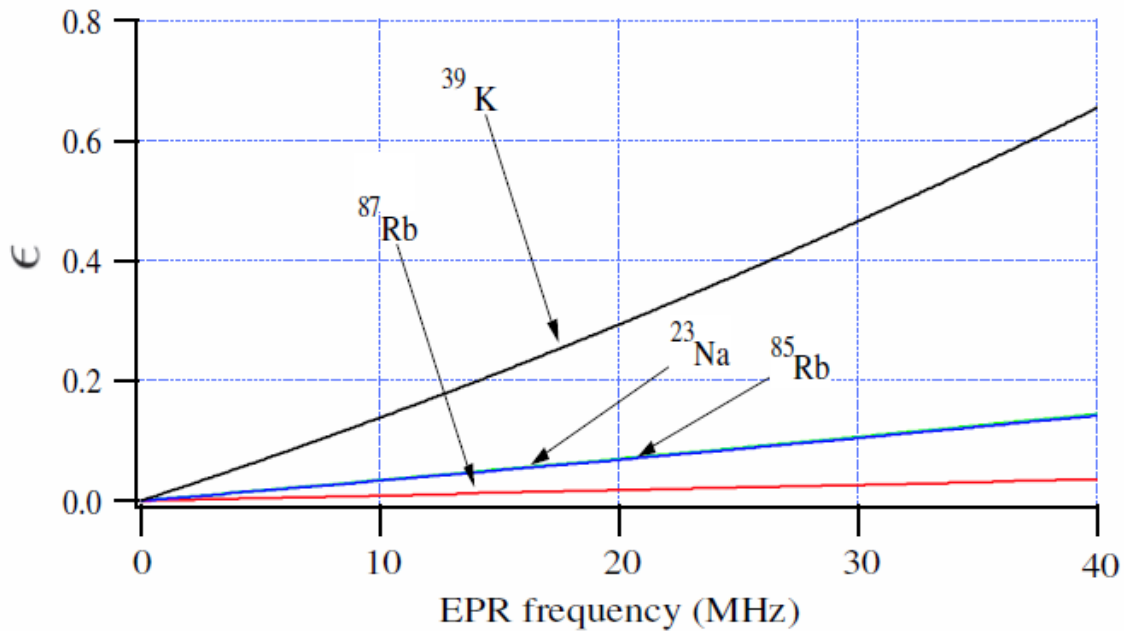


Figure A.1 Plot (calculated in [Babcock et al., 2005a]) of the magnetic correction factor for the various alkali isotopes as a function of the EPR frequency. Note that for the special case of  $^{85}\text{Rb}$  and  $^{23}\text{Na}$  the correction factors follow each other to less than 0.1%

to tip the  $^3\text{He}$  spins. The spins then precess about the static holding field, inducing an EMF in a pickup coil. The magnitude of this signal is proportional to the magnetization of the spins.

In FID apparatus is controlled by a computer using a National Instruments DAQ and a LabView program. The DAQ outputs an analog AC pulse near the  $^3\text{He}$  Larmor frequency to an FID conditioning circuit which drives a 300 turn, 34 gauge, 2cm diameter coil placed under the SEOP cell. The pulse gives a small tip to the  $^3\text{He}$  spins, into the plane perpendicular to the magnetic holding field. The spins then precess around the holding field at the  $^3\text{He}$  Larmor frequency and dephase with a time constant  $T_2$ .  $T_2$  in our apparatus is typically 50ms, dominated by field gradients and diffusion. Shim coils are used to maximize  $T_2$ .

The NMR drive coil is also used as the pick-up coil, in parallel with a variable capacitor which is set to make a tank circuit resonant at the NMR frequency, maximizing the induced  $EMF$ . This  $EMF$  is pre-amplified by our signal conditioning circuit and sent to a lock-in amplifier with the lock-in reference frequency detuned from the  $^3\text{He}$  Larmor frequency by  $\sim 100\text{Hz}$ . The output

of the lock-in is recorded by the analog input of the DAQ. A diagram of the NMR FID system is shown in Fig. A.2. A typical data set is shown in Fig. ???. Note that the signal oscillates at the difference frequency between the  $^3\text{He}$  Larmor frequency and the lock-in reference frequency. This allows us to fit the decay of the signal, and retrieve the initial amplitude, without precisely eliminating any DC offset of the signal. The initial magnitude of the signal is proportional to the magnetization of the  $^3\text{He}$  spins, giving us a relative measure of  $P_{\text{He}}$ . These measurements can be taken over time to observe the build up or relaxation of the  $^3\text{He}$  spins.

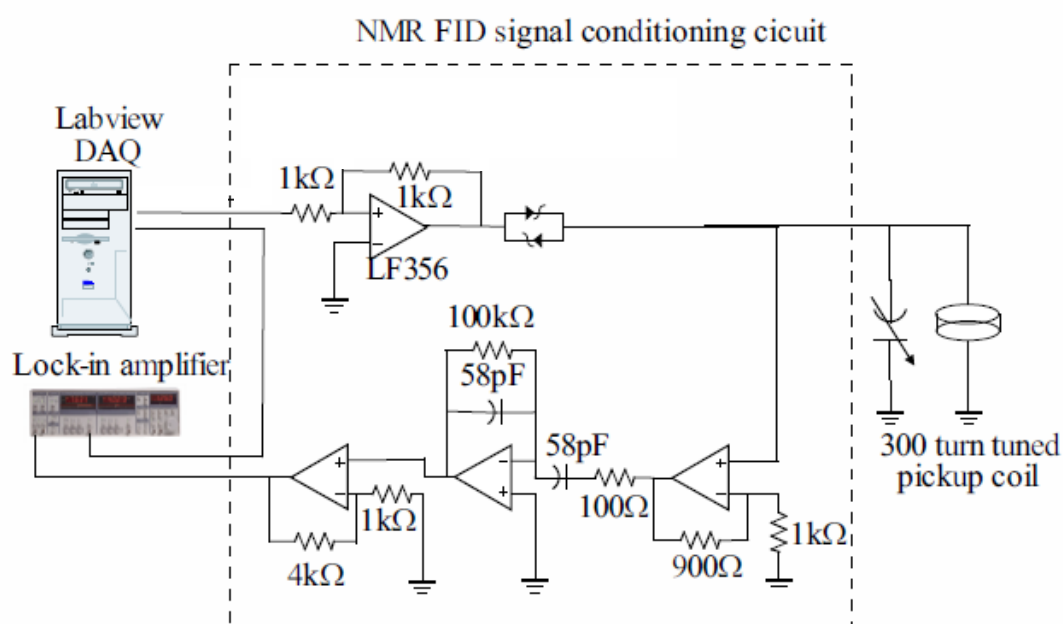


Figure A.2 Plot (Diagram of the NMR FID setup).

## Appendix B: Alkali-Metal Vapor Pressure Curves

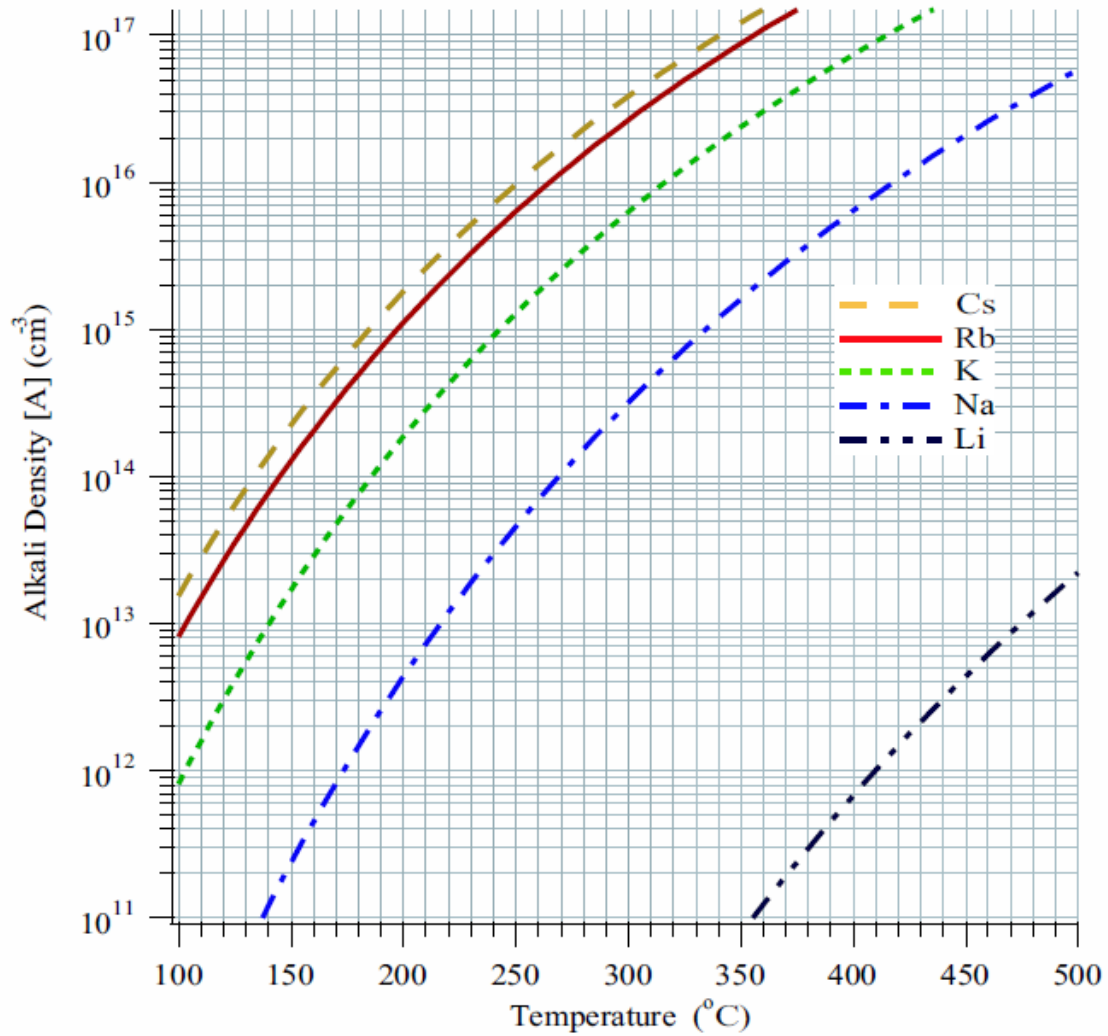


Figure B.1 Vapor pressure curves for Cs,Rb,K,Na, and Li.

	A	B
Cs	4.165	3830
Rb	4.312	4040
K	4.402	4453
Na	4.704	5377
Li	5.055	8310

Table B.1 The coefficients for determining the vapor pressures of the alkali-metals [Lide, 2011]. Number densities are given by  $[A]=7.336 \times 10^{21} T^{-1} (10^{A+BT^{-1}})$  where  $T$  is the temperature in Kelvin and  $[A]$  will be in  $\text{cm}^{-3}$ .

## Appendix C: Spin Temperature

When the rate of spin-exchange collisions between alkali-metal atoms or the ground state hyperfine frequency are high compared to all other rates in the alkali-metal spin evolution equation, namely the optical pumping rate, the atoms will be in a spin temperature distribution ([?, Anderson et al., 1959]). In spin temperature, all the ground state populations and  $P_{\text{Rb}}$  can be written in terms of one parameter, the inverse spin temperature  $\beta$ . The polarization is written

$$P_{\text{Rb}} = 2 \tanh^{-1}(\beta) \quad (\text{C.1})$$

$\beta$  can also be used to calculate the ratio of the populations of two sublevels of azimuthal quantum numbers  $m$  and  $m - 1$

$$e^{-\beta} = \frac{\rho_m}{\rho_{m-1}} \quad (\text{C.2})$$

Furthermore, the nuclear spin  $\langle I_z \rangle$  can be related to the electron spin  $\langle S_z \rangle$  by  $\langle I_z \rangle = \epsilon(I, \beta) \langle S_z \rangle$ , where the paramagnetic coefficient is defined ([Walker and Happer, 1997])

$$\epsilon(K, \beta) = (2K + 1) \coth(\beta/2) \coth(\beta(K + 1/2)) - \coth^2(\beta/2) \quad (\text{C.3})$$

## Appendix D: Far Wing Cross Sections

From the transmission data collected for the measurement of the dark state absorption we extracted the Rb-N<sub>2</sub> and Rb-<sup>3</sup>He pressure broadened absorption cross-sections (Fig. 3.9 and Fig. 3.11). For use in our models, we fit these cross sections to appropriate fit functions.

### D.1 Rb-<sup>3</sup>He Cross Section

First, we look at the Rb-<sup>3</sup>He cross section. In the region between -500 GHz and 500GHz, the cross section is well fit by the lineshape from [Romalis et al., 1997], with a linear approximation  $I(x) = 0.3380 - 0.2245x$  for the shape function (Table refIofX). We fit the transmission data from NHRb for detunings between +1500 GHz and 500GHz, and between -1500 GHz and -500GHz. We assume that at these detunings the cross section is linear in [<sup>3</sup>He], so we divide the fit by 3.27 to produce a cross-section in units of  $\frac{\text{cm}^2}{\text{amg}}$ .

### D.2 Rb-N<sub>2</sub> Cross Section

The Rb-N<sub>2</sub> cross section is well fit by the lineshape from [Romalis et al., 1997], with a linear approximation  $I(x) = 0.3380 - 0.2245x$  for the shape function in the region from -200 GHz to 100 GHz. Fits of the transmission data from the cell K2 were made for larger detunings, and scaled by [N<sub>2</sub>] (Table D.2).

Detuning Range (GHz)	Cross Section
-1500 to -500	$(5.0 \times 10^{-17} + 2.47 \times 10^{-15} e^{.0051(\nu-\nu_1)}) \frac{[\text{He}] \text{ cm}^2}{3.27 \text{ amg}}$
-500 to 500	$1.406 \times 10^{-12} \times \frac{1+.664 \times 2\pi T_d(\nu-\nu_1)}{\gamma_{\text{Rb}}^2/4+(\nu-\nu_1)^2} \text{cm}^2$
500 to 1500	$(5.586 \times 10^{-17} + 2.57 \times 10^{-15} e^{-.00371(\nu-\nu_1)}) \frac{[\text{He}] \text{ cm}^2}{3.27 \text{ amg}}$

Table D.1 Functions for the Rb-<sup>3</sup>He pressure broadened absorption cross section. The near resonance function is the lineshape from [Romalis et al., 1997], with a linear approximation  $I(x) = 0.3380 - 0.2245x$  for the shape function. The cross sections in the wings are fits to the NHRb transmission data, scaled by [<sup>3</sup>He].

Detuning Range (GHz)	Cross Section
-1000 to -200	$(2.14 \times 10^{-17} + 6.27 \times 10^{-11} / ((\Delta + 55.3)^2 - 286.6)) \frac{[N_2] \text{ cm}^2}{2.80 \text{ amg}}$
-200 to 100	$1.406 \times 10^{-12} \times \frac{1 + .664 \times 2\pi T_d \Delta}{\gamma_{\text{Rb}}^2 / 4 + \Delta^2} \text{ cm}^2$
200 to 290	$(6.99 \times 10^{-17} + 4.18 \times 10^{-11} / ((\Delta + 47.2)^2 - 7739)) \frac{[N_2] \text{ cm}^2}{2.80 \text{ amg}}$
290 to 2100	$(3.57 \times 10^{-17} + 1.0 \times 10^{-15} e^{-((\Delta+100)/400)}) \frac{[N_2] \text{ cm}^2}{2.80 \text{ amg}}$

Table D.2 Functions for the Rb-N<sub>2</sub> pressure broadened absorption cross section. The near resonance function is the lineshape from [Romalis et al., 1997], with a linear approximation  $I(x) = 0.3380 - 0.2245x$  for the shape function. The cross sections in the wings are fits to the K2 transmission data, scaled by [N<sub>2</sub>].

## Appendix E: Equations for EPR Spectroscopy in Non-Spin Temperature Distributions

As discussed in chapter 2, when the Rb atoms are not in spin temperature, it is necessary to use all the resolvable peaks of the EPR spectrum to solve for the ground state sublevel populations. For  $^{85}\text{Rb}$ , the peak areas are defined as shown in Fig. E.1. The peak areas are related by raising operator coefficients to population differences

### E.1 $^{85}\text{Rb}$

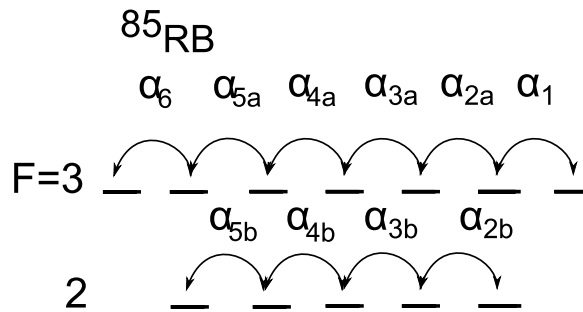


Figure E.1 Labels of the peak areas in  $^{85}\text{Rb}$  EPR spectroscopy.

$$\alpha_1 \propto 6(\rho_{33} - \rho_{32}) \quad (\text{E.1})$$

$$\alpha_{2a} \propto 10(\rho_{32} - \rho_{31}) \quad (\text{E.2})$$

$$\alpha_{2b} \propto 4(\rho_{22} - \rho_{21}) \quad (\text{E.3})$$

$$\alpha_{3a} \propto 12(\rho_{31} - \rho_{30}) \quad (\text{E.4})$$

$$\alpha_{3b} \propto 6(\rho_{21} - \rho_{20}) \quad (\text{E.5})$$

$$\alpha_{4a} \propto 12(\rho_{30} - \rho_{3-1}) \quad (\text{E.6})$$

$$\alpha_{4b} \propto 6(\rho_{20} - \rho_{2-1}) \quad (\text{E.7})$$

$$\alpha_{5a} \propto 10(\rho_{3-1} - \rho_{3-2}) \quad (\text{E.8})$$

$$\alpha_{5b} \propto 4(\rho_{2-1} - \rho_{2-2}) \quad (\text{E.9})$$

For 3 peak sets

$$R_1 = \frac{\alpha_1}{\alpha_{2a}} = \frac{3}{5} \frac{\rho_{33} - \rho_{32}}{\rho_{32} - \rho_{31}} \quad (\text{E.10})$$

$$R_2 = \frac{\alpha_{2a}}{\alpha_{3a}} = \frac{5}{6} \frac{\rho_{32} - \rho_{31}}{\rho_{31}} \quad (\text{E.11})$$

$$R_3 = \frac{\alpha_{2b}}{\alpha_{3b}} = \frac{2}{3} \left( \frac{\rho_{22}}{\rho_{21}} - 1 \right) \quad (\text{E.12})$$

$$R_5 = \frac{\alpha_{31}}{\alpha_{3b}} = 2 \frac{\rho_{31}}{\rho_{21}} \quad (\text{E.13})$$

Solving for the populations gives

$$\rho_{31} = \left( 2 + \frac{6}{5} R_2 \left( \frac{5}{3} R_1 + 2 \right) + \frac{R_3 + 4}{R_5} \right)^{-1} \quad (\text{E.14})$$

$$\rho_{21} = \frac{2}{R_5} \rho_{31} \quad (\text{E.15})$$

$$\rho_{22} = \frac{2 \left( \frac{3}{2} R_3 + 1 \right)}{R_5} \rho_{31} \quad (\text{E.16})$$

$$\rho_{32} = \left( \frac{6}{5} R_2 + 1 \right) \rho_{31} \quad (\text{E.17})$$

$$\rho_{33} = \left( 2 R_2 R_1 + \frac{6}{5} R_2 + 1 \right) \rho_{31} \quad (\text{E.18})$$

For 4 peak sets Fix This

$$\rho_{30} = \left( 1 + \frac{2}{A_7} + \frac{2(A_6 + 1)}{A_7} \left( 2 + \frac{3}{2} A_4 \right) - \frac{3A_4}{A_7} + (A_5 + 1) \left( \frac{6}{5} A_3 + 2 \right) \right. \quad (\text{E.19})$$

$$\left. - \frac{6}{5} A_3 + (A_5 + 1)(A_3 + 1) - \frac{6}{5} A_3 \left( \frac{5}{3} A_1 + 1 \right) - \frac{5}{3} A_1 (A_5 + 1) \right)^{-1} \quad (\text{E.20})$$

$$\rho_{20} = \frac{2}{A_7} \rho_{30} \quad (\text{E.21})$$

$$\rho_{31} = (A_5 + 1) \rho_{30} \quad (\text{E.22})$$

$$\rho_{21} = \frac{2(A_6 + 1)}{A_7} \rho_{30} \quad (\text{E.23})$$

$$\rho_{32} = \left( (A_5 + 1) \left( \frac{6}{5} A_3 + 1 \right) - \frac{6}{5} A_3 \right) \rho_{30} \quad (\text{E.24})$$

$$\rho_{22} = \left( \frac{2(A_6 + 1)}{A_7} \left( 1 + \frac{3}{2} A_4 \right) - \frac{3A_4}{A_7} \right) \rho_{30} \quad (\text{E.25})$$

$$\rho_{33} = \left( (A_5 + 1) \left( \frac{6}{5} A_3 + 1 \right) - \frac{6}{5} A_3 \right) \left( \frac{5}{3} A_1 + 1 \right) - \frac{5}{3} A_1 (A_5 + 1) \rho_{30} \quad (\text{E.26})$$

## E.2 $^{87}\text{Rb}$

For  $^{87}\text{Rb}$ , the peak areas are defined as shown in Fig. E.2. The peak areas are related by raising

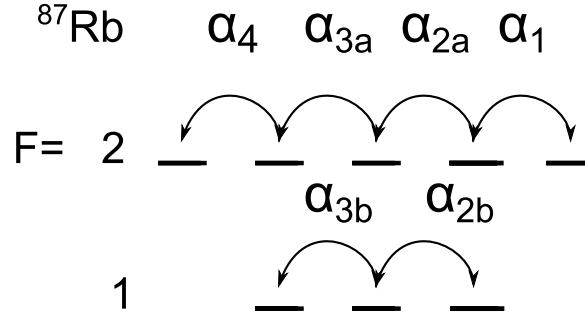


Figure E.2 Labels of the peak areas in  $^{87}\text{Rb}$  EPR spectroscopy.

operator coefficients to population differences

$$\alpha_1 \propto 4(\rho_{22} - \rho_{21}) \quad (\text{E.27})$$

$$\alpha_{2a} \propto 6(\rho_{21} - \rho_{20}) \quad (\text{E.28})$$

$$\alpha_{2b} \propto 2(\rho_{11} - \rho_{10}) \quad (\text{E.29})$$

$$\alpha_{3a} \propto 6(\rho_{20} - \rho_{2-1}) \quad (\text{E.30})$$

$$\alpha_{3b} \propto 2(\rho_{10} - \rho_{1-1}) \quad (\text{E.31})$$

$$\alpha_4 \propto 4(\rho_{2-1} - \rho_{2-2}) \quad (\text{E.32})$$

First we solve for the simple case of 2 peak sets (3 peaks) being resolvable. Define the ratios of peak areas

$$R_1 = \frac{\alpha_1}{\alpha_{2a}} = \frac{2}{3} \left( \frac{\rho_{22}}{\rho_{21}} - 1 \right) \quad (\text{E.33})$$

$$R_2 = \frac{\alpha_{2a}}{\alpha_{2b}} = 3 \frac{\rho_{21}}{\rho_{11}} \quad (\text{E.34})$$

Solving these equations for  $\rho_{22}, \rho_{21}$  and  $\rho_{11}$  assuming all other populations are zero gives

$$\rho_{11} = \left( 1 + \frac{R_2}{3} \left( \frac{3}{2} R_1 + 2 \right) \right)^{-1} \quad (\text{E.35})$$

$$\rho_{21} = \frac{R_2}{3} \rho_{11} \quad (\text{E.36})$$

$$\rho_{22} = \left( \frac{3}{2} R_1 + 1 \right) \rho_{21} \quad (\text{E.37})$$

For three peak sets, we have

$$R_1 = \frac{\alpha_1}{\alpha_{2a}} = \frac{2}{3} \frac{\rho_{22} - \rho_{21}}{\rho_{21} - \rho_{20}} \quad (\text{E.38})$$

$$R_2 = \frac{\alpha_{2a}}{\alpha_{2b}} = 3 \frac{\rho_{21} - \rho_{20}}{\rho_{11} - \rho_{10}} \quad (\text{E.39})$$

$$R_3 = \frac{\alpha_{2a}}{\alpha_{3a}} = \frac{\rho_{21} - \rho_{20}}{\rho_{20}} \quad (\text{E.40})$$

$$R_4 = \frac{\alpha_{3a}}{\alpha_{3b}} = 3 \frac{\rho_{20}}{\rho_{10}} \quad (\text{E.41})$$

Solving these for  $\rho_{22}$ ,  $\rho_{21}$ ,  $\rho_{20}$ ,  $\rho_{11}$ , and  $\rho_{10}$  gives

$$\rho_{10} = \left( R_3 R_4 \left( \frac{R_1}{2} + \frac{1}{R_2} + \frac{2}{3} \right) + R_4 + 2 \right)^{-1} \quad (\text{E.42})$$

$$\rho_{20} = \frac{R_4}{3} \left( R_3 R_4 \left( \frac{R_1}{2} + \frac{1}{R_2} + \frac{2}{3} \right) + R_4 + 2 \right)^{-1} \quad (\text{E.43})$$

$$\rho_{21} = \frac{R_4(R_3 + 1)}{3} \left( R_3 R_4 \left( \frac{R_1}{2} + \frac{1}{R_2} + \frac{2}{3} \right) + R_4 + 2 \right)^{-1} \quad (\text{E.44})$$

$$\rho_{11} = \left( \frac{R_4 R_3}{R_2} + 1 \right) \left( R_3 R_4 \left( \frac{R_1}{2} + \frac{1}{R_2} + \frac{2}{3} \right) + R_4 + 2 \right)^{-1} \quad (\text{E.45})$$

$$\rho_{11} = \left( \frac{R_1 R_3 R_4}{2} + \frac{R_4}{3} (R_3 + 1) \right) \left( R_3 R_4 \left( \frac{R_1}{2} + \frac{1}{R_2} + \frac{2}{3} \right) + R_4 + 2 \right)^{-1} \quad (\text{E.46})$$

Five peak sets adds

$$R_5 = \frac{\alpha_{3a}}{\alpha_4} = \frac{3}{2} \frac{\rho_{20} - \rho_{2-1}}{\rho_{2-1}} \quad (\text{E.47})$$

The solution is

$$\rho_{2-1} = \left( 1 + \frac{2R_5}{R_4} + \left( \frac{2}{3}R_5 + 1 \right) + \left( \frac{2}{3}R_5(R_3) + 1 \right) + 1 \right) + \left( \frac{R_3 R_4}{R_2} + 1 \right) \frac{2R_5}{R_4} \quad (\text{E.48})$$

$$+ \left( R_1 R_3 R_5 + \frac{2}{3}R_5(R_3 + 1) + 1 \right)^{-1} \quad (\text{E.49})$$

$$\rho_{20} = \left( \frac{2}{3}R_5 + 1 \right) \rho_{2-1} \quad (\text{E.50})$$

$$\rho_{10} = \frac{2R_5}{R_4} \left( \frac{2}{3}R_5 + 1 \right) \rho_{2-1} \quad (\text{E.51})$$

$$\rho_{21} = \left( \frac{R_3 R_4}{R_2} + 1 \right) \frac{2R_5}{R_4} \rho_{2-1} \quad (\text{E.52})$$

$$\rho_{11} = \left( \frac{R_3 R_4}{R_2} + 1 \right) \frac{2R_5}{R_4} \left( \frac{2}{3}R_5 + 1 \right) \rho_{2-1} \quad (\text{E.53})$$

$$\rho_{22} = \left( R_1 R_3 R_5 + \frac{2}{3}R_5(R_3 + 1) + 1 \right) \rho_{2-1} \quad (\text{E.54})$$

## LIST OF REFERENCES

- [Allard and Kielkopf, 1982] Allard, N. and Kielkopf, J. (1982). The effect of neutral nonresonant collisions on atomic spectral lines. *Reviews of Modern Physics*, 54(4):1103–1182.
- [Allard et al., 2003] Allard, N. F., Allard, F., Hauschildt, P. H., Kielkopf, J. F., and Machin, L. (2003). A new model for brown dwarf spectra including accurate unified line shape theory for the NaI and K I resonance line profiles. *Astronomy and Astrophysics*, 411(3):L473–L476.
- [Anderson et al., 1959] Anderson, L., Pipkin, F., and Baird, J. (1959). N14-N15 Hyperfine Anomaly. *Physical Review*, 116(1):87–98.
- [Anderson, 1979] Anderson, L. W. (1979). Optically pumped electron spin polarized targets for use in the production of polarized ion beams. *Nuclear Instruments and Methods*, 167(3):363–370.
- [Appelt et al., 1998] Appelt, S., Baranga, a., Erickson, C., Romalis, M., Young, a., and Happer, W. (1998). Theory of spin-exchange optical pumping of  $^3\text{He}$  and  $^{129}\text{Xe}$ . *Physical Review A*, 58(2):1412–1439.
- [Babcock, 2005] Babcock, E. (2005). *PhD. Thesis*. PhD thesis, University of Wisconsin-Madison.
- [Babcock et al., 2009] Babcock, E., Boag, S., Becker, M., Chen, W., Chupp, T., Gentile, T., Jones, G., Petukhov, A., Soldner, T., and Walker, T. (2009). Effects of high-flux neutron beams on  $^3\text{He}$  cells polarized in situ with spin-exchange optical pumping. *Physical Review A*, 80(3).
- [Babcock et al., 2005a] Babcock, E., Chann, B., Nelson, I. A., and Walker, T. G. (2005a). Frequency-narrowed diode array bar. *Applied Optics*, 44(15):3098.
- [Babcock et al., 2006] Babcock, E., Chann, B., Walker, T., Chen, W., and Gentile, T. (2006). Limits to the Polarization for Spin-Exchange Optical Pumping of He3. *Physical Review Letters*, 96(8).
- [Babcock et al., 2003] Babcock, E., Nelson, I., Kadlecik, S., Driehuys, B., Anderson, L., Hersman, F., and Walker, T. (2003). Hybrid Spin-Exchange Optical Pumping of He3. *Physical Review Letters*, 91(12).

- [Babcock et al., 2005b] Babcock, E., Nelson, I., Kadlecek, S., and Walker, T. (2005b).  $^3\text{He}$  polarization-dependent EPR frequency shifts of alkali-metal $^3\text{He}$  pairs. *Physical Review A*, 71(1).
- [Baranga et al., 1998] Baranga, A., Appelt, S., Erickson, C., Young, A., and Happer, W. (1998). Alkali-metal-atom polarization imaging in high-pressure optical-pumping cells. *Physical Review A*, 58(3):2282–2294.
- [Barton et al., 1994] Barton, A., Newbury, N., Cates, G., Driehuys, B., Middleton, H., and Saam, B. (1994). Self-calibrating measurement of polarization-dependent frequency shifts from Rb- $^3\text{He}$  collisions. *Physical Review A*, 49(4):2766–2770.
- [Baylis, 1979] Baylis, W. (1979). *Progress in Atomic Spectroscopy, part B*. Plenum, New York.
- [Ben-Amar Baranga et al., 1998] Ben-Amar Baranga, A., Appelt, S., Romalis, M., Erickson, C., Young, A., Cates, G., and Happer, W. (1998). Polarization of  $^3\text{He}$  by Spin Exchange with Optically Pumped Rb and K Vapors. *Physical Review Letters*, 80(13):2801–2804.
- [Chann, 2003] Chann, B. (2003). *PhD. Thesis*. PhD thesis, University of Wisconsin-Madison.
- [Chann et al., 2002a] Chann, B., Babcock, E., Anderson, L., and Walker, T. (2002a). Measurements of  $^3\text{He}$  spin-exchange rates. *Physical Review A*, 66(3).
- [Chann et al., 2002b] Chann, B., Babcock, E., Anderson, L., and Walker, T. (2002b). Skew light propagation in optically thick optical pumping cells. *Physical Review A*, 66(3).
- [Chann et al., 2003] Chann, B., Babcock, E., Anderson, L. W., Walker, T. G., Chen, W. C., Smith, T. B., Thompson, a. K., and Gentile, T. R. (2003). Production of highly polarized [<sup>3</sup>He using spectrally narrowed diode laser array bars. *Journal of Applied Physics*, 94(10):6908.
- [Chann et al., 2000] Chann, B., Nelson, I., and Walker, T. G. (2000). Frequency-narrowed external-cavity diode-laser-array bar. *Optics Letters*, 25(18):1352.
- [Chen et al., 2007] Chen, W., Gentile, T., Walker, T., and Babcock, E. (2007). Spin-exchange optical pumping of  $^3\text{He}$  with Rb-K mixtures and pure K. *Physical Review A*, 75(1):1–14.
- [Driehuys et al., 1996] Driehuys, B., Cates, G. D., Miron, E., Sauer, K., Walter, D. K., and Happer, W. (1996). High-volume production of laser-polarized  $^{129}\text{Xe}$ . *Applied Physics Letters*, 69(12):1668.
- [Drummond, 1974] Drummond, D. L. (1974). Potentials and continuum spectra of Rb-noble gas molecules. *The Journal of Chemical Physics*, 60(9):3426.
- [Erickson et al., 2000] Erickson, C., Levron, D., Happer, W., Kadlecek, S., Chann, B., Anderson, L., and Walker, T. (2000). Spin Relaxation Resonances due to the Spin-Axis Interaction in Dense Rubidium and Cesium Vapor. *Physical Review Letters*, 85(20):4237–4240.

- [Fu et al., 2011] Fu, C., Gentile, T., and Snow, W. (2011). Limits on possible new nucleon monopole-dipole interactions from the spin relaxation rate of polarized  $^3\text{He}$  gas. *Physical Review D*, 83(3).
- [Happer, 1972] Happer, W. (1972). Optical Pumping. *Reviews of Modern Physics*, 44(2):169–249.
- [Happer et al., 2010] Happer, W., Jau, Y.-Y., and Walker, T. G. (2010). *Optically Pumped Atoms*. WILEY-VCH Verlag GmbH & Co. KGa, Weinheim.
- [Jau et al., 2004] Jau, Y.-Y., Kuzma, N., and Happer, W. (2004). Measurement of  $^{129}\text{Xe}$ -Cs binary spin-exchange rate coefficient. *Physical Review A*, 69(6).
- [Kadlecek, 2000] Kadlecek, S. (2000). *PhD. Thesis*. PhD thesis, University of Wisconsin-Madison.
- [Kadlecek et al., 2001] Kadlecek, S., Anderson, L., Erickson, C., and Walker, T. (2001). Spin relaxation in alkali-metal  $^1\Sigma_g^+$  dimers. *Physical Review A*, 64(5).
- [Kadlecek et al., 1998] Kadlecek, S., Anderson, L., and Walker, T. (1998). Field Dependence of Spin Relaxation in a Dense Rb Vapor. *Physical Review Letters*, 80(25):5512–5515.
- [Kielkopf, 1980] Kielkopf, J. (1980). Measurement of the width, shift and asymmetry of the sodium D lines broadened by noble gases. *Journal of Physics B: Atomic and Molecular Physics*, 13:3813.
- [Kominis et al., 2003] Kominis, I. K., Kornack, T. W., Allred, J. C., and Romalis, M. V. (2003). A subfemtotesla multichannel atomic magnetometer. *Nature*, 422(6932):596–599.
- [Lancor et al., 2010a] Lancor, B., Babcock, E., Wyllie, R., and Walker, T. (2010a). Breakdown of Angular Momentum Selection Rules in High Pressure Optical Pumping Experiments. *Physical Review Letters*, 105(8).
- [Lancor et al., 2010b] Lancor, B., Babcock, E., Wyllie, R., and Walker, T. (2010b). Circular dichroism of RbHe and RbN<sub>2</sub> molecules. *Physical Review A*, 82(4).
- [Lancor and Walker, 2010] Lancor, B. and Walker, T. (2010). Effects of nitrogen quenching gas on spin-exchange optical pumping of  $^3\text{He}$ . *Physical Review A*, 82(4).
- [Lancor and Walker, 2011] Lancor, B. and Walker, T. (2011). Polarization limits in K-Rb spin-exchange mixtures. *Physical Review A*, 83(6).
- [Levy and Zelenski, 1998] Levy, C. D. P. and Zelenski, A. N. (1998). Polarized ion sources for high-energy accelerators (invited). *Review of Scientific Instruments*, 69(2):732.
- [Lide, 2011] Lide, D. R. (2011). *Handbook of Chemistry and Physics 91st Edition*.

- [Littman and Metcalf, 1978] Littman, M. G. and Metcalf, H. J. (1978). Spectrally narrow pulsed dye laser without beam expander. *Applied Optics*, 17(14):2224.
- [Pascale, 1983] Pascale, J. (1983). Use of  $l$ -dependent pseudopotentials in the study of alkali-metal-atomHe systems. The adiabatic molecular potentials. *Physical Review A*, 28(2):632–644.
- [Peterson and Anderson, 1991] Peterson, D. and Anderson, L. (1991). Effect of radiation trapping on the polarization of an optically pumped alkali-metal atomic beam. *Physical Review A*, 43(9):4883–4888.
- [Ramsey, 1953] Ramsey, N. (1953). *Nuclear Moments*. Wiley and Sons, Inc., New York.
- [Romalis and Cates, 1998] Romalis, M. and Cates, G. (1998). Accurate  $^3\text{He}$  polarimetry using the Rb Zeeman frequency shift due to the Rb- $^3\text{He}$  spin-exchange collisions. *Physical Review A*, 58(4):3004–3011.
- [Romalis et al., 1997] Romalis, M., Miron, E., and Cates, G. (1997). Pressure broadening of Rb  $D_{1}$  and  $D_{2}$  lines by  $^3\text{He}$ ,  $^4\text{He}$ ,  $\text{N}_2$ , and Xe: Line cores and near wings. *Physical Review A*, 56(6):4569–4578.
- [Rotondaro and Perram, 1998] Rotondaro, M. and Perram, G. (1998). Collision-induced transitions between the Zeeman-split (J,m) levels of Rb( $5^2P_{1/2}$ ,  $5^2P_{3/2}$ ). *Physical Review A*, 58(3):2023–2029.
- [Schaefer et al., 1989] Schaefer, S., Cates, G., Chien, T.-R., Gonatas, D., Happer, W., and Walker, T. (1989). Frequency shifts of the magnetic-resonance spectrum of mixtures of nuclear spin-polarized noble gases and vapors of spin-polarized alkali-metal atoms. *Physical Review A*, 39(11):5613–5623.
- [Sharma et al., 2008] Sharma, M., Babcock, E., Andersen, K., Barrón-Palos, L., Becker, M., Boag, S., Chen, W., Chupp, T., Danagouljian, A., Gentile, T., Klein, A., Penttila, S., Petoukhov, A., Soldner, T., Tardiff, E., Walker, T., and Wilburn, W. (2008). Neutron Beam Effects on Spin-Exchange-Polarized He3. *Physical Review Letters*, 101(8).
- [Singh, 2010] Singh, J. (2010). *PhD. Thesis*. PhD thesis, University of Virginia.
- [Singh et al., 2009] Singh, J., Dolph, P., Mooney, K., Nelyubin, V., Tobias, A., Kelleher, A., Averett, T., Cates, G., Crabb, D. G., Prok, Y., Poelker, M., Liuti, S., Day, D. B., and Zheng, X. (2009). *Recent Advances in Polarized He-3 Targets*, volume 19. AIP.

- [Slifer et al., 2008] Slifer, K., Amarian, M., Auerbach, L., Averett, T., Berthot, J., Bertin, P., Bertozzi, B., Black, T., Brash, E., Brown, D., Burtin, E., Calarco, J., Cates, G., Chai, Z., Chen, J.-P., Choi, S., Chudakov, E., Ciofi degli Atti, C., Cisbani, E., de Jager, C., Deur, A., DiSalvo, R., Dieterich, S., Djawotho, P., Finn, M., Fissum, K., Fonvieille, H., Frullani, S., Gao, H., Gao, J., Garibaldi, F., Gasparian, A., Gilad, S., Gilman, R., Glamazdin, A., Glashauser, C., Glöckle, W., Golak, J., Goldberg, E., Gomez, J., Gorbenko, V., Hansen, J.-O., Hersman, B., Holmes, R., Huber, G., Hughes, E., Humensky, B., Incerti, S., Iodice, M., Jensen, S., Jiang, X., Jones, C., Jones, G., Jones, M., Jutier, C., Kamada, H., Ketikyan, A., Kominis, I., Korsch, W., Kramer, K., Kumar, K., Kumbartzki, G., Kuss, M., Lakuriqi, E., Laveissiere, G., Lerose, J., Liang, M., Liyanage, N., Lolos, G., Malov, S., Marroncle, J., McCormick, K., McKeown, R., Meziani, Z.-E., Michaels, R., Mitchell, J., Nogga, A., Pace, E., Papandreou, Z., Pavlin, T., Petratos, G., Pripstein, D., Prout, D., Ransome, R., Roblin, Y., Rowntree, D., Rvachev, M., Sabatié, F., Saha, A., Salmè, G., Scopetta, S., Skibiski, R., Souder, P., Saito, T., Strauch, S., Suleiman, R., Takahashi, K., Tejiro, S., Todor, L., Tsubota, H., Ueno, H., Urciuoli, G., Van der Meer, R., Vernin, P., Voskanian, H., Witaa, H., Wojtsekhowski, B., Xiong, F., Xu, W., Yang, J.-C., Zhang, B., and Zolnierczuk, P. (2008). He3 Spin-Dependent Cross Sections and Sum Rules. *Physical Review Letters*, 101(2).
- [Szudy and Baylis, 1975] Szudy, J. and Baylis, W. (1975). Unified Franck-Condon treatment of pressure broadening of spectral lines. *Journal of Quantitative Spectroscopy and Radiative Transfer*, 15(7-8):641–668.
- [Szudy and Baylis, 1996] Szudy, J. and Baylis, W. (1996). Profiles of line wings and rainbow satellites associated with optical and radiative collisions. *Physics reports*, 266(3-4):127–227.
- [Vasilakis et al., 2009] Vasilakis, G., Brown, J. M., Kornack, T. W., and Romalis, M. V. (2009). Limits on New Long Range Nuclear Spin-Dependent Forces Set with a  $K^{-3}$ He Comagnetometer. *Physical Review Letters*, 103(26).
- [Vliegen et al., 2001] Vliegen, E., Kadlecsek, S., Anderson, L., Walker, T. G., Erickson, C., and Happer, W. (2001). Faraday rotation density measurements of optically thick alkali metal vapors. *Nuclear Instruments and Methods in Physics Research Section A: Accelerators, Spectrometers, Detectors and Associated Equipment*, 460(2-3):444–450.
- [Walker and Happer, 1997] Walker, T. G. and Happer, W. (1997). Spin-exchange optical pumping of noble-gas nuclei. *Reviews of Modern Physics*, 69(2):629–642.
- [Walker et al., ] Walker, T. G., Nelson, I., and Kadlecsek, S. Amerhsam Health Report (unpublished). Technical report.
- [Walkup et al., 1984] Walkup, R., Stewart, B., and Pritchard, D. (1984). Collisional line broadening due to van der Waals potentials. *Physical Review A*, 29(1):169–173.
- [Walter et al., 2001] Walter, D., Griffith, W., and Happer, W. (2001). Energy Transport in High-Density Spin-Exchange Optical Pumping Cells. *Physical Review Letters*, 86(15):3264–3267.

[Young et al., 1997] Young, A. R., Appelt, S., Ben-Amar Baranga, A., Erickson, C., and Happer, W. (1997). Three-dimensional imaging of spin polarization of alkali-metal vapor in optical pumping cells. *Applied Physics Letters*, 70(23):3081.